AB

EX-RALT-106

(9111)

EVENT RECONSTRUCTION AND A STUDY OF ELECTROWEAK EFFECTS IN $e^+e^- \rightarrow \mu^+\mu^-(\gamma)$ AT OPAL.

Nigel Keith Watson

Thesis submitted for the degree of
Doctor of Philosophy

School of Physics and Space Research
Faculty of Science
University of Birmingham

December 1990

Synopsis

The full 1990 data sample recorded in the OPAL detector on the LEP collider was analysed to extract the muon pair cross section and asymmetry at seven centre of mass energies between 88 GeV and 95 GeV, with an integrated luminosity of 6.6 pb^{-1}. A detailed analysis of the cross section and asymmetry measurements and their energy variation was subsequently used to determine the mass (M_Z) and width (Γ_Z) of the Z^0 and the pole cross section for muons ($\sigma_{\mu\mu}^{\text{pole}}$). The effective vector ($\hat{v}_l$) and axial vector ($\hat{a}_l$) couplings to charged leptons were also determined in the combinations $\hat{a}_l{}^2\hat{v}_l{}^2$ and $\hat{a}_l{}^2$ (with $a_l \equiv I_3$). The values obtained are;

$$\begin{aligned}
M_Z &= 91.21 \pm 0.04 \pm 0.02 \text{ (LEP) GeV},\\
\Gamma_Z &= 2.46 \pm 0.07 \pm 0.01 \text{ (LEP) GeV},\\
\sigma_{\mu\mu}^{\text{pole}} &= 2.03 \pm 0.03 \pm 0.03 \text{ nb},\\
\hat{a}_l{}^2\hat{v}_l{}^2 &= (73 \pm 54) \times 10^{-5},\\
\hat{a}_l{}^2 &= 0.23 \pm 0.04,\\
\Gamma_l &= 0.0834 \pm 0.0025 \pm 0.0005 \text{ GeV}.
\end{aligned}$$

The leptonic partial width (Γ_l) is deduced from the measured M_Z, Γ_Z and $\sigma_{\mu\mu}^{\text{pole}}$. The colinear hard photonic cross section for muon pairs and the differential energy spectrum of photons in these events is studied. It is shown that photons measured in this exclusive channel originate from final state radiation. On the basis of all quantities studied herein. the standard model provides a good description of the process $e^+e^- \to \mu^+\mu^-(\gamma)$.

A detailed description of the software tools developed to reconstruct muons in the endcap muon detectors of the OPAL experiment, which are particularly important for measuring the muon pair forward-backward asymmetry, is presented.

The Author's Contribution

The OPAL collaboration is a group of several hundred people who work remarkably well together and few activities within the experiment are carried out in isolation. However, despite the large size of the group, it is possible to identify the work of individuals. A brief summary of my contribution to the experiment in the last three years is given below.

Most of this work has been carried out within the offline group of OPAL. Shortly after joining the experiment I took over responsibility for a variety of software activities relating to the muon endcap sub-detector. This entailed significant software development work in the areas of event reconstruction, graphics and Monte Carlo; approximately 90% of the reconstruction code was re-written. I took part in a joint study of the detection of the Higgs boson in OPAL, concentrating upon the Bjorken process with an inclusive dimuon final state.

I have contributed to the event display program by making changes for the specific needs of the muon detectors as well as improving the automatic maintenance of the OPAL software environment for OPAL institutes remote from CERN. Shortly before the muon endcaps were fully commissioned at CERN, I wrote the necessary software to allow the muon endcap reconstruction to interact with the calibration database as well as to improve the error recovery of the software. During the pilot run of August of 1989 when the first data was recorded I was part of a small group responsible for running the 'hotline', and during the main physics run of 1989 I was one of the 'experts' responsible for the offline production processing of data.

All aspects of the analysis presented in this thesis have been carried out independently (to a good approximation) of the main analysis effort at CERN. This has entailed my finalising cuts, evaluating cross sections, performing the various fits to determine the asymmetries, studying the acceptance and generating a large number of fully simulated Monte Carlo events. The colinear photon study is not a measurement that the experiment has presented previously. Furthermore, all of the final fits have been carried out independently, *i.e.* I have made all necessary changes to the various lineshape programs and written the analytic cross section program.

Acknowledgements

I would like to thank Professors Derek Colley and John Dowell for giving me the opportunity to study in the Birmingham High Energy Physics Group and for their advice, support and the generosity throughout the course of my studies here. I acknowledge the financial support provided by the tax-payers of Great Britain, three years of which were administered under the auspices of the SERC.

I am very grateful to Pete Watkins, my supervisor, who throughout the past three years has been a close friend and highly valued colleague. His constant enthusiasm, advice and support, particularly in helping to organise my long term attachment at CERN with less than 3 weeks notice, have been invaluable throughout my studies. I am also indebted to him for having suffered this thesis in draft form and for his comments on the text. I would like to thank Peter Hattersley, Mel Jobes and Ian Bloodworth, the other members of the offline group at Birmingham with whom it has been fun to work. I am grateful to Ian and Peter for taking over the general responsibility for our code, thereby allowing me to concentrate on analysis.

I owe a great deal to everyone from whom I have learned about computers, in particular to Lawrie Lowe for running the ever stable `BHIA`, solving 'impossible' problems on several occasions and always being able to answer queries about IBMs, to Bill Stokes for his expert help on VAX systems and to Jonathan Gregory and Dave Charlton for numerous discussions about computers. I'd like to belatedly express my gratitude to Gron Jones, Kev Varvell and Roger Jones, who between them are probably at least partly responsible for my interest in particle physics, computers and offline code.

My colleagues and good friends Tim Smith, Dave Rees, Steve Hillier and Alan between them overcame the daunting task of commissioning the muon endcap online system without which the analysis presented herein would have been impossible (particularly so the comparison of Monte Carlo and real data with the reconstruction code!). This achievement owes much to their enthusiasm and unquestionable all-round competence. Likewise, the design, testing and production of the muon endcaps was the result of much hard work by Jim Homer, Tom McMahon and the RAL engineers and technicians.

I thoroughly enjoyed my long attachment at CERN, largely because of the very friendly working atmosphere generated by the members of OPAL, epitomised by the collaboration leader, Aldo Michelini. I am very grateful to Mette Decamp, Sue Geddes, Mary-Elizabeth Shewry and Sue Cannon who have all been incredibly helpful, particularly on the (several) occasions when I had a 'last minute' panic with paperwork or accommodation. There are too many people with whom I have worked at CERN to mention even a significant fraction of them here and I hope no-one is too offended if only thank by name George Lafferty, Sylvain Weisz, Adriaan Buijs, Terry Wyatt, Steve O'Neale, Richard Hemingway and Pete Hinde. Very special thanks are due to Glenn Patrick for all of his help with, and discussions about, RALVM; it clear that without his efforts at RAL, my analysis would have been impossible.Apologies to everyone else, but the sooner these acknowledgements are finished, the sooner I can submit this thesis!

On the social scene, I enjoyed going walking in the summer and skiing when there was sufficient snow in winter with Martin Saich, Simon Patton, Julie Hart, Tony Wildish, Steve Hillier, Andy Kirk, Roger Jones, Alan and Miriam. I've also been fortunate in having such good friends as Bill Murray, Colin Roach, Mike Akrawy, Gary Barker, Nick Wood and Sarah Pawley. My thanks also to anyone who discovered that "2 mins" can be a rather long time or who tried out an "interesting"solution to a problem. On my return to Birmingham I was glad to have Matt Couch and Mark Nikitas as fellow thesis scribbling sufferers during the summer and autumn—without them this would have been more of an ordeal. It's also been a privilege to know and work with Dave Rees, Dave (`DEVANS`), Tan and Richard and lately Mark Whalley, Chris and Mike who have between them helped to maintain a general air of sanity (most of the time) in the locality.

Special thanks are due to all of my friends with whom I have shared houses, and have known outside of work, especially Paul and Nicola D'Urso, Dave Hargreaves, Simon Gompertz, Jayne Nation, Pete Jones, Andy Butterworth, Sarah Moverely, Andy Shaw and Tracie Withers. Tracie has been one of my closest friends since I came to Birmingham, even to the point of suffering early parts of this thesis in draft form! I thank Mum and Dad, Jen and Alan, Dave and Simon for their constant love and support throughout my studies. Finally, I am ever grateful to Miriam, for her love, support and sufferance during the writing of this thesis; she has been a constant source of inspiration when I seemed lacking in it.

Nige, December 21st 1990, Birmingham.

Contents

List of Figures

List of Tables

Chapter 1

Introduction

The description of the physical universe at a fundamental level is an attractive (albeit elusive) goal and many theoretical models have been proposed in the past to explain experimentally observed phenomena; models which are unable to withstand detailed comparison with ever more refined experimental data are simply discarded. In the last few decades this process has resulted in the development of a theoretical model that can provide a complete description of all known (non-gravitational) particle interactions. This theory, which is based on the principle that gauge symmetries exist within certain types of quantum fields, is sufficiently successful that it is known as the 'standard model' [1] of particle physics. As such it is currently being subjected to a series of stringent, high precision tests by many experimental groups at various laboratories around the world.

This thesis presents a measurement of some of the fundamental parameters in the electroweak sector of the standard model. The measurements are compared with theoretical predictions and constitute a precision test of the standard model. This analysis been carried out within the OPAL collaboration as part of the LEP project at CERN in Geneva. In order to put these tests into context, a brief overview of the main features of the standard model, with a bias towards electroweak physics, is given below.

1.1 The standard model

At the present time there are four known forces that are thought to be fundamental in nature and a small number of elementary particles which are influenced by these forces. The standard model successfully describes the effects of the electromagnetic, weak and strong interactions in terms of two renormalisable gauge field theories down to a scale of $O(10^{-18}\ \mathrm{m})$. The gravitational force is not part of the standard model due to a problem arising from the tensor nature of the gravitational field quanta. As the gravitational force is negligible compared to all other forces at the energies that have so far been reached by accelerators, its omission from the standard model is assumed to have an immeasurably small effect on numerical results that may be compared with experimental data.

1.1.1 Particle spectrum

There are two types of elementary particles in the standard model, the distinction being made on the basis of spin quantum numbers. Spin-$\frac{1}{2}$ fermions are the basic constituents of matter upon which the various forces act and bosons are the gauge field quanta that mediate these forces. Both fermions and bosons are pointlike and structureless in this theory which is consistent with all measurements so far performed.

Elementary fermions

The basic fermions of the model are divided into two categories, *viz.* quarks which are subject to the influence of the strong interaction and leptons which are not. There are six different flavours of quarks, three of which have charge $+\frac{2}{3}$e (*i.e.* u, c and t) while the remaining three have charge $-\frac{1}{3}$e (*i.e.* d, s, b). Of these, all except the t quark have been 'observed' experimentally. These are observed indirectly through hadronic spectroscopy—free quarks are not allowed in the standard model because of colour confinement. There are also six flavours of leptons, three with one unit of charge (*i.e.* e^-, μ^-, τ^-) and a further three which are electrically neutral (*i.e.* ν_e, ν_μ, ν_τ). There is a symmetry between the different quarks and leptons which is evident when they are grouped together into 'generations', the fermions in successive generations being higher mass replicas of those in the first generation. One of the most important results that has been obtained from the early running of the LEP experiments at CERN is that there are only three such generations [2]. These are;

$$(\mathrm{e}, \nu_e; \mathrm{u}, \mathrm{d}) \qquad (\mu, \nu_\mu; \mathrm{c}, \mathrm{s}) \qquad (\tau, \nu_\tau; \mathrm{t}, \mathrm{b}).$$

Within each generation fermions are arranged in SU(2) doublets (left-handed fermions) and singlets (right-handed fermions) as follows;

$$\begin{pmatrix} \nu_e \\ \mathrm{e} \end{pmatrix}_L \quad \begin{pmatrix} \mathrm{u} \\ \mathrm{d} \end{pmatrix}_L \quad \mathrm{e}_R \quad \mathrm{u}_R \quad \mathrm{d}_R. \tag{1.1}$$

The doublets and singlets have different quantum number assignments—a feature which is allowed by virtue of helicity conservation in gauge interactions as well as being necessary to reproduce the observed parity-violating behaviour of the weak force. Furthermore, the grouping of fermions into these generations in the standard model ensures cancellation of the Adler-Bell-Jackiw (ABJ) anomalies [3] which destroy the renormalisation of the theory.

Elementary (gauge) bosons

Interactions between the quarks and leptons are described using the formalism of quantum field theory; the forces are mediated by the exchange of virtual field quanta associated with these (gauge) fields. The electromagnetic force is the result of virtual photon exchange between charged particles, the weak force by the exchange of massive, intermediate $W^\pm$ and Z^0 vector bosons and the strong force by the exchange of an octet of massless, coloured gluons. The fact that the $W^\pm$ and Z^0 gauge bosons are massive ($M_W \sim 80$ GeV and $M_Z \sim 90$ GeV) can be inferred from the relatively short range of the weak nuclear force, typically 10^{-17} m. It is the Z^0 boson, responsible for the weak neutral current interaction, that is studied at LEP to a much higher precision than possible in lower energy experiments.

1.1.2 Quantum field theories

Early experiments revealed that all purely leptonic charged current interactions had the same coupling in weak interactions. Furthermore, a similar universality of coupling was observed among all quarks after corrections had been made for the mass eigenstates and the weak eigenstates of the quarks being different from each other [4]. This universality is indicative of a more fundamental symmetry and can be described by two relativistic quantum field theories both of which are postulated to be invariant under local gauge transformations and renormalisable. These two pre-requisites are necessary for the theory to predict interactions and to allow calculations which yield finite results to be carried out and are therefore of the utmost importance. These field theories and the associated symmetry transformations constitute the basis of the standard model.

Gauge invariance

In quantum field theory, the elementary fermions are described by complex fields which may be used to construct a Lagrangian. These fermion fields have an unobservable quantum mechanical phase and it is postulated that the Lagrangian is invariant under a space-time dependent, or *local*, transformation of this phase. A local phase transformation is known for historical reasons as a *gauge* transformation.

Although such a postulate is not unreasonable—absolute phase is not a physical observable so it is should not affect physical measurements—there is *a priori* no compelling reason for the requirement.

Applying such an arbitrary transformation would in general alter the Lagrangian. A special case such as the gauge transformation being the same at all space-time points, *i.e.* a *global* phase transformation, which would naturally leave the Lagrangian unchanged, is an obvious exception. However, it may be restored to its assumed invariant state by introducing a set of fields into the theory to locally compensate for any changes in the Lagrangian caused by the way in which the fermion fields have been transformed. The theory, enlarged by the addition of the so-called *gauge fields* to satisfy the initial postulate, now possesses fields that predict the dynamics of interactions; the quanta associated with these gauge fields are the aforementioned gauge bosons. In this way, the entire theory of interacting particles is determined by the way in which the fermion fields transform under operations of a particular symmetry group. The specific choice of symmetry groups used in the standard model is included in sections 1.1.3 and 1.1.4.

As an example, the prototype of most modern gauge field theories is Quantum Electrodynamics (QED) in which the requirement of gauge invariance of a single charged fermion field under local U(1) phase transformations predicts the electromagnetic interaction with quite remarkable precision. Measurements of the gyromagnetic ratio of the electron, g, which differs from the tree level prediction of g=2 as a result of virtual electromagnetic corrections, agree with renormalised QED calculations to better than seven significant figures [5].

Renormalisation

The calculation of physical results in quantum field theory are currently carried out entirely within the framework of perturbation theory. The need for renormalisation and a very simple description of the procedure involved can be illustrated by considering the determination of the cross section for the elastic scattering process $e^-\mu^- \rightarrow e^-\mu^-$. In lowest order this is the single photon exchange process of figure 1.1a, for which a finite amplitude may be calculated. However, when higher order terms of the perturbation expansion are included such as the vacuum polarisation diagram depicted in figure 1.1b which enters at order α^2, then logarithmic divergences appear due to infinite integrals over the momenta in these loops.

To obtain a finite result, the renormalisation process introduces a particular *regularisation scheme* by which all divergent integrals are made finite so that they may be formally manipulated, whilst still remaining Lorentz invariant; two commonly used schemes are those of 'covariant' and 'dimensional' regularisation. The essence of the former is to define an finite upper bound on the range of the momentum integration, say Λ, separate the divergent part (which will be a function of Λ) from the finite part, absorb the divergent parts into a redefinition of a physical quantity such as charge or mass, and then allow the cut-off parameter to tend to

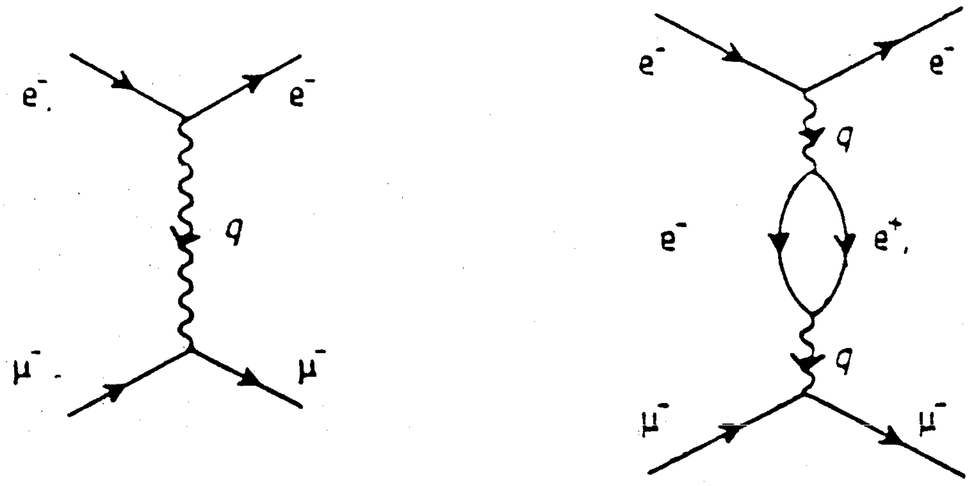

(a) one γ exchange (b) vacuum polarisation correction.

Figure 1.1: Examples of tree level and one-loop diagrams for $e^-\mu^- \rightarrow e^-\mu^-$.

infinity. The redefined physical parameters whose values must be determined by experiment are referred to as ‘renormalised’ and the unmeasurable quantities containing the divergences are known as ‘bare’.

This is the vital distinction between renormalisable and non-renormalisable theories: in the former type, all divergences may be removed by the introduction of a finite number of parameters that have to be fixed by experiment, whereas in the latter, new types of divergences may occur in each order of perturbation theory and so an infinite number of parameters would be required to bypass the infinities by the same method.

For the scattering process example above, the amplitude is of the general form

$$e^2 \times (\text{current}) \times (\text{photon propagator}) \times (\text{current}), \tag{1.2}$$

where the (electromagnetic) current is a product of charged lepton spinors and a Dirac gamma matrix[1]. When the one-loop diagram is added to the lowest order expression, the amplitude and currents remain effectively unchanged if the defi-

---

[1] The charge, e, is removed from the current and included as an overall factor in the amplitude to simplify this description.

nition of the charge of the electron, e, is modified accordingly. Considering only this one-loop correction, the appropriate 'renormalisation' of the electron charge is given,

$$\mathrm{e} \longrightarrow \mathrm{e}' = \mathrm{e}\left[1 - \frac{\alpha}{3\pi}\ln\left(\frac{\Lambda^2}{m^2}\right)\right]^{\frac{1}{2}} . \tag{1.3}$$

This expression for e' is in fact one term of a more general, infinite set of higher order corrections. The summation of all terms gives the fully renormalised charge,

$$\mathrm{e}_R = \mathrm{e}\left(1 + \sum_{m=1}^{\infty} \alpha^m c_m(\Lambda^2)\right) ,$$

where coefficients $c_m(\Lambda^2)$ are obtained from considering all diagrams of a given order in perturbation theory. This e_R must be determined by experiment and a physically meaningful definition is the charge as perceived from infinity, *i.e.* in the classical long-wavelength limit. The final step is to invert the series, express e in terms of e_R, expand to a given order in α (*e.g.* in the first order case $\mathrm{e}_R = \mathrm{e}'$ of equation 1.3) and substitute for e in equation 1.2. In doing so, all the Λ dependence is removed leaving the amplitude finite when the the cut-off is allowed to tend to infinity. A proper treatment of renormalisation is non-trivial and the interested reader is referred to the extensive literature for details [3,6,7].

1.1.3 Electroweak theory

The Glashow-Salam-Weinberg (GSW) electroweak theory describes the weak and electromagnetic interactions by requiring invariance of an appropriate Lagrangian under transformations of the non-Abelian, direct product group $\mathrm{SU(2)_L} \times \mathrm{U(1)_Y}$, where $\mathrm{SU(2)_L}$ and $\mathrm{U(1)_Y}$ are the gauge groups of weak isospin and the weak hypercharge (Y) respectively. Non-Abelian groups are ones in which the members of the group do not commute, or in the parlance of associated field quanta, the gauge bosons may interact with one another. Such gauge theories are often called Yang-Mills theories for historical reasons.

The weak isospin transitions only affect the left-handed fermions in each generation (*i.e.* the doublets of equation 1.1), hence the subscripted L in $\mathrm{SU(2)_L}$. Maintaining invariance with the above product group entails the introduction of four gauge fields, *viz.* a weak isotriplet of vector fields, W^i and a neutral hypercharge vector field, B^0. Experimentally, the weak force is observed to have a parity-violating charged current nature and the charged members of the isotriplet of gauge fields, when arranged in suitable linear combinations, reproduce this behaviour. The physical fields with which the observed massive gauge bosons, $\mathrm{W}^{\pm}$, will ultimately be associated are

$$\mathrm{W}^{\pm}_{\mu} = \frac{1}{\sqrt{2}}(W^1_{\mu} \mp W^2_{\mu}).$$

In contrast, the weak neutral current and electromagnetic processes couple to both helicity states of fermions and so neither can be associated with the (parity-violating) W^3 field alone. This is part of the reason why the weak interaction cannot be described in isolation from the electromagnetic interaction, whereas the converse is not true as demonstrated by the success of QED. It happens that a mixing of the two neutral gauge fields is required to obtain the physical fields corresponding to the Z^0 gauge boson and the photon. The mixing, parameterised by the so-called weak mixing (or Glashow) angle, θ_{W}, is given by

$$\begin{aligned} \mathrm{Z}_{\mu} &= W^3_{\mu}\cos\theta_{\mathrm{W}} - B_{\mu}\sin\theta_{\mathrm{W}} \\ \mathrm{A}_{\mu} &= W^3_{\mu}\cos\theta_{\mathrm{W}} + B_{\mu}\sin\theta_{\mathrm{W}}. \end{aligned} \tag{1.4}$$

It is worth noting that as this theory is based on the product of two disconnected sets of gauge transformations that there is no *prediction* for the relation between the weak and electromagnetic coupling constants and so it is not a fully unified theory in every sense. Furthermore, the introduction of finite masses to the Lagrangian for any gauge bosons or fermions would destroy the invariance and hence the renormalisation of the theory.[2] The favoured method of circumventing this dilemma is to use the Higgs mechanism [8] although it can also be achieved by other means [9].

Hidden symmetries—the Higgs mechanism.

A consequence of the symmetry of the GSW theory is that the four gauge bosons are constrained to have zero mass, whereas the observed short range of the weak

---

[2] Local gauge invariance is a *necessary* condition for the theory to be renormalisable.

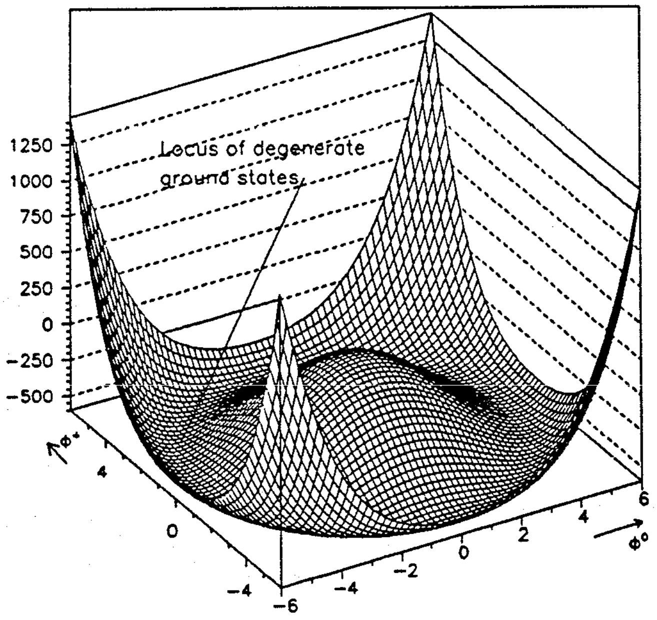

Figure 1.2: Higgs potential energy and locus of degenerate ground states

interaction indicates that the weak gauge bosons are of $O(100\ GeV)$. Massive particles can be accommodated in the theory if the symmetry is broken, although explicitly breaking the symmetry by an *ad hoc* addition of mass terms into a Lagrangian describing the interaction will render the theory non-renormalisable and hence of no practical interest. However, if the Lagrangian itself remains invariant under local gauge transformations whilst the physical vacuum (or ground state) is not then some of the symmetry inherent in the theory will be 'hidden' which turns out to be sufficient for the purpose in hand.

In the standard model, this is carried out by the introduction of a complex, isodoublet scalar field, ϕ, consisting of four Higgs fields. The self-interaction potential for this field, which appears linearly in the Lagrangian, is given

$$V(\phi^\dagger\phi) = -\mu^2\phi^\dagger\phi + \lambda(\phi^\dagger\phi)^2,$$

where μ^2 and λ are coupling parameters. This potential has a infinitely degenerate set of minima, the non-trivial solutions (for $\mu^2, \lambda > 0$) being at $|\phi|^2 = \mu^2/2\lambda$. It should be stressed that although the potential itself is symmetric under continuous transformations in ϕ, the choice of any particular ground state or minima in the potential (about which perturbation expansions may be performed) 'spontaneously breaks' the symmetry. The potential and the locus of minima for the scalar field are illustrated in figure 1.2.

Unfortunately the spontaneous breaking of any continuous symmetry implies the existence of an additional massless scalar boson, often called a Goldstone boson. This is the crux of *Goldstone's theorem* [3, pp 144–151]. However, no gauge fixing condition imposes all of the normal axioms of field theory on a gauge field and these are necessary for the proof of Goldstone's theorem to hold and so the additional massless scalars may be removed from the theory by a judicious choice of ground state. Following a detailed mathematical analysis, the quanta associated with three of the Higgs fields (*i.e.* the 'would-be' Goldstone bosons) may be combined with the three weak gauge bosons to confer mass on the latter as originally intended, removing the zero mass Goldstone bosons from the physically observed spectrum in the process [3, pp 240–247].

As the vacuum expectation value (vev) of each Higgs field is in general non-zero, choosing any one of the infinite number of ground states[3] as the physical vacuum results in a physical vacuum with non-zero weak hypercharge and isospin. Gauge bosons coupling to this vacuum develop quadratic terms in the Lagrangian proportional to the vevs of the Higgs fields *i.e.* they become massive. This is usually referred to as the *Higgs mechanism*. (For details of the mechanism, see [8] or, for a review, [3, pp 240–247, 394–399].) A necessary feature of this mechanism is the existence of at least one physical scalar with finite mass, *i.e.* the neutral Higgs boson. Despite all couplings of this scalar to other particles being predicted within the standard model, there is no prediction for its mass. To date no such fundamental object has been observed by experiments [10].

1.1.4 Quantum chromodynamics

Quantum chromodynamics (QCD) is a non-Abelian gauge theory based on the group SU(3). The basis of the theory is that all quarks possess a *colour* degree of freedom, there being three possible colour states in which a quark may exist (R,

---

[3] A ground state is a given set of vevs for the four Higgs fields.

G, B). This was originally proposed to allow the construction of wave functions that are antisymmetric under interchange of quark labels for the Ω^-, Δ^- and Δ^{++} baryons which in the absence of an extra degree of freedom such as colour is not possible. These three quark states are fermions, hence the antisymmetry requirement. It is postulated that only colour singlets may be observed, thus single quark states, which are always coloured, are not allowed. This is called *colour confinement.*

Studies of the momentum distributions of quarks in deep inelastic lepton-nucleon scattering experiments lead to the conclusion that there exist electrically neutral particles carrying momentum within hadrons. These are thought to be the gauge bosons of QCD, called *gluons*. The mediators of the strong interaction are an octet of massless, bi-coloured gluons. The gluons act on objects having colour quantum numbers such as quarks. Being coloured themselves, gluons may also interact with each other illustrating the non-Abelian nature of the theory.

In processes involving large 4-momentum transfers, quarks behave as though they are only weakly interacting whereas at larger inter-quark separations the converse is true. The former behaviour is the property that caused QCD to be recognised as a good candidate theory of the strong interaction, *i.e.* that the effective coupling decreases at short distances tending towards a free field theory as the distance in question tends to zero. This is called *asymptotic freedom* and it is something that a renormalisable field theory cannot possess without also having non-Abelian gauge fields [3, pp 284–288]. In contrast to QED where the coupling constant is small ($\alpha \simeq \frac{1}{137}$), the coupling in QCD is large enough ($\alpha_s \simeq 0.12$) to restrict the applicability of perturbative methods to the regime of small distances (or high 4-momentum transfers).

As perturbation theory is the only calculational method available in field theory, it is not possible to fully describe even a simple process such as the pair production of quark states in e^+e^- annihilation. In this case, the quarks are converted to hadrons with unit probability and the short distance behaviour of the process may be described semi-quantitatively by perturbative methods. At larger separations the effective coupling constant increases such that the approach is no longer valid. In order to compare QCD calculations with experimental data it is necessary to either restrict the comparison to quantities which are only sensitive to the initial response of the system in the perturbative region such as total hadronic or jet cross sections or for the behaviour of the non-perturbative to be modelled in an empirical way.

1.2 Electroweak tests of the standard model

Many aspects of the standard model have been compared with experiment and all such tests have reinforced the view that the standard model provides an excellent description of three out of the four known (and assumed) fundamental interactions: even if it eventually transpires that it is not the ultimate description of the physical universe it is the framework inside which most investigations are carried out. Among the most dramatic supporting evidence for the validity of the model was the prediction of weak neutral current interactions mediated by the Z^0 first observed in $\nu_\mu N$ scattering in the Gargamelle bubble chamber at CERN [11] and the observation of the massive $W^\pm$ and Z^0 gauge bosons in the UA1 and UA2 experiments at CERN [12] with good agreement between the predicted and observed masses. With their existence well established the Large Electron Positron (LEP) collider was built at CERN to thoroughly investigate the precise nature of these very important massive gauge bosons.

At the present time, the project is in the first of two distinct phases of operation during which electrons and positrons are collided at centre of mass energies in the vicinity of the Z^0 resonance energy. Experiments collecting data at this machine have together accumulated approximately half a million Z^0 decays. To put this into context, the the largest number of Z^0 decays observed in the world in a single experiment before the start of the first physics run of LEP in September, 1989 was 332 by MARK II (310 multihadrons, 13 $\tau^+\tau^-$ and 9 $\mu^+\mu^-$ events) [13]. During the second phase of operation, LEP energies will extend up to and beyond the W^+W^- pair production threshold giving access to the triple gauge boson vertex and allowing a direct study of the non-Abelian nature of electroweak theory to be performed.

Given the high statistics that are attainable at LEP, it is an ideal testing ground for many and varied details of the standard model. A detailed literature exists for both the theoretical expectation [14,15,16] and the experimental measurements—almost one hundred publications have been submitted between the four main LEP experimental groups since the start of data taking. As there are very comprehensive summaries of LEP experimental results available [2,18] only the main results are presented below, most of which are obtained by combining published data from all LEP experiments. These results, which are taken from [2] unless otherwise specified, are:

- The number of standard model neutrino generations, $N_\nu = 2.89 \pm 0.10$.
- The mass of the Z^0, $M_Z = 91.177 \pm 0.031 \pm 0.030$ GeV.
- The total width of the Z^0, $\Gamma_Z = 2.496 \pm 0.016 \pm 0.010$ GeV.
- The hadronic pole cross section, $\sigma_{\mathrm{had}}^{\mathrm{pole}} = 41.78 \pm 0.52 \pm 0.40$ nb.
- The partial width of the Z^0 to hadrons, $\Gamma_{\mathrm{had}} = 1.764 \pm 0.016 \pm 0.008$ GeV.
- The partial width to charged leptons, $\Gamma_l = 0.0837 \pm 0.0011 \pm 0.005$ GeV.
- The strong coupling constant, $\alpha_s = 0.118 \pm 0.008$ [19].
- The minimal Higgs scalar is excluded within $0.0 \leq M_H \leq 44.0$ GeV (at 95% CL) [10].
- The top quark is inferred to have a mass, $M_t = 144^{+39}_{-50}$ GeV (from lineshape measurements), [20].
- The supersymmetric muon (amongst others), is found to have a mass, $M_{\tilde{\mu}} \geq 44.0$ GeV (at 95% CL).

Chapter 2

The LEP collider and OPAL detector

This chapter outlines the major components of the LEP accelerator system and the OPAL detector. The latter is composed of a number smaller sub-detectors each of which is described below. As the offline reconstruction of data from the endcap muon chambers of OPAL forms a large proportion of the technical work for this thesis, a slightly greater emphasis is placed on the description of this particular detector element.

2.1 The LEP collider

The LEP facility is a synchrotron collider designed to annihilate electrons and positrons at centre of mass energies in the range between approximately 80 GeV and 200 GeV with a peak luminosity of $1.7 \times 10^{31}\mathrm{cm}^{-2}\mathrm{s}^{-1}$. It has a circumference of 26.7 km and is accommodated in a tunnel that varies in depth from 51 m to 143 m below the surface of the Franco-Swiss countryside, the large radius being essential to reduce synchrotron radiation losses by the two counter-rotating lepton beams.

In order to span the wide energy range intended, the LEP project is staged in two phases. The first phase relies upon copper accelerating cavities to attain centre of mass energies up to 110 GeV, concentrating on the physics close to the Z^0 resonance, whilst the second phase will utilise superconducting cavities to allow electrons and positrons to reach a maximum of 100 GeV per beam, *i.e.* above the W^+W^- pair production threshold. LEP has been providing physics beams in the

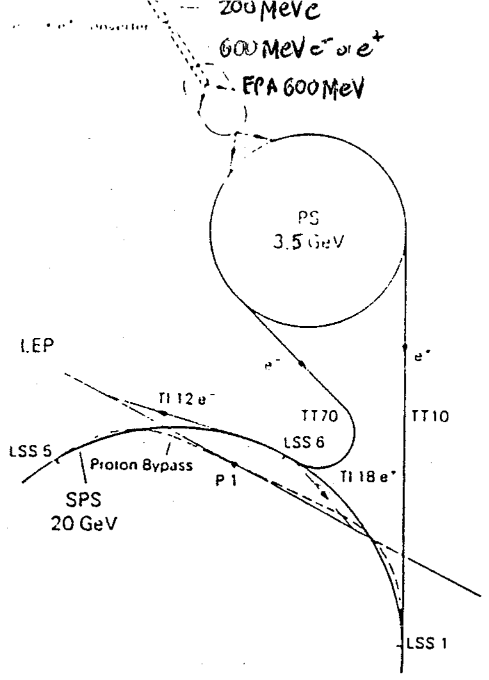

Figure 2.1: The injection and acceleration system for LEP.

region of the Z^0 for almost twelve months at the time of writing. An overview of the elements that are essential to the operation of LEP are outlined below; more detailed descriptions are available in the literature [21].

2.1.1 The injection system

The injection system used to introduce electrons and positrons into the main LEP ring is shown in figure 2.1. It starts with the purpose built LEP Injector Linac (LIL) which consists of two small linacs. The first of these is a high current linac (beam currents approximately 2–3 A) that accelerates electrons from a heated filament to 200 MeV, some of which are directed onto a tungsten target. Positrons are pair produced by bremsstrahlung photons which are emitted during the rapid deceleration that the electrons experience upon impact with the target; shower development within the target results in a positron yield proportional to the energy of the incident electron beam.

The positrons are magnetically separated, accelerated to 600 MeV in the second part of LIL and stored in the Electron Positron Accumulator (EPA) ring. Electrons accelerated to 200 MeV in the first part of LIL are also accelerated to 600 MeV and stored in the EPA. When a sufficiently large number of both species has been accumulated, they are transferred to the Proton Synchrotron (PS) for acceleration to 3.5 GeV prior to injection into the Super Proton Synchrotron (SPS) where the preliminary acceleration to 20 GeV is completed. These beams are subsequently extracted from the SPS and injected into LEP where they are further accelerated to full energy.

2.1.2 The charged particle transport system

To enable the beams to continue circulating for time periods on the order of hours they are transported within the accelerating system inside an evacuated beam pipe; inside the OPAL detector the beam pipe has an internal diameter of 156 mm. In order to maintain acceptable beam luminosity during each fill, the number of contaminating gas molecules with which the circulating electrons and positrons can collide must be kept to an absolute minimum. For this reason the pressure inside the beam pipe is held at approximately 10^{-11} Torr.

To constrain charged particles to a circular orbit in LEP requires 3304 bending (dipole) magnets and almost 2000 focussing (quadrupole, sextupole and octupole) magnets. The LEP machine has an effective bending radius of 3.1 km [22] and thus requires a relatively low average dipole field of 0.05 T to constrain the beams to the required orbit. (For comparison, the average field in the $Sp\bar{p}S$ operating in pulsed mode is nearly 2 T.) As a consequence, it was possible to use specially constructed dipoles with ceramic laminations to significantly reduce the overall cost of the project.

2.1.3 The radio frequency accelerating system

At a nominal energy of 46 GeV an electron loses approximately 128 MeV for each revolution of LEP it performs. Given the large number of particles per bunch (nominal design specification is 4×10^{11}) and four bunch operation of LEP, the energy losses due to synchrotron radiation dominate the large power requirements of the LEP machine. This energy is returned to the beams via radio frequency (RF) cavities [22]. There are 128 RF cavities installed in the straight sections of the LEP ring powered by klystrons. In the first phase of LEP, most of these are copper cavities coupled to 'low loss' spherical storage cavities into which energy is transferred for periods in each operating cycle when no beam is in the RF cavity itself, thus reducing the net power consumption.

In order to reach the design energies for the second phase of LEP it is essential to use superconducting, niobium coated cavities to reduce the energy losses which, being proportional to the fourth power of the beam energy, increase by more than a factor of twenty as the centre of mass energy changes from 92 GeV to 200 GeV.

2.1.4 LEP performance after one year

The LEP machine has improved steadily since the observation of the first Z^0 event by OPAL on Sunday 13th August, 1989. Luminosities of $4.5 \times 10^{30}\mathrm{cm}^{-2}\mathrm{s}^{-1}$ with fills lasting 6 hours were typically delivered towards the end of the 1990 run and current records are $6.8 \times 10^{30}\mathrm{cm}^{-2}\mathrm{s}^{-1}$ and 19 hours for these two parameters.

Four of the eight possible interaction regions of LEP are equipped with large general purpose, experimental detectors. These are known as ALEPH, DELPHI, L3 and OPAL. Two much smaller and more specialised experiments called BREMS and MODAL have been approved and are in preparation. OPAL is one of the detectors which is currently in the process of collecting data and is described below.

2.2 The OPAL detector

The OPAL (Omni Purpose Apparatus for LEP) detector [23] is a general purpose apparatus designed to detect and enable the study of all possible processes that are known to occur in e^+e^- annihilation at LEP energies (except for $\nu\bar{\nu}$ final states) as well as to search for hitherto unknown phenomena. It combines good particle identification and accurate event reconstruction with an outstanding acceptance for Z^0 decays over a solid angle of close to 4π. A perspective view of the OPAL detector is given in figure 2.2, whilst the co-ordinate system, track parameters and derived quantities used throughout this thesis are defined in Appendix A. An overview of the detector is given below followed by a more detailed description of each constituent sub-detector.

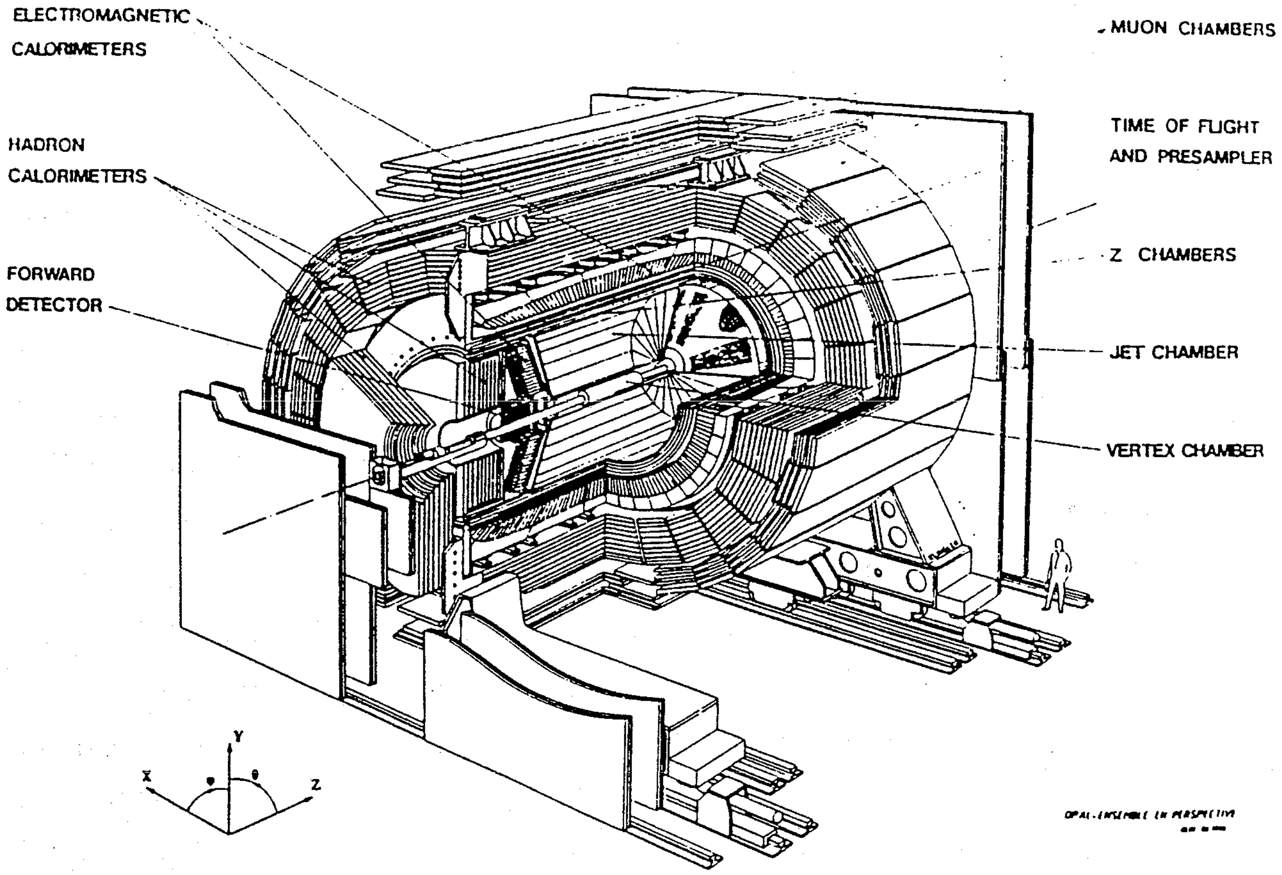

Figure 2.2: A perspective view of the OPAL detector.

2.2.1 Overview of detector components

Tracking of charged particles is carried out in a uniform, solenoidal magnetic field by the central detector (CD) which is a high precision, composite drift chamber. This apparatus is capable of determining particle momentum and the rate of energy loss ($\frac{dE}{dx}$) to aid particle identification as well as being able to reconstruct primary and secondary vertices. The CD is situated inside a pressure vessel at a pressure of 4.0 atmospheres, the pressure vessel having a conventional, warm coil at its outer radius and the beam pipe at the inner radius.

Situated immediately beyond the coil is the time-of-flight (ToF) system. which is used to generate trigger signals and aids both cosmic ray rejection and low momentum particle identification. The electromagnetic calorimeter (ECAL) is situated immediately outside the ToF. The most important part of this is a highly segmented. lead glass device which measures the energy carried by incident photons, electrons and some fraction of the energy carried by charged hadrons. Any particles that manage to traverse the ECAL, which constitutes approximately 20–25 radiation lengths (χ_0) and 2.2 interaction lengths (λ_{Int}), pass into the hadron calorimeter (HCAL) which is actually the iron return yoke of the solenoid instrumented with streamer tubes. Most hadronic showers are initiated in the ECAL making it necessary to combine both ECAL and HCAL signals in order to determine the hadronic energy.

Surrounding the iron of the HCAL, which also acts as a muon filter, are several layers of muon chambers which are used to measure the position and direction of charged particles. Muons are identified by matching these track segments and those within the HCAL with central detector tracks. The final element of OPAL is the forward detector, a composite device which has elements that provide tracking and electromagnetic calorimetry at small angles with respect to the beam axis, in addition to its main (and vital) function of measuring the beam luminosity. The various sub-detectors that comprise OPAL, illustrated in figure 2.3, are described below.

2.2.2 The central detector

The central tracking system of OPAL is composed of a high precision vertex chamber, a large volume 'jet' chamber and z-chambers which measure track directions and curvatures in a solenoidal field and hence determine particle momenta. The three chambers are maintained at a common pressure of 4.0 atmospheres within the pressure vessel and use a gas mixture of 88.2% argon, 9.8% methane and 2.0% isobutane. This is a typical mixture for a gaseous detector where argon is the 'vehicular' gas which is responsible for the multiplication of the initial ionisation signal and the remaining 'quenching' gases break the multiplication chain by

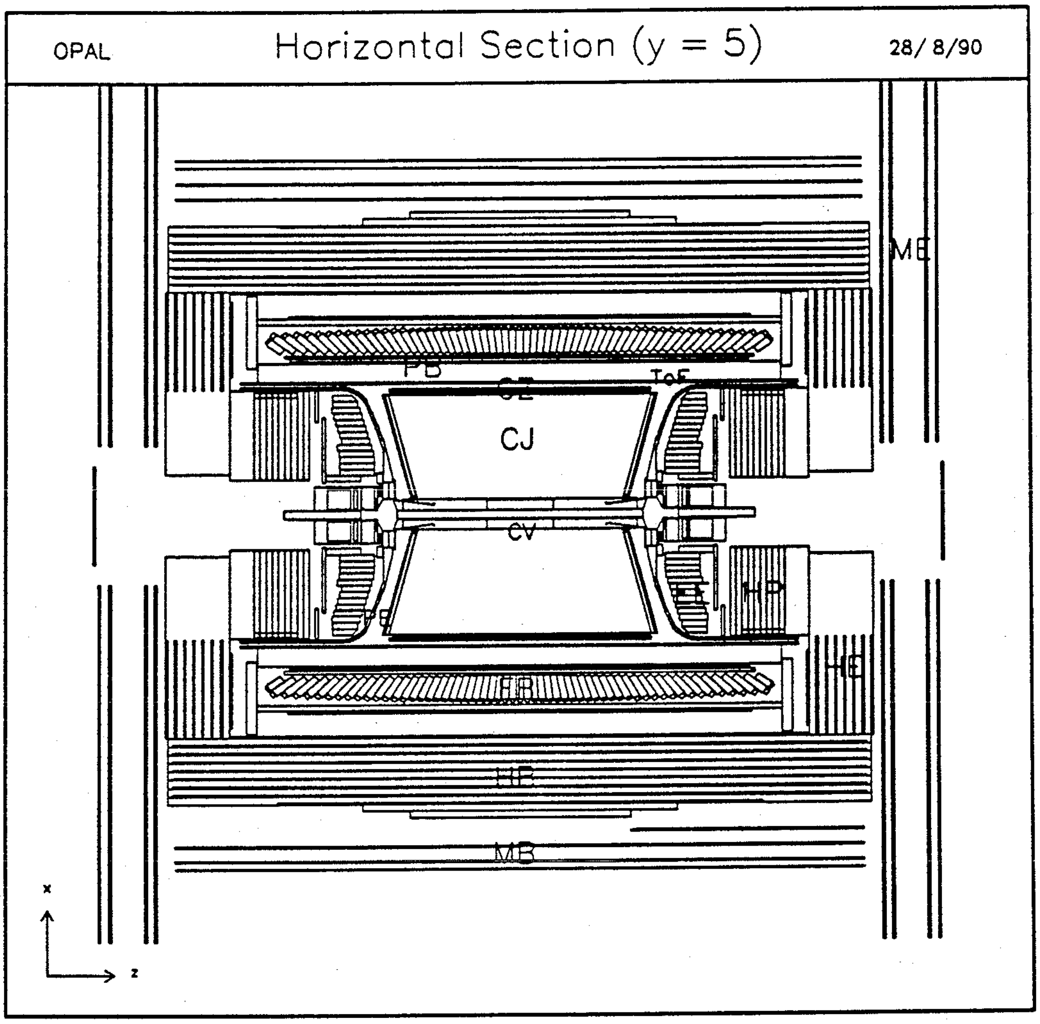

Key
CV: Vertex detector CJ: Jet chamber CZ: Z-chambers
ToF: Time-of-flight
PB: ECAL presampler barrel PE: ECAL presampler endcaps
EB: ECAL lead glass barrel EE: ECAL lead glass endcaps
HB: HCAL barrel HE: HCAL endcaps HP: HCAL poletips
MB: Muon barrel ME: Muon endcaps FD: Forward detector

Figure 2.3: Horizontal section through OPAL at $y = 5$ cm.

absorbing photons [24].

The combined performance of the CD is illustrated by the impact parameter resolutions for dimuon events which have been measured in the r-ϕ plane as $\sigma_{r\text{-}\phi} = 43\ \mu$m and in the r-z plane as $\sigma_{r\text{-}z} = 1.7$ mm. This latter measurement is for tracks which are fully matched to the vertex chamber. If no information from the axial cells of the vertex chamber is incorporated, the resolution is reduced to $\sigma_{r\text{-}z} = 27$ mm. The momentum resolution is found to be 8% at 45 GeV.

The vertex detector

The primary purpose of the vertex chamber is to locate decay vertices of short lived particles and to improve the combined CD momentum resolution. This is a cylindrical chamber, 1 m in length with a diameter of 470 mm, that is divided into two concentric drift volumes each of which is subdivided into 10° azimuthal sectors. The inner drift cells have 12 axially strung anode sense wires with a radial spacing of 5.3 mm from an inner radius of 103 mm and accurately measure azimuthal co-ordinates on a track. The outer cells are small angle stereo cells which ensure a precise determination of z co-ordinates. Each stereo cell contains 6 sense wires, radially separated by 5 mm between radii of 188 mm and 213 mm. The stereo cells are inclined at an angle of $\sim 4^\circ$ relative to the r-z plane. All anode wires are staggered by ± 41 μm to resolve left-right drift ambiguities.

The resultant resolution in r-ϕ is 55 μm whilst in r-z it is 700 μm using both stereo and axial cells or 4 cm in the absence of stereo cell information.

The jet chamber

The main tracking chamber in OPAL is based on a design first used at the JADE detector [25] at PETRA. It has an active volume that is approximately 4 m in length with an inner radius of 25 cm and an outer radius of 185 cm. It is divided into 15° azimuthal sectors, each of which contains a single plane of 159 axially oriented anode (sense) wires. Planes of cathode wires define the sector boundaries. The sense wires are radially spaced at 10 mm intervals between radii of 25.5 cm and 183.5 cm, alternating with potential wires, and are staggered by ± 100 μm either side of a given plane of potential wires to resolve left-right ambiguities. The potential wires are normally maintained at a voltage of -2.38 kV, which determines the gas gain in the chamber (approximately 10^4).

As in the other components of the CD, charged particles passing through the active volume ionise gas molecules and liberate electrons. These electrons drift towards the sense wires in the electric field created by the cathode wires resulting in a pulses which are read out at either end of the sense wires. As the maximum drift distance varies with radial displacement from the beam axis up to a maximum of 25 cm at the outer wires, the voltage applied to the cathode planes increases with radius in order to maintain a uniform drift potential. The cathode planes are supplied with voltages between −2.5 kV on the inner wires and −25 kV on the outer wires whereas all anode wires are at ground potential. A three-dimensional co-ordinate is determined for each reconstructed point, where the drift time and wire position measure the position in the r-ϕ plane and charge division along the sense wire determines the z co-ordinate.

The rate of energy loss of a particle in the chamber gas, $\frac{dE}{dx}$, is calculated using the variation of the sum of integrated charges from both ends of sense wires that define a reconstructed track. The resolution of $\frac{dE}{dx}$ in the angular region $|\cos\theta| < 0.8$ is 3.8% for particles in the momentum range 0.5–1.0 GeV. The average resolution in r-ϕ is 135 μm whilst in r-z it is 6 cm. The momentum resolution is characterised by $\sigma_p = 2.2 \times 10^{-3} p^2$, which is approximately 10% at 45 GeV.

The z-chambers

The z-chambers provide an accurate z co-ordinate for the end point of a central detector track in the angular region $|\cos\theta| < 0.72$. They are mounted on the outer surface of the jet chamber in a barrel shaped configuration. Each one of the 24 drift chambers is 4 m long, 50 cm wide, 5.9 cm thick and is divided into 8 50 cm × 50 cm active volumes. There are 6 sense wires strung in an azimuthal direction in the middle of each cell so that the z co-ordinate is accurately determined by the drift time measurement. The maximum drift distance is 25 cm. The radial separation of the sense wires is 4 mm with a stagger of ± 250 μm to resolve left-right ambiguities. The azimuthal co-ordinate is deduced from charge division.

The resolution in r-ϕ has been measured at 15 mm whereas the absolute resolution in r-z is approximately 100–350 μm, being limited by the accuracy with which the chambers have been surveyed *in situ* in the experimental hall.

2.2.3 The time-of-flight system

The time-of-flight counters provide OPAL with fast trigger signals, aid the rejection of cosmic rays and contribute to the identification of low momentum charged particles. This sub-detector consists of 160 scintillation counters of length 6.84 m which form a barrel of radius 2.36 m immediately outside the coil and covers the region $|\cos\theta| < 0.82$. The timing resolution achieved using the ToF is found to be 460 ps for muon pair events and, by comparison with other sub-detectors, the z resolution is determined to be 75 mm.

2.2.4 The electromagnetic calorimeter

The purpose of the electromagnetic calorimeter is to detect and measure the energy of electrons, positrons and photons as well as making a partial energy measurement for charged hadrons. It is capable of electron-hadron discrimination if tracking information is available as well as π^0-photon discrimination. The largest part of this device is a highly segmented ensemble of lead glass blocks which form a homogeneous (as opposed to sampling) calorimeter that covers 98% of 4π. Lead glass is a very attractive material for a calorimeter due to its good intrinsic energy resolution ($\frac{\sigma_E}{E} \sim \frac{5\%}{\sqrt{E}}$ with E in GeV), linearity, gain stability, spatial resolution and high granularity.

Electrons or photons incident upon the active material start showers by the processes of pair production and bremsstrahlung. Some fraction of the particles in each shower will be travelling faster than light in the active material, resulting in Čerenkov radiation being produced. This radiation, collected by a photomultiplier tube at the outermost face of each block, is proportional to the energy of the incident particle.

As there is a substantial amount of material in front of the lead glass calorimeter in the form of the coil and pressure vessel ($\sim 2\ \chi_0$) most electromagnetic showers start to develop before entering the lead glass array. To partially compensate for this, presampling detectors are located directly in front of the lead glass to measure the position and extent of clusters as well as to sample their energy. The energy resolution and discriminatory power of the calorimeter is significantly improved by the use of the presampler. The energy resolution of the lead glass without any material in front, $\frac{\sigma_E}{E}$, is approximately $\frac{6.3\%}{\sqrt{E}} + 0.2\%$ in the barrel and $\frac{5.0\%}{\sqrt{E}}$ (E in GeV) in the endcap region. With the $2\ \chi_0$ of material in front of the lead glass, this resolution is degraded by a factor ≈ 2 at 6 GeV. By using presampler information, the loss in energy resolution may be restricted to a factor ≈ 1.5 and the spatial resolution obtained for an electromagnetic shower is 2–5 mm. (The presampler was not fully operational in 1990.)

The electromagnetic presampler

This has barrel and endcap components and provides almost complete coverage in the angular region $|\cos\theta| < 0.95$. The former is composed of two layers of plastic streamer tubes (based on [26]) operated in limited streamer mode, and the latter out of narrow proportional chambers. The barrel readout uses charge induction onto external strips, placed at ±45° to the sense wire direction as well as charge division along the sense wire. The endcap readout is of a similar design using pads and strips. The intrinsic spatial resolution, averaged over endcap and barrel, is 2–3 mm for single, minimum ionising particles.

The lead glass electromagnetic calorimeter

This detector is geometrically divided into barrel and endcap regions and encompasses the region defined by $|\cos\theta| < 0.98$. The active material of the calorimeter is lead loaded glass (50% by weight).

The barrel consists of a cylindrical array of 9440 blocks arranged in an 'almost pointing' geometry of 59 azimuthal rings, each of which contains 160 blocks (see figure 2.4). Complete coverage is provided in the region $|\cos\theta| < 0.82$. The blocks do not point exactly back to the origin in either θ or ϕ to prevent particles from passing undetected through inter-block gaps. The blocks are situated at a radius of 245.55 cm and are read out using phototubes that are insensitive to the relatively low magnetic field (0.01 T) in this region. Each block has a square cross section with length of side 10 cm and an average length of 37 cm, corresponding to 24.6 χ_0.

Each endcap contains 1132 blocks arranged parallel to the beam axis, where constituent blocks have a square cross section with length of side 9.2 cm and are variously 38 cm, 42 cm or 52 cm long. An endcap presents a minimum depth of 20.5 χ_0 to incident particles from the origin in the range $0.81 < |\cos\theta| <$

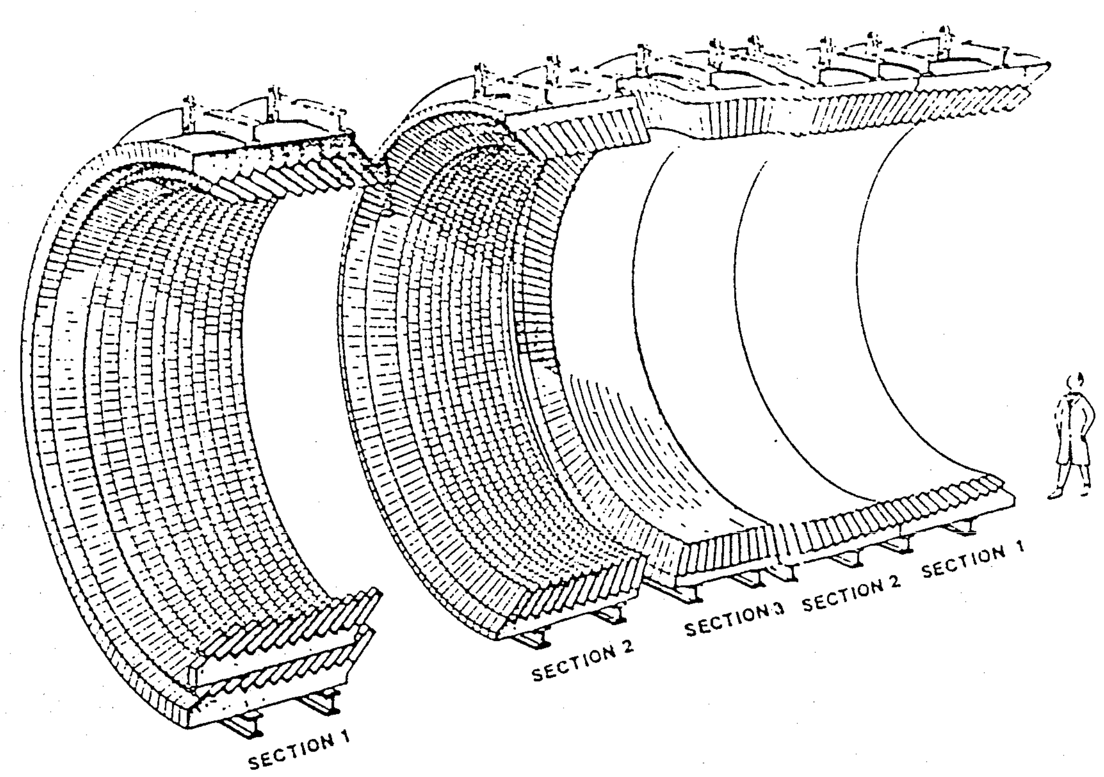

Figure 2.4: Perspective view of one half of the lead glass barrel.

0.98. Vacuum photo triodes (VPTs) [27] are used to read out each block which is necessarily located in the full axial field of the coil. Both barrel and endcap detectors have elaborate systems of calibration and monitoring, involving xenon flash tubes (barrel) and light diodes and UV lasers (endcaps).

The spatial resolution of the lead glass system is approximately 11 mm. It is possible to obtain a resolution of less than half of the width of an individual block by studying the lateral profile of electromagnetic showers, which are not normally confined to a single block. The intrinsic energy resolution of the system, $\frac{\sigma_E}{E}$, is $\frac{5\%}{\sqrt{E}}$ in the endcaps and $\frac{6.3\%}{\sqrt{E}} + 0.2\%$ in the barrel.

2.2.5 The hadron calorimeter

The hadron calorimeter measures the energy of hadrons that emerge from the ECAL and provides valuable information for the identification of muons. The HCAL is particularly important for measuring the neutral hadronic energy component, which is measured to a lesser extent by the ECAL. In order to provide a

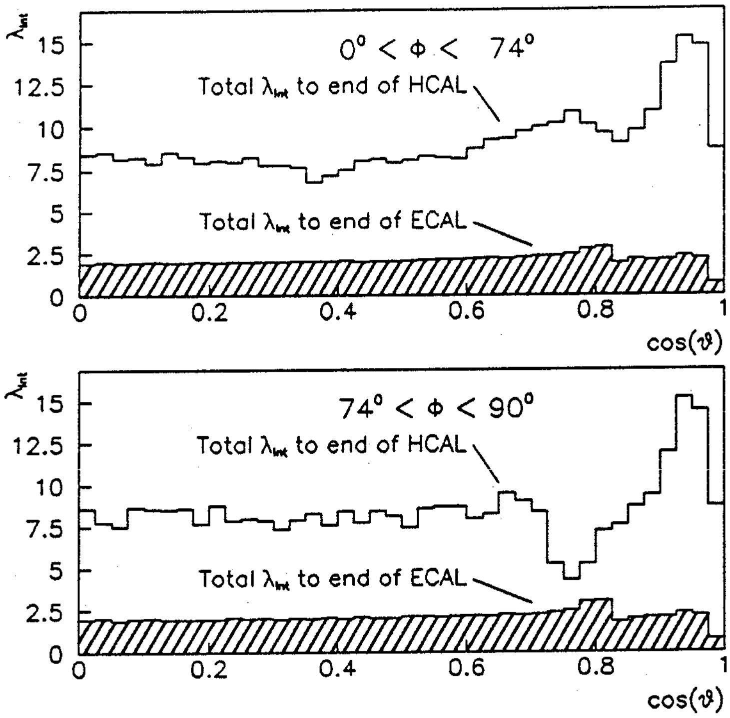

Figure 2.5: Distribution of material in OPAL from Monte Carlo.

hermetic and relatively accurate measurement of the energy of hadronic showers, as well as to reduce the non-muon particle flux reaching the muon chambers, the HCAL has a large acceptance which covers 97% of the solid angle with more than 4 λ_{Int} (see figure 2.5).

It is a sampling calorimeter formed by instrumenting the iron layers that constitute the return yoke of the coil. Gaseous detectors are placed between these layers and are read out by a system of pads and narrow strips. The energy of a hadronic shower is sampled by the active gas detectors after the shower has traversed successive layers of passive iron absorber. The pads are arranged in geometrical 'towers' pointing back to the origin with the width of pads varying from layer to layer. The pads are read out after being summed in depth within each tower whilst the innermost pad is also read out separately. The strips provide tracking information for minimum ionising particles and are used to map shower profiles.

The energy resolution of the HCAL is limited by the amount of material in front of the detector ($\sim$ 2.2 λ_{Int}), most of which is present in the ECAL (see figure 2.5). As a large fraction of hadronic interactions will be initiated in this amount of absorber and the ECAL is not compensated[1] it is necessary to combine the ECAL and HCAL signals using an appropriate ansatz to fully reconstruct the hadronic energy in an event. The resultant hadronic energy resolution, $\frac{\sigma_E}{E}$, is $\frac{120\%}{\sqrt{E}}$.

The HCAL is divided into barrel, endcap and pole-tip regions. The HCAL barrel region is defined by $|\cos\theta| < 0.81$, the endcap region by $0.81 < |\cos\theta| < 0.91$ and the poletip by $0.91 < |\cos\theta| < 0.99$ The endcap and barrel hadron calorimeters are similar in that they both use limited streamer tubes [26] with a gas mixture of 25% argon and 75% isobutane as the active elements and have iron layers that are 10 cm thick. The barrel is segmented into 15° azimuthal sectors, each of which contains 8 plates of absorber and 9 layers of streamer tubes between radii of 339 cm and 439 cm. The streamer tubes are read out by 1 cm wide strips parallel to the axially oriented anode wires and by large area pads, typically 50 cm × 50 cm. The pads form 1152 towers.

The endcap is an annular device with an outer radius of 320 cm composed of 7 iron plates and 8 sampling regions. It is read out by strips and pads, the latter forming 192 towers. Both barrel and endcap have a 20 cm thick layer of iron after the last sampling to enhance the muon filter. The geometric tower arrangement of pads in the endcap and barrel divide the solid angle into 976 equal elements, with 48 bins in ϕ and 21 in θ.

The pole-tip extends the HCAL coverage as far as $|\cos\theta| = 0.99$ and uses 10 iron plates, each 8 cm thick, and 10 samplings. (This very marginally improves the energy resolution in the region where the CD momentum resolution starts to deteriorate, but not significantly so.) The active elements are narrow gap proportional chambers filled with 45% n-pentane and 55% carbon dioxide. The overall thickness of each element is 7 mm. The wire chambers are read out with pad towers and radially arranged strips. A 30 cm thick layer of iron on the rear surface of the pole-tip reduces the hadronic flux reaching the muon chambers.

---

[1] Hadronic showers do not develop in the same way as electromagnetic showers. Most of the secondaries produced by hadrons interacting in the ECAL travel at speeds below the Čerenkov threshold and so an accurate measurement of the hadronic energy is not possible in the ECAL.

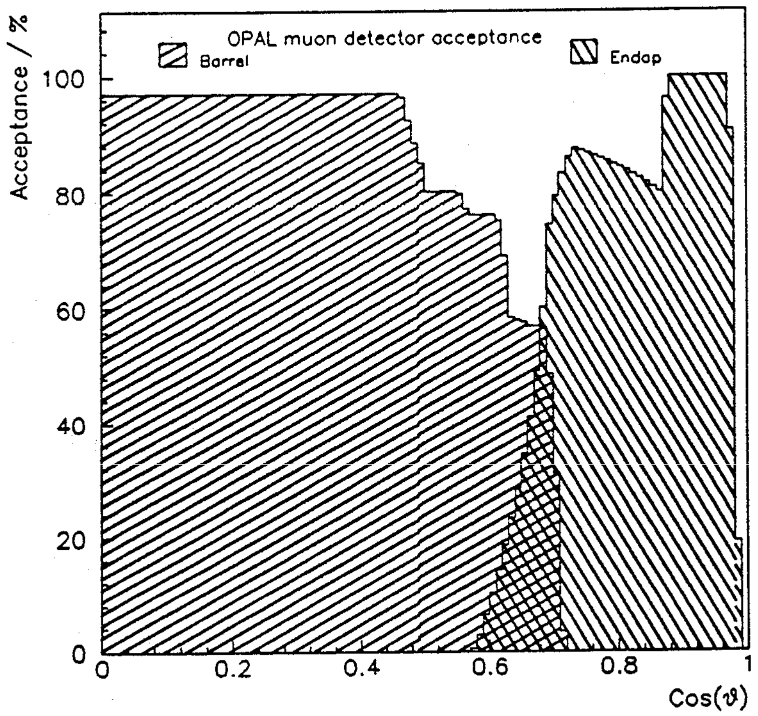

Figure 2.6: Geometric acceptance for muon detectors, averaged over ϕ.

2.2.6 The muon chambers

The muon chambers are used to measure the position and direction of charged particles that manage to penetrate the material of the ECAL, HCAL and additional iron absorber outside the HCAL. Track segments in these chambers are matched in position and direction with CD tracks to identify muons, taking into account the effects of multiple scattering and energy loss in the absorber. Hadrons reaching these chambers may therefore be misidentified as muons. As there are more than 7 λ_{Int} in front of the muon system over a large fraction of the solid angle (see figure 2.5) the probability of a hadron reaching the muon system without strongly interacting is small ($\sim$ 0.1%). (A large fraction of the regions in which the amount of absorber in front of the muon chambers is significantly less than 7 λ_{Int} correspond to areas of reduced acceptance of the muon chambers themselves.) Secondaries from strong interactions in the absorber and from in-flight decays dominate the hadronic background.

The muon system is divided into endcap and barrel regions and covers approximately 94% of 4π. the loss in coverage being necessary to allow for support

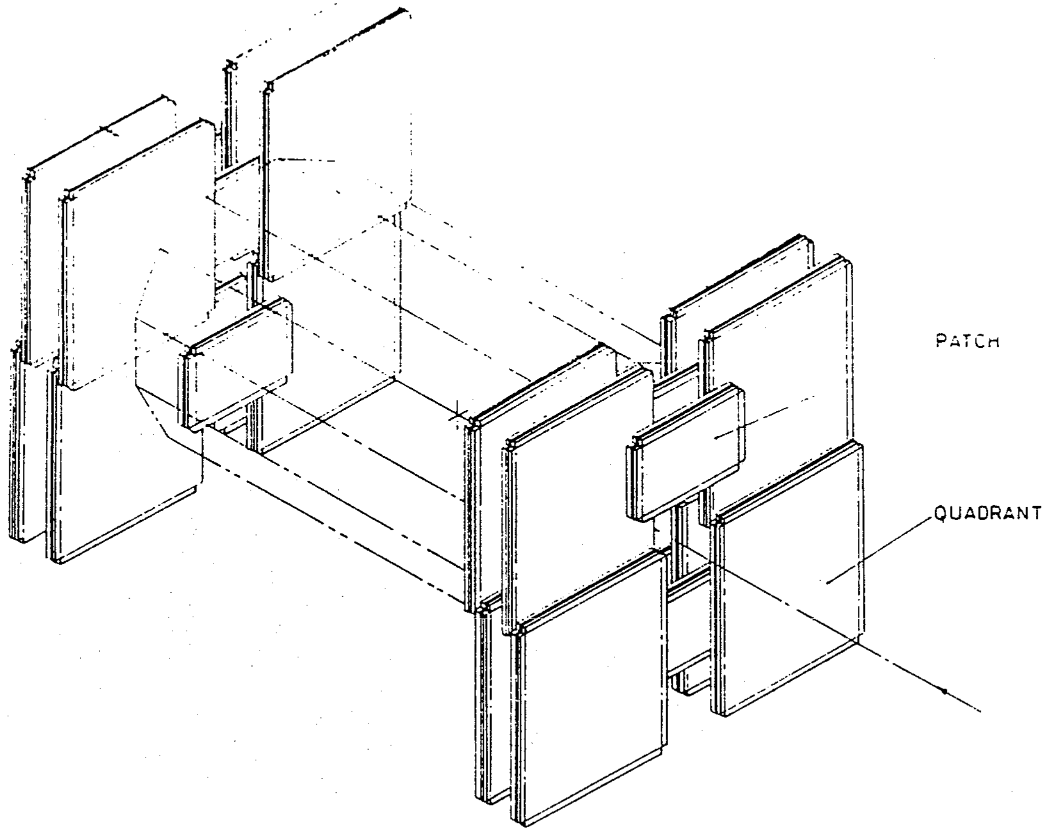

Figure 2.7: The endcap muon detector.

structures, cables and the beam pipe. The geometric acceptance (averaged over ϕ) inside which track segments may be reconstructed in the endcaps and barrel is shown in figure 2.6. Both sub-detectors consist of 4 layers of gaseous detectors and the active area of each covers an area of approximately 1200 m^2

The muon barrel detector consists of 110 drift chambers developed from a design used at JADE [28]. Each chamber is 1.2 m wide, 90 mm thick and variously 10.4 m, 8.0 m or 6.4 m in length and is divided into two lateral drift cells of width 60 cm, both of which contain a single sense wire parallel to the beam axis. The gas mixture used is 90% argon and 10% ethane. The chambers are arranged to form a cylinder 4 layers deep, outside and coaxial with the HCAL barrel, staggered by ±50 mm in ϕ to resolve drift ambiguities. The drift time determines the r-ϕ co-ordinate to an accuracy of 1.5 mm. The z co-ordinate is estimated using a timing measurement from the sense wires and a novel system of diamond shaped pads [29] placed above and below each wire. This arrangement is intrinsically capable of determining the z co-ordinate with an accuracy of 1.5 mm.

The muon endcap (ME) detector is composed of two large structures placed at either end of the OPAL detector. An endcap consists of two planes of detectors perpendicular to the beam axis and separated by 65 cm. Each of these planes. which measures 13 m × 13 m. is constructed from 4 'quadrants' and 2 'patches' as shown in figure 2.7. This arrangement ensures a large coverage of the solid angle, particularly at small polar angles, without unduly impeding access to the inner sub-detectors for cables and maintenance. For reasons of conciseness, the term 'quadrants' will be used to refer to both quadrants and patches unless it is necessary to make a distinction between them. The active detector elements used are limited streamer tubes having a square cross section of 9 mm and typical length of 6 m (in the quadrants) or 2.5 m (in the patches). The endcap muon system in total contains 21248 such elements.

The chambers operate on a gas mixture of 25% argon and 75% isobutane and are read out by measuring the charge induced onto 9 mm wide aluminium strips placed on either side of the streamer tubes, oriented parallel and perpendicular to the anode wires. The anode wires are not read out and the streamer positions determined by parallel and perpendicular strips for a given hit are essentially independent of one another, *i.e.* each layer of streamer tubes measures two (orthogonal) 2-dimensional co-ordinates. The resolution of the parallel strips is approximately 3–4 mm whilst that of the perpendicular strips is 1–1.5 mm. Full details of various aspects of this sub-detector are available elsewhere [24,30,31].

Each plane contains two orthogonal layers of streamer tubes and therefore determines two xz and two yz co-ordinates. The planes are referred to hereafter as 'inner' and 'outer' (with respect to the vertex) and 'upper' and 'lower' (with respect to the xz plane) if it is necessary to make a distinction between them.

2.2.7 The forward detector

The forward detector measures the luminosity of LEP in the region of the OPAL experiment by detecting small angle Bhabha scattering into a region with an accurately known acceptance, as well as tagging electrons from 2-photon interactions. As small angle Bhabha scattering is well described theoretically and the cross section integrated over a given solid angle close to the beam axis is calculable, the

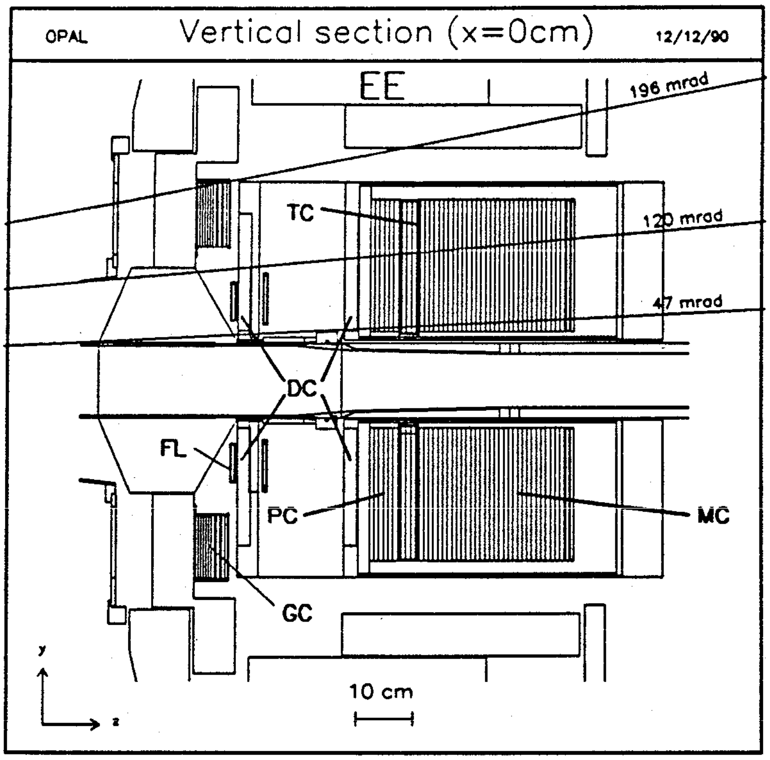

Key
(DC) Drift chambers (TC) Proportional tube chambers
(GC) Gamma catcher (FL) Fine luminosity monitor
(PC) Presampler calorimeter (MC) Main calorimeter
(EE) ECAL (lead glass) endcap

Figure 2.8: Vertical section through the forward region of OPAL at $x = 0$ cm.

number of observed events is an absolute measure of luminosity.

The forward detector consists of two identical sets of tracking and electromagnetic calorimeter elements located at either end of OPAL. In total, polar angles from 40 to 220 mrad are covered by this device with unobstructed coverage (apart from the carbon fibre beam pipe, a 2 mm aluminium window in the CD pressure vessel and support struts for the beam pipe) in the region from 47 to 120 mrad. The largest part of the forward detector is between $|z| = 205$ cm and $|z| = 290$ cm and is composed of a 29 layer, 20 χ_0 calorimeter, a 6 layer, 4 χ_0 pre-sampling calorimeter, three sets of tracking chambers, a fine luminosity monitor consisting of 4 pairs of 6 mm thick precision scintillators and a ring shaped 7 χ_0 calorimeter called the 'gamma catcher'. The layout of these components is illustrated in figure 2.8. The figure is a section through the main part of the forward detector in the $x = 0$ plane which does not intersect with the fine luminosity monitors, which are positioned at $\phi = \frac{\pi}{4}$ modulo $\frac{\pi}{2}$. For illustration, they have been projected onto this plane and included in the figure. The second part of the forward detector consists of the far forward luminosity monitors. These are small 20 χ_0 calorimeters located 7.85 m from the intersection region.

The calorimeters are made from a lead-scintillator sandwich and are divided into 16 azimuthal segments. Two of the tracking chambers are radial drift chambers and the third is an array of proportional tube chambers. The radial resolution of the drift chambers is approximately 300 μm, whilst that from the calorimeter is 2 mm. The azimuthal resolution of the calorimeter (from energy sharing between adjacent segments) is less than 1.5° and the energy resolution of the calorimeter, $\frac{\sigma_E}{E}$, is approximately $\frac{17\%}{\sqrt{E}}$.

The best luminosity determination in 1990 (which is used in this thesis) utilises all components of the forward detector. The relative luminosity between different energy points is measured by the main calorimeter as this component accumulates the highest Bhabha statistics, whilst the weighted average of two different determinations of the absolute normalisation determine the final normalisation to be used for the main calorimeter luminosity. The first method of determining the absolute normalisation uses the fine luminosity scintillators alone, whilst the second method uses the tube chambers, the calorimeter and the drift chambers. This latter procedure uses the precision drift chambers to improve upon the position survey of the tube chambers and the calorimeter to provide redundancy for the angular measurement, to remove spurious tube clusters and to reduce the inefficiency to less than 0.3%. The end products of the involved procedure are systematic uncertainties in the relative luminosity measurement of 0.8% and in the absolute normalisation of 1.0%.

Chapter 3

Event reconstruction in the muon endcaps

The purpose of event reconstruction is to convert 'raw' data recorded by the OPAL detector into quantities such as energies, momenta and vertices that characterise the original collisions which were selected by the triggering system (described in chapter 5). The reconstruction of these collisions within OPAL is carried out by a large computer program called `ROPE`[1] [32], which is run in an online environment as the last stage of the data acquisition system.

The main objective of this chapter is to describe the reconstruction of data within the muon endcaps, which are a typical OPAL sub-detector. It therefore begins with a brief overview of how OPAL events are reconstructed and is followed by a detailed description of the muon endcap reconstruction process. The latter includes the algorithms used, the treatment of calibration and processing parameters and a discussion of the tuning of the reconstruction algorithms. The final section presents a comparison of the reconstruction of real and Monte Carlo data to illustrate that the muon endcaps are well simulated and thoroughly understood.

3.1 Overview of OPAL event reconstruction

The purpose of `ROPE` is to produce data summary tape (DST) records for each event which contain as much information about the original event as it is possible

---

[1] Reconstruction of OPAL Physics Events

to extract from the raw data. As the raw data produced by the actual detector and Monte Carlo are treated in the same way by `ROPE`, all references to 'data' are used to mean input from either source. The Monte Carlo simulation of the detector, called `GOPAL` [33], is based upon the `GEANT3` package [34] which allows the detector to be described in terms of a set of standard three-dimensional shapes. `GEANT` also performs the tracking of particles through the detector so defined and simulates various secondary physics processes including particle decays, scattering and interactions. In order to use the simulation for analysis purposes `GOPAL` data must reproduce the observed response of the OPAL detector to real particles, as is shown later in this chapter.

The reconstruction process is divided into a number of self-contained units of software or *processors* in `ROPE`, leading to an overall program organisation that is modular. There are 30 such processors at the present time with well defined tasks that may be grouped as follows:

- Reconstruction within individual sub-detectors, such as the muon endcaps.
- Association and merging of information from related sub-detectors, such as muon endcaps, muon barrel and hadron calorimeter strips.
- Global merging and production of event summaries, *i.e.* DST generation.
- Provision of utility services such as access to calibration data, the three-dimensional interactive event display program (`GROPE`[2]), monitoring of event statistics and so forth.

These processors are driven by a kernel of steering routines, which initiate three types of activity in each processor. These are:

1. 'Initialisation', in which defaults that will remain in effect for the duration of a job are defined and `FFREAD` cards are initialised. (`FFREAD` data cards [35] are a convenient way of selecting options, such as the processors that should be used or the datasets to be read, in a format-free way and are used extensively in `ROPE`.)

---

[2] Graphical Reconstruction of OPAL Physics Events

2. 'Processing', in which events are read into memory and reconstructed.

3. 'End', in which processing terminates. Examples of tasks that are performed are the creation of statistical summaries of the processor performance, the printing of histograms and the production of updated calibrations for use in subsequent jobs.

As reconstruction requires a detailed knowledge of the apparatus, each subdetector group provides a set of subroutines that comprise a processor to reconstruct data from the corresponding detector element. The muon endcap processor (ME) is described in detail below. To facilitate this description, the data structure, within which all reconstruction takes place, is first outlined. Details are available in the literature cited.

3.1.1 Data structure

The `ROPE` data is maintained by the `FORTRAN` memory manager `ZEBRA` [36] in a series of banks which are spread over three divisions in memory. Each division contains a unique top level bank from which subsidiary banks are hung, containing either items specific to sub-detectors, such as the raw data or reconstructed quantities, or more global information such as statistics or details of files being read. The three divisions contain the following data structures:

Statistics structure This is contains information about the processing of a given job. The data accumulated includes status messages (*e.g.* errors, successes and warnings), the average numbers of reconstructed tracks or the amount of memory used for each processor where appropriate. The statistics structure is created during the initialisation phase of the program.

Constants structure This contains the processing parameters for a given job, such as the processors which are to be activated and the calibrations and survey information that are common to many different jobs. The calibrations are maintained in a central direct access database in which all data is stored in association with a period of validity. This allows the 'best' calibrations and processing parameters to be varied to reflect changes that occur during data taking, such as drifts in pedestal levels or periods of high beam related background. In principle, calibrations can be varied on an event-by-event basis.

Event structure This contains the raw data and the results of the reconstruction process, such as the DST records.

For completeness, it is noted that as most of the software mentioned above must necessarily function on several different computer operating systems, it is written in `FORTRAN 77` [37] and required to conform to a strict set of conventions [38]. The code management system `PATCHY` [39] is used to maintain this suite of programs as well as to incorporate machine dependent features, most of which are associated with the input and output of data, where they are unavoidable. Having summarised the main features of `ROPE`, and to a lesser extent those of `GOPAL`, the description of the ME processor now follows.

3.2 Algorithms

The reconstruction process is divided into two entirely separate tasks, *viz.*

- The determination of *hits* in the OPAL co-ordinate system from the raw data, where a hit in the muon endcaps is a two-dimensional xz or yz co-ordinate.
- The formation of the best *track segments*[3] possible for a given set of hits.

These tasks are implemented as two sets of subroutines both of which are called from a steering routine (`MEBAT`). Other routines are present in the reconstruction software which are responsible for the handling of calibration data and processing parameters. A summary of the calling sequence of the subroutines present in the ME processor is presented in figures 3.1 and 3.2. Descriptions of the algorithms involved are given below.

---

[3] In this chapter, a segment or track segment is used to mean a three-dimensional track in a particular sub-detector. Track segments from different sub-detectors are combined to make a complete track. Two-dimensional track segments will be explicitly referred to as 2d-segments.

```
"ROPE"                 ROPE steering routines.
    |
============== Initialisation level =============
    |---MEINIT          Initialise defaults.
    |       |---MEDEFF  Define FFREAD cards.
    |---MESETR          Book histograms and set run parameters.
================ Processing level ===============
    |---MECALR          Read calibrations and parameters from database.
    |       |---MECLNK  Check data structure integrity.
    |       |---MECFLI  Option: Read new calibrations for testing?
    |       |       |---MESVNO Option: Interpret test calibrations?
    |       |---MEUPCO  Update processing parameters where appropriate.
    |       |---MEDABS  Option: Validate current survey information?
    |---MEBAT           Convert raw data to track segments.
    |       |---MEDICN  Find hits present in (packed) raw data.
    |       |       |---MESTCO  Convert strip number to OPAL co-ordinates.
    |       |---MEPATR  Find and fit track segments.
    |       |------>>>  Perform "PASS 2" processing?? (See Appendix B.)
    |---MEDROP          Tidy up intermediate processing results.
================== End level =================
    |---MEFIN           Close down after processing of all events.
            |---MECHCO  Option: Check any requests to save calibrations.
            |---MEUPCO  Option: Obtain best current calibrations.
            |---MECARZ  Option: Save calibrations to database on request.
            |---MECFLO  Option: Save calibrations to file on request.
```

Figure 3.1: Decomposition of the ME reconstruction process into subroutines.

```
MEPATR                 Find and fit track segments.
    |---MEINDX          Construct cross reference tables for hits.
    |---MESEG           Pattern recognition: form 2d-segments from hits.
    |       |---MELSF   Perform weighted least squares fit for 2d-segments.
    |               |---MEBITS Encode list of quadrants for hits on
    |                          2d-segments.
    |---MEDIRC          Combine 2d-segments to form 3d-segments.
    |       |---MECOMB  Decide which 2d-segments may be combined to form
                        3d-segments.
```

Figure 3.2: Detailed decomposition of segment finding process into subroutines.

3.2.1 Hit finding algorithm

Two different reference frames are used in the reconstruction of hits within the muon endcaps. These are the OPAL or 'master co-ordinate' frame, which is illustrated in figure 2.2, and the muon endcap 'local co-ordinate' system, where a 'local' co-ordinate is a point measured within (and relative to the edges of) a given quadrant. The raw data used by this processor is an ordered list of integers containing details of readout strips that are considered to be above threshold and the digitised charges on each such strip.

In order to locate hits searches are made for maxima separated by levels of reduced activity, where the level of reduction or 'step-down' is a parameter that has been optimised. The distribution of pulse heights around a muon track in these chambers is different for readout strips that are parallel and perpendicular to the anode wires of the streamer tubes. In the case of the perpendicular readout, the pulse distribution can be described by two gaussians having a common centroid and full width half maxima (FWHM) of 2–3 strips and 8 strips. In the parallel case, the pulse shape can be approximately described as a gaussian with FWHM of 2–3 strips. These pulse shapes are modelled in `GOPAL`.

After all the hits have been found, their local co-ordinates are transformed into the master frame. To do so, it is essential that the position of the muon endcaps relative to the rest of OPAL and the location of readout strips within a given quadrant are accurately known. These vital dimensions are obtained from a precise ($\sim$ 1 mm) survey of the chamber positions after installation in the experimental area underground. This was hindered by the proximity of the both endcaps to the walls of the experimental hall, with access to triangulate measurements somewhat restricted.

The xz and yz co-ordinates and a 'quadrant number' which uniquely identifies the quadrant or patch in which they are found are passed on as input for the segment finding process. Despite the muon endcaps containing 42496 readout channels, the level of noise within the chambers is sufficiently low that in a sample of approximately 4000 events recorded in normal data taking conditions, the online digital signal processor (DSP, see [24] for details) only found an average of 21 hits

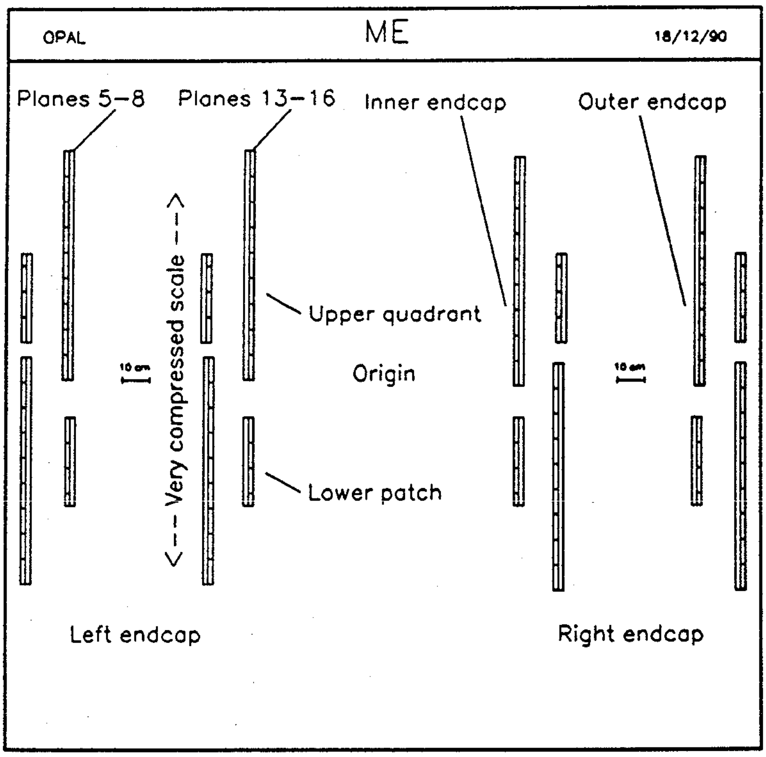

Figure 3.3: Vertical section of the muon endcaps at $x = 0$cm, expanded in z.

per event. For comparison, an ideal muon pair event would produce 16 hits. The hit finding described above is an offline analogue of the DSP process, although the exact algorithm used is different in the two cases. The method described above is such that a strip with no recorded pulse height in the midst of a peak will not prevent that peak from being located, although there will necessarily be a small shift in the centroid.

3.2.2 Segment finding algorithm

The philosophy adopted in the segment finding process is that, at the level of a sub-detector processor, finding the occasional excess of segments is preferable to not finding all of the genuine segments. This will maintain a high efficiency in the muon endcaps although it will occasionally complicate matters for processors that try to associate these track segments with those in other sub-detectors.

As the hits produced by the hardware are two-dimensional objects, the segment finding is carried out independently in two projections (xz and yz). Figure 3.3 illustrates the definition of the so-called *logical planes*, as opposed to *strip planes*, a more hardware oriented grouping of the readout system: each endcap contains eight xz and eight yz logical planes. Herein, 'planes' will be used to refer to logical planes. Each logical plane is composed of all the readout strips located at a given (nominal) z co-ordinate. There are four sets of planes corresponding to two projections and endcaps at $z > 0$ and $z < 0$: all 2d-segment finding is performed in the framework of a given set of planes.

2d-segment formation

The basic idea involves considering planes in pairs and taking all possible combinations of two hits, one from either plane, each such pair of hits defining a straight line. These lines are then extrapolated to the next plane, where a search is made for a third hit that is consistent with being on the same straight line. For this to be the case, the third hit must be within some tolerance of the point of intersection of the original line and the third plane. This tolerance is called a *road*. If any 2d-segments can be constructed that contain three hits, then the same procedure is carried out for the fourth plane, and similarly up to the eighth plane. The result is a list of 2d-segments, defined by their constituent hits.

This operation is then repeated iteratively, each time starting with a different pair of planes, until all combinations have been exhausted. Hits that are not contained in any 2d-segment are noted as such for later use. In general, 2d-segments may contain between two and eight hits although for most of the active area of the detector the maximum possible is four hits. Small regions of overlap between quadrants and patches (approximately 6% of the area of the chambers at normal incidence) as illustrated in figure 3.3 allow the increased hit multiplicity. Two hit 2d-segments can only be formed if one hit is in the inner part of an endcap, the other in the outer part *and* if neither of the two hits is included in another 2d-segment with greater than two hits.

2d-segments are then compared with one another to remove any double counting that may have occurred as a result of the comprehensive search procedure described above. Any in which the constituent hits form a subset of those in another (larger) 2d-segment are discarded, on the assumption that the larger one has a greater likelihood of being genuine. Those remaining are then fitted using a weighted least squares procedure. As the fitting process requires a relatively large amount of computation, attempts are made to eliminate spurious segments before fitting commences.

By default, 2d-segments that do not extrapolate back to the CD volume are removed, although this check can be bypassed to allow non-pointing cosmic rays to be reconstructed. Further duplication may still exist, *e.g.* use of too small a road will occasionally cause a 2d-segment to manifest itself as two smaller ones. This behaviour is illustrated later in this chapter. To help reduce this effect, whenever 2d-segments have the same gradient *and* ordinate within errors ($\pm 3\sigma$ added in quadrature), only the one possessing the highest χ^2-probability[4] is retained. The algorithm thus far has produced and fitted what are considered to be the 'best' 2d-segments for a given set of planes and a set of unused hits that do not appear in any 2d-segment. Attempts are made to incorporate unused hits in segments during the merging of muon endcap data with other sub-detectors.

3d-segment formation

The series of steps outlined above is carried out sequentially for each of the four sets of planes (xy and yz projections at $z > 0$ and $z < 0$) that contain hits. It is at the subsequent stage—the combining of 2d-segments from orthogonal projections to form (three-dimensional) track segments—that the segmentation of the detector in some sense degrades the purity of reconstruction by introducing ambiguous (or *ghost*) track segments. Any given pair of 2d-segments from different projections may define a track segment, which is characterised by a trajectory in terms of direction cosines (or θ and ϕ) and a single point on a 'reference plane' defined at $|z| = 539.55$ cm. The difficulty arises in trying to determine which 2d-segments to combine, given that only a weak correlation exists in the pulse heights between hits from the different projections in the same quadrant. (As this correlation had not been observed when the ME processor was written, no use is made of this effect, although to do so would be a fairly straightforward procedure.)

---

[4] More precisely, this is a χ^2 upper tail distribution.

The default requirement imposed on combining 2d-segments is that there must be two or more xz and yz hits that have originated from the same streamer tube planes, with the further constraint that one pair of matched hits must be in an inner endcap and the other in an outer endcap. It is unwise to insist that 2d-segments have all hits in identical streamer tube planes as this prevents tracks being formed whenever a single hit is missed from either 2d-segment, as might conceivably occur due to an occasional hardware problem or survey imperfection. In contrast, allowing segments to be formed in the absence of constraints occasionally leads to an inordinately high segment multiplicity when additional hits (*e.g.* from sources such as beam halo, or delta rays) are present in the chambers.

The requirement that segments have two streamer tube planes in common at the hit level before they are combined has been found to be a reasonable compromise. However, extra hits close to a genuine track do cause large numbers of segments to be generated. Such hits are attributed to electromagnetic showers in the vicinity of muons, initiated by an accompanying delta ray or photon. The comparison with GOPAL presented later in this chapter shows that the frequency of multiple segments in the data is consistent with expectation. This reinforces the idea that the extra hits originate from secondary processes rather than from noise in the chambers as the latter is *not* simulated in GOPAL; electronic noise as such is very limited in the actual chambers.

In the rare instances when very large numbers of localised segments are produced, the ME ROPE processor enters a second processing pass in which more stringent requirements are used in creating segments. The conditions which initiate this second pass and the changes to the segment finding parameters used are described in Appendix B. This procedure enables the ME processor to cope with all but a few recorded events without imposing an arbitrary cut on the total number of segments. For example, in reconstructing a sample of 9057 GOPAL muon pair events that contained hits in ME, the second pass processing was only required 5 times; in 3 out of these 5 events the reprocessing succeeded in producing track segments.

3.3 Calibration and processing parameters

In order to be able to reconstruct track segments in the muon endcaps, there are two types of information that must be available to the ME processor at run time. These are generically referred to as 'calibration data' or 'constants' although the latter is a rather misleading name as they will in general change in value during a given processing run. The two categories into which this data fall are,

- **Survey** The positions and dimensions of the chambers in the OPAL co-ordinate system.

- **Processing parameters** The options and parameter values that define the rules governing segment reconstruction.

This data is distributed over five 'directories' in the calibration database, where each directory is arranged to have a one-to-one correspondence with a bank in the part of the constants structure reserved for the ME processor. (The motivation for segregating the data into different directories is that the database utility processor, OPCAL, is more efficient when data with differing update frequencies are stored in separate directories.) These banks themselves contain the following information:

MESF (ME Survey Frame) This is the survey information for the positions of the large, iron support frames of the muon endcaps in the OPAL co-ordinate system. These are stored as the Cartesian co-ordinates of a series of fiducial dowell pegs accurately positioned upon the frames. There are a total of 216 real data words (corresponding to 72 three-dimensional co-ordinates) that are stored which are updated whenever the muon endcaps are moved into or out of the beam position.

MESI (ME Survey Internal) This is the survey information for the internal structure of the quadrants, *i.e.* the relative positions of all of the dowell pegs. There are a total of 2448 real data words (which is equivalent to 816 measured points) stored: these are only updated when a quadrant is dismantled and subsequently rebuilt. The only forseen update of these parameters took place recently when the ideal, design specification for the internal dimensions was superceded by surveyed values.

MEGM (ME GeoMetry) This bank contains various geometric parameters intrinsic to the detector such as the readout strip widths and the gap between adjacent units. The data stored consists of 8 real words and will only be updated when more parameters are required by future program development.

MECN (ME CoNstants) The contents of this bank are the parameters that control the behaviour of the ME processor and include the road width, resolutions and control flags. It is updated whenever better tuned sets of parameters are obtained and comprises 20 real words.

MEDR (ME Dead Region) This consists of a list of integers which specify a series of readout strip numbers. Taken in pairs, these strips define intervals of readout strips which are considered inoperative or unreliable. Although this facility has been successfully tested, it was not used during the 1990 run.

This data can be obtained from several sources and there is a well defined hierarchy to determine which is used, depending upon the type of data that is being processed and the external input available in a given `ROPE` run. Calibrations may be read from the main calibration databases, sequential files and `FFREAD` cards amongst others, in various combinations. The mechanics of handling calibrations by the ME processor is quite technically involved and definitive details are given elsewhere [40].

3.3.1 Features of survey data

The position of a given readout strip is obtained by combining the known position of the quadrant in which it is located and the position of the strip within the given quadrant. For all processing to date, the positions of the quadrants have been calculated from detailed survey measurements made *in situ* in the experimental hall. The position of each quadrant is defined by a single survey point after much cross checking and validation, some of which is performed automatically by the ME processor. The precision of these points is typically ±1 mm.

The internal dimensions of the quadrants have hitherto been taken from the design specification although recent measurements and careful checking has allowed the actual internal dimensions of the chambers to be used. Studies in the overlap regions between quadrants and patches have proved to be useful in evaluating the validity of new survey measurements. It is estimated that the new calibrations will only affect the position of reconstructed hits at the level of a few mm in directions perpendicular to the beam axis.

3.4 Performance of the ME ROPE processor

In addition to reconstructing tracks segments, this software also provides basic monitoring data in the form of simple histograms which summarise the overall performance of the muon endcaps. These distributions, shown in figure 3.4, are:

- The distribution of hits amongst the quadrants and patches. Hits are recorded for each individual quadrant and patch in a plane and these are ordered according to their high voltage configuration, resulting in a characteristic 'comb-like' distribution because of the relative areas of patches and quadrants. Deviations in this distribution have indicated high voltage problems in the chambers.

- The hit multiplicity within 2d-segments, considering xz and yz projections separately. This shows the proportion of segments that are found with the expected number of hits, the mode being four hits for events which do not have excessive activity in the chambers. (In the presence of large backgrounds, more spurious segments are likely to be formed which will tend to have fewer hits than genuine segments.)

- The track segment multiplicity per event—the end product of the muon endcap detector and ME processor.

- The trajectories of track segments with respect to the beam axis, expressed as a direction cosine.

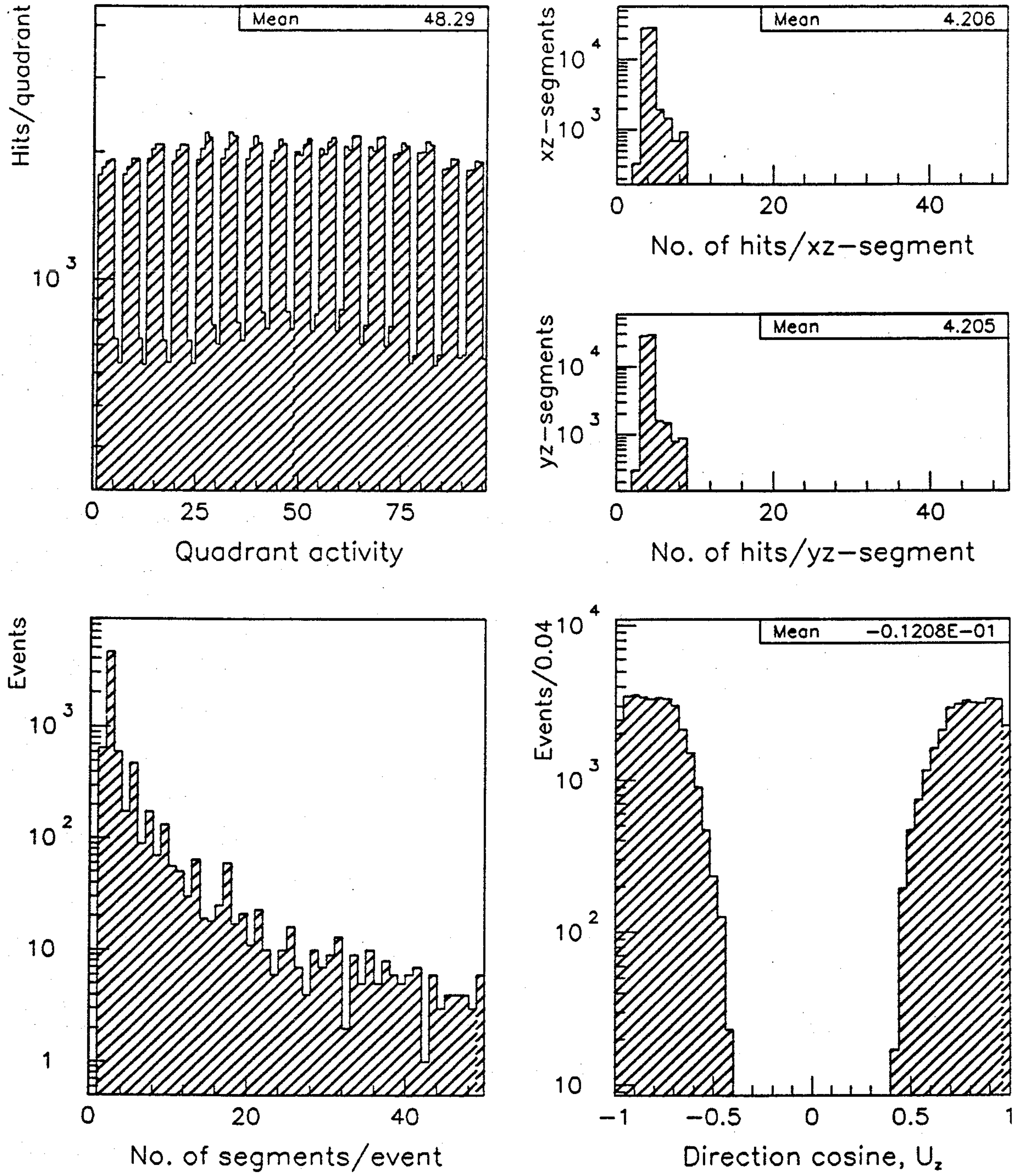

Figure 3.4: Standard histograms produced by the ME ROPE processor.

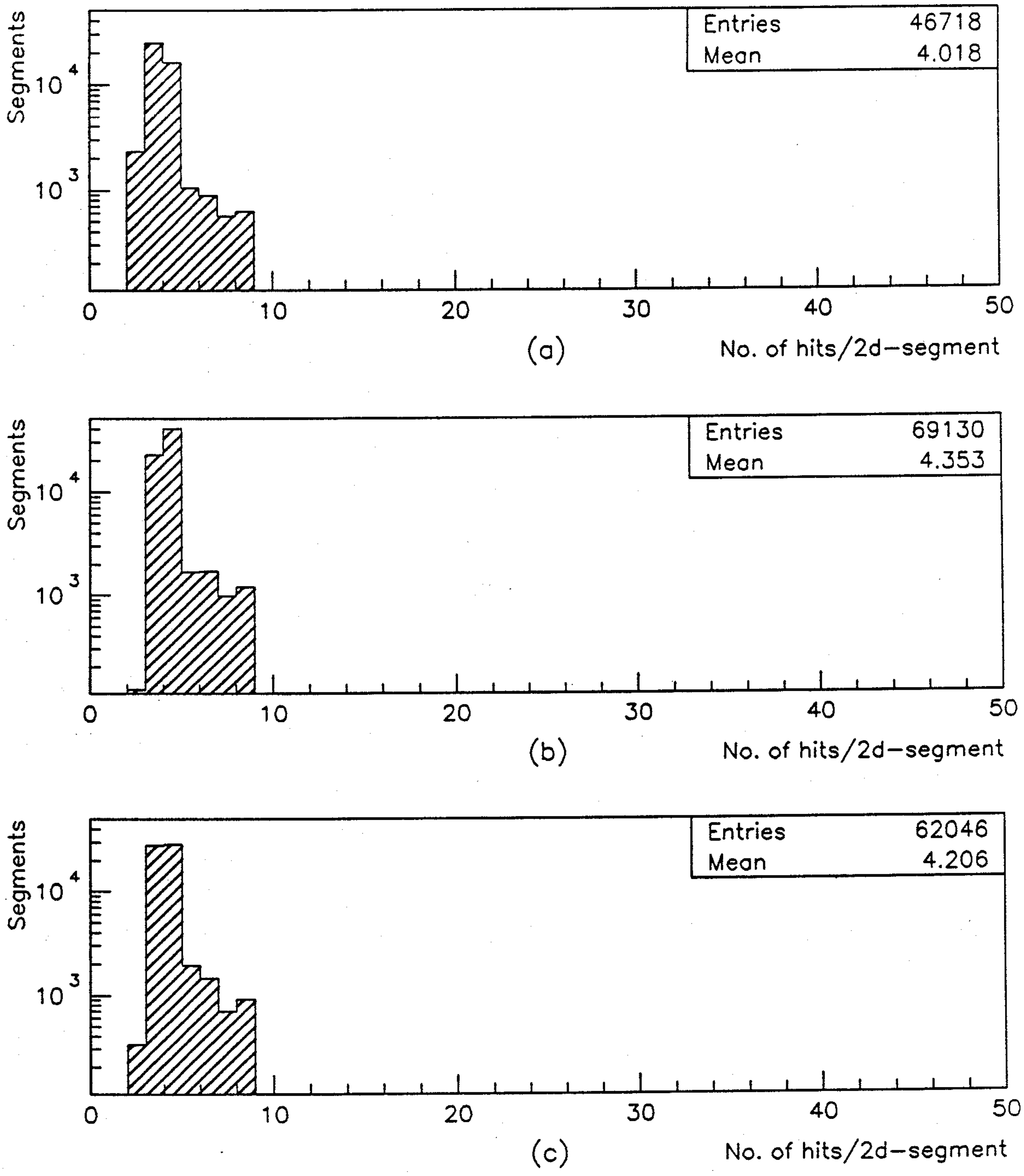

Key
(a) Road = 5 mm
(b) Road = 20 mm
(c) Road = 9 mm (default)

Figure 3.5: Hit multiplicity within segments, for three different roads (note logarithmic scale).

3.4.1 Dependence on road width

The accuracy and speed of reconstruction depend upon a number of parameters such as the basic road width and the minimum number of matched hits required to form a segment. These rules have been tuned by varying parameters using `FFREAD` data cards at program execution time [40, p 2]. An optimal set of such parameters is maintained in the calibration database in such a way that these rules may in general be changed from event to event; in practise, this parameter set has only been modified once since the first physics data recorded in 1989. To illustrate the sensitivity of the reconstruction to variations in these parameters, the qualitative dependence of the hit multiplicity in 2d-segments on the road width is discussed below. It should be noted that away from the edges of the quadrants, 2d-segments having four hits are expected to be more common than other hit multiplicities and so the fraction of all segments that are of this type, $\frac{N_4}{N_{\mathrm{Tot}}}$, should be a good indication of the quality of the reconstruction.

If too small a road is used (*e.g.* 5 mm, ~ chamber resolution) many 2d-segments that should have four hits are reconstructed as several 2d-segments, each with only two or three hits (see figure 3.5a). As two or more hits must be matched between projections to form a track segment and most 2d-segments only have three hits, the overall number of three-dimensional objects produced is *not* proportional to the product of the number of 2d-segments in either projection, as is approximately true under normal conditions. Having too small a road width tends to increase the total number of 2d-segments whilst reducing the number of 3d-segments.

Conversely, if too large a road is used (*e.g.* 20 mm) an abundance of high multiplicity 2d-segments will be reconstructed (see figure 3.5b). Having a higher number of hits, these have an increased probability of being combined with 2d-segments from orthogonal projections, as only two hits need to be associated in order to define a 3d-segment. Extra hits present a more serious problem when using a larger road, particularly in the overlap regions of the detector.

The compromise adopted is for the road to be a few times larger than the estimated detector resolution, *i.e.* 9 mm (see figure 3.5c). As explained above, the number of segments reconstructed *does* depend upon the precise value of the

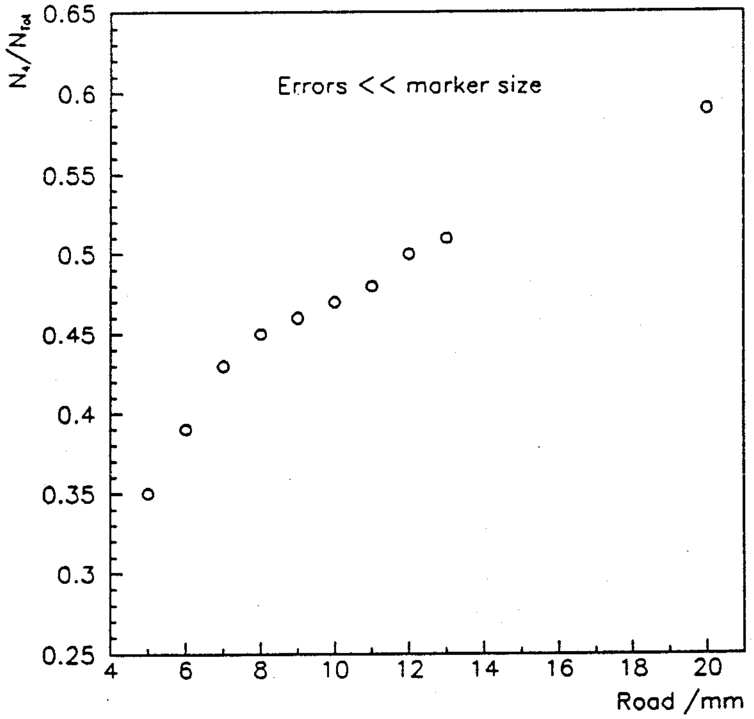

Figure 3.6: Variation in four hit 2d-segments with road.

road used. However, the variation in the quantity, $\frac{N_4}{N_{tot}}$, proposed above as an indicator of reconstruction quality, is relatively small over such a wide range in the road width as illustrated in figure 3.6. This optimisation was carried out making extensive use of Monte Carlo data and so-called 'cheat hits'—true hits from the simulated muon—against which the reconstructed tracks may be compared to optimise track finding efficiency. The overall efficiency for finding muons within the geometrical acceptance is high ($\gtrsim 98\%$) as only two hit out of a possible four hits are necessary to make a segment.

3.5 Comparison of `GOPAL` and real data

The muon endcaps are modelled in detail within `GOPAL` with each of the 21248 streamer tubes being simulated. In order to use this simulation for physics analysis, reconstructed Monte Carlo events must resemble reconstructed OPAL events. Distributions of four quantities that are representative of the reconstruction process are compared below, using dimuon events for simplicity. The datasets used are a sample of 20000 `GOPAL` muon pair events and an OPAL standard event sample

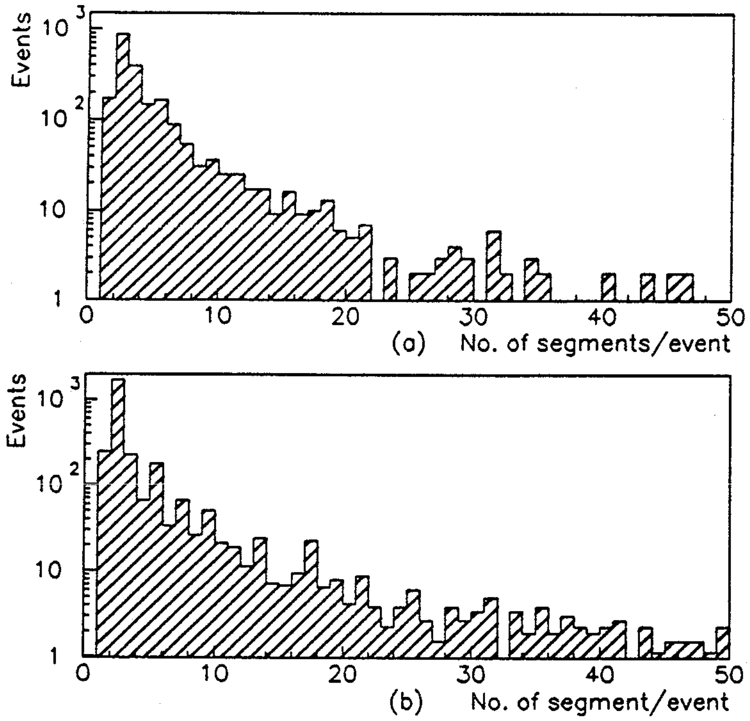

Key
(a) Real data (b) Monte Carlo

Figure 3.7: Comparison of total number of segments reconstructed/event

of 6033 muon pair events recorded in 1990. In order to allow a 'clean' comparison to be made, a simple cut is made to ensure only relatively high quality muon segments are used.

The cut imposed on the data samples is that there must be exactly two three-dimensional muon endcap segments. In the first quantity presented, the number of segments reconstructed per event, this cut is inappropriate and is not applied. For presentation purposes all Monte Carlo data below has been normalised to the appropriate quantity of real data, such as the total number of segments or events.

The total number of track segments reconstructed per event

The number of reconstructed three-dimensional track segments is shown in figure 3.7 (with logarithmic scales) for real and Monte Carlo data. The agreement here is very good, even in the tail region where higher number of segments are produced. The number of Monte Carlo and real events in which more than 50 segments were reconstructed are also mutually consistent. Slightly more events

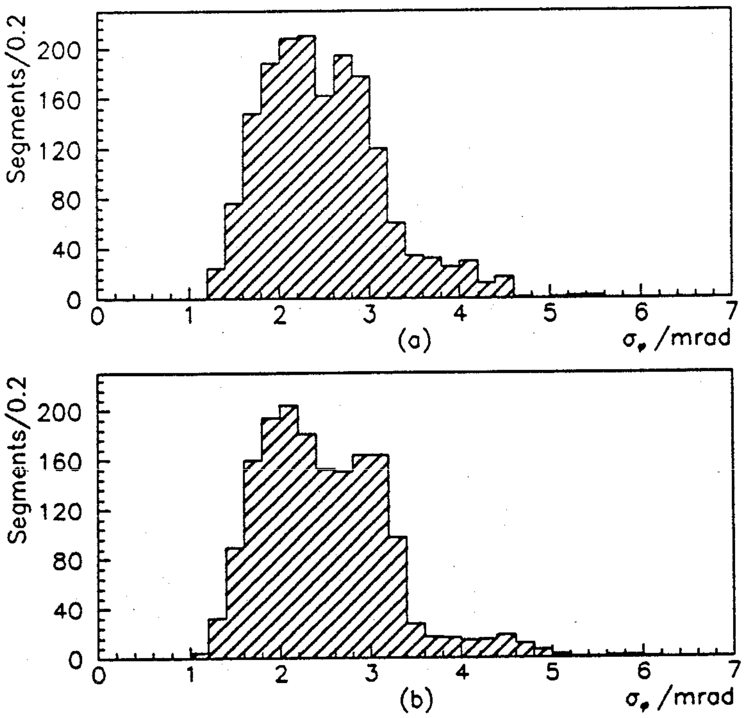

Key
(a) Real data (b) Monte Carlo

Figure 3.8: Comparison of error on reconstructed polar angle, σ_θ

containing three segments are reconstructed in the real data set. This is attributed to small imperfections in the knowledge of the chamber positions from the survey which cannot be modelled in the Monte Carlo. This effect is most pronounced in the overlap regions between upper and lower quadrants and also between patches and quadrants (in total about 6% of the detector area at normal incidence) where it is possible to have eight hits on a 2d-segment.

The error on the reconstructed polar angle, σ_θ

The error on the reconstructed trajectory of three-dimensional segments with respect to the z axis, σ_θ, is shown in figure 3.8 for real and Monte Carlo data. These two profiles closely resemble one another. In using this error to form associations between muon endcap segments and those from other sub-detectors, it is necessary to include a term to allow for systematic uncertainties in their relative positions. The extra contribution is similar in magnitude to σ_θ itself.

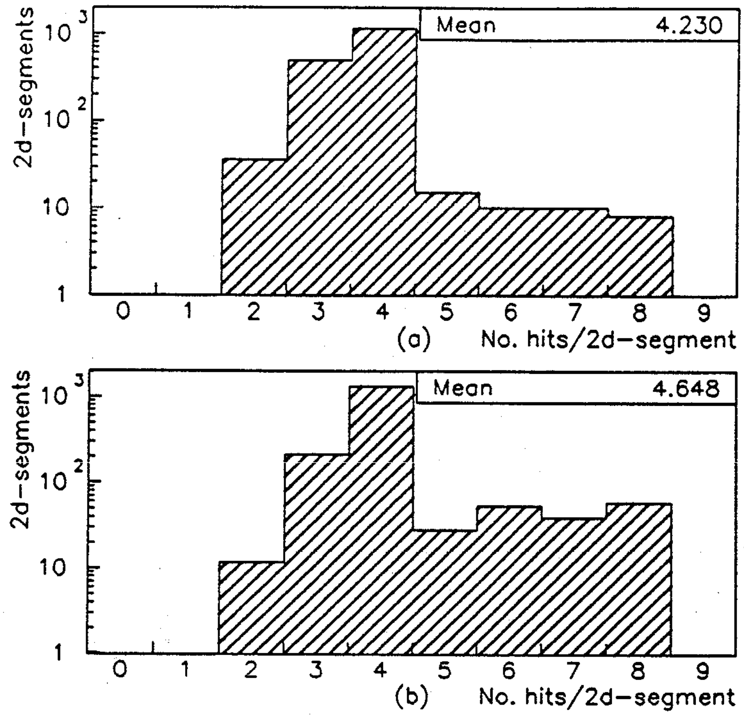

Key
(a) Real data (b) Monte Carlo

Figure 3.9: Comparison of hit multiplicity in 2d-segments

The hit multiplicity in 2d-segments

The hit multiplicity in 2d-segments is shown in figure 3.9 (with logarithmic scales) for real and Monte Carlo data. There is an excess of 2d-segments with more that four hits in the Monte Carlo data. This is an artefact of imperfections in the survey of the detector: in the overlap regions where more than four hits are possible, systematic shifts between quadrants cause 2d-segments to be split resulting in lower proportion of 2d-segments with more than four hits in real data than in the Monte Carlo.

A rough estimate of the overall hit finding efficiency of each plane (*i.e.* the combined efficiency of the streamer tube planes and the hit finding algorithm) can be obtained from the ratio of the number of three hit 2d-segments to the number of four hit 2d-segments, $\frac{N_3}{N_4}$, assuming that three hit 2d-segments would have been reconstructed with four hits but for an inefficiency in one of four streamer tube planes. It is assumed that any inefficiency in the 2d-segment finding algorithm is negligible. Defining the efficiency for finding a hit in a given streamer tube plane as ϵ, the probability of obtaining a 2d-segment with four hits is ϵ^4. To obtain a three hit segment, any one out of the four possible planes must not have a hit (probability $(1-\epsilon)$) whilst the other three do have hits (probability ϵ^3). As this can occur in four different combinations the probability of obtaining a three hit 2d-segment is $4\epsilon^3(1-\epsilon)$.

The quantity $\frac{N_3}{N_4}$ is given by the ratio of the probabilities for obtaining three hits and four hits on a 2d-segment; it follows that the efficiency per plane is given by,

$$\epsilon = \left(1 + \frac{1}{4}\frac{N_3}{N_4}\right)^{-1}.$$

Using the expression above, the efficiency per plane is estimated to be,

$$\begin{aligned} \epsilon_{\mathtt{GOPAL}} &= 96.2 \pm 0.1\% \\ \epsilon_{\mathtt{OPAL}} &= 90.4 \pm 1.3\%. \end{aligned}$$

As the segment finding efficiency is approximately given by $(1-(1-\epsilon)^2)$, the discrepancy between these efficiencies leads to a difference in the segment finding efficiency between Monte Carlo and real data of less than 1%. The inconsistency in these efficiencies is not sufficiently large to cause any problem in using the simulation because of the large redundancy in the ME system. This result is consistent with other studies [41]. A parameter of the streamer tube simulation, the minimum path length that a muon must traverse within the active volume of a streamer tube before a hit is produced, can be tuned to resolve this disagreement.

The χ^2 per degree of freedom for 2d-segments

The χ^2 per degree of freedom distributions are shown in figure 3.10 for real and Monte Carlo data. This χ^2 is calculated from the straight line fit for 2d-segments assuming resolutions of 2 mm for the high resolution readout planes and 3 mm for the low resolution planes. The data presented in the figure includes 2d-segments with between three and eight hits and is therefore proportional to the sum of six different χ^2 probability density distributions $P(\chi^2, n)$, each divided by the appropriate number of degrees of freedom, n.

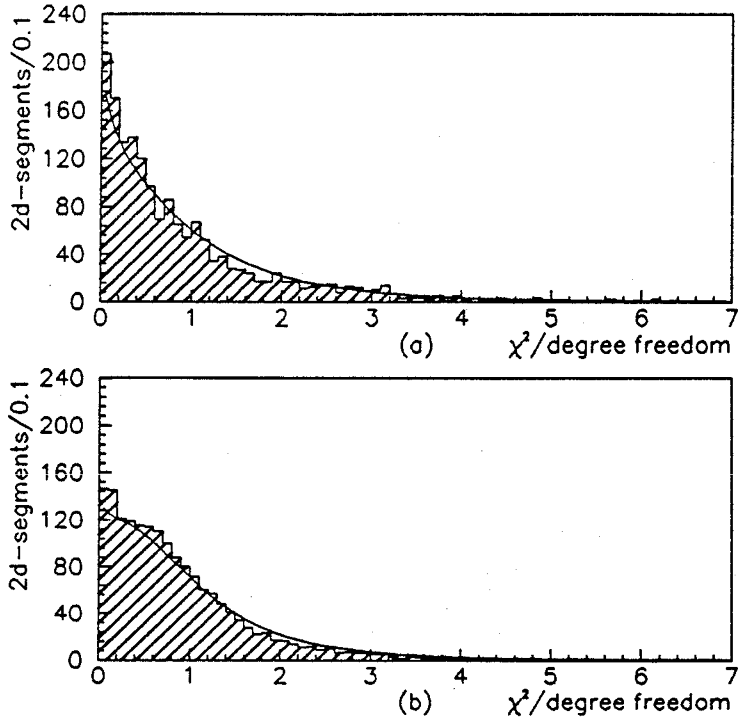

Key
(a) Real data (b) Monte Carlo Solid curve: ideal χ^2 (see text)

Figure 3.10: Comparison of χ^2/degree of freedom for 2d-segments

By calculating these six different distributions from the definition,

$$P(z,n) \equiv \frac{z^{\frac{n}{2}-1}e^{-\frac{z}{2}}}{\sqrt{2^n}\Gamma(\frac{n}{2})}, \quad \text{with } z \equiv \chi^2 \geq 0,$$

adding them together according to the relative numbers of 2d-segments of each type present (which is obtained from figure 3.9) it is possible to find an 'ideal' χ^2/n distribution for both real data and Monte Carlo. These ideal predictions for the observed hit multiplicities. normalised to corresponding real or Monte Carlo distribution, are included in the figure as solid curves. It can be seen that the ideal curves agree well with the χ^2/n obtained from the segment reconstruction in both real and simulated cases. In the actual experiment, the χ^2/n has been used as an indicator of systematic shifts in the survey measurements between quadrants by using segments reconstructed in the overlap regions.

3.5.1 Conclusions

The agreement above is illustrative of the compatibility between the very detailed simulation and data recorded with the OPAL detector. These comparisons are typical of those performed for each sub-detector in OPAL. Thus, `GOPAL` may be used in analysis for various tasks such as estimation of the efficiency of event selection criteria or the correction of data for detector effects *e.g.* acceptance. It is used extensively in the analysis presented later in this thesis.

Chapter 4

Theoretical description of $e^+e^- \rightarrow \mu^+\mu^-$

A high precision measurement of parameters present in the standard model, such as the width or couplings of the Z^0 boson, may be used to strictly test the model by comparing the predicted values with those determined experimentally. Such parameters may be extracted by the analysis of final states produced at LEP energies; only the muon pair final state is studied herein. Muon pairs are very attractive theoretically as they are only produced via s-channel exchange processes at tree level, unlike e^+e^- production which has a large contribution from t-channel processes, and there are no complications associated with particle decays, as is the case for $\tau^+\tau^-$ or $q\overline{q}$ production. Furthermore, muon pairs are a desirable state to study from an experimental point of view because their detection and reconstruction is comparatively straightforward and they have a relatively small background. They have been the subject of many studies in the past [14,16] to which the reader is referred for details.

This chapter outlines briefly the process of $\mu^+\mu^-$ production[1] near the Z^0 pole and the theoretical description of two important quantities which are experimentally accessible, *viz.* the forward-backward asymmetry ($A_{\mathrm{FB}}(s)$) and the cross section ($\sigma(s)$). The choice of input parameters for calculations within the standard model is discussed, as is the effect of higher order diagrams which modify $A_{\mathrm{FB}}(s)$ and $\sigma(s)$ from their tree level values. The amount by which the various classes of higher order diagrams modify $A_{\mathrm{FB}}(s)$ and $\sigma(s)$ is illustrated by a numerical

---

[1] Most results are applicable to a general $f\overline{f}$, $f \neq e$ final state in which fermion masses may be neglected.

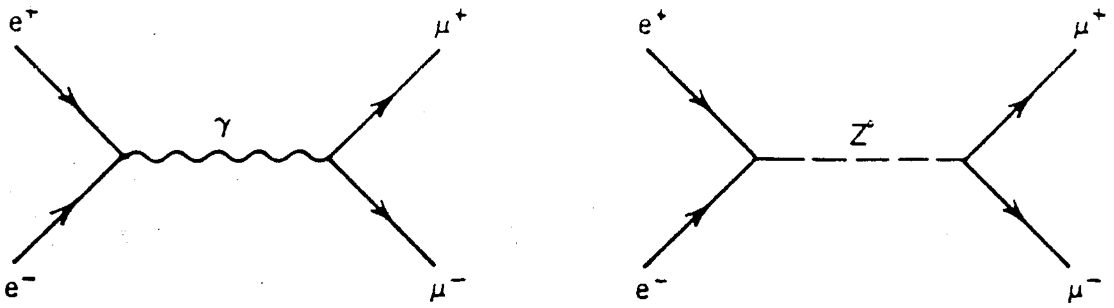

(a) virtual γ exchange (b) Z^0 exchange

Figure 4.1: Feynman diagrams for $e^+e^- \rightarrow \mu^+\mu^-$ in lowest order

comparison.

4.1 Lowest order (Born) processes

There are two processes with amplitudes of order α that contribute to $\mu^+\mu^-$ production in e^+e^- annihilation, the Higgs exchange process being completely negligible. These are the virtual photon and Z^0 exchange diagrams, illustrated in figures 4.1a and 4.1b respectively.

The vertex factors that determine the coupling strength of fermions to gauge bosons in neutral current (NC) interactions can be expressed in terms of the charge on the electron, e, and the weak mixing angle, θ_W. The vertex factor for the electromagnetic interaction ($f\bar{f}\gamma$) is given by,

$$-ieQ_f\gamma_\mu,$$

whilst that for the weak neutral current interaction ($f\bar{f}Z^0$) is given by,

$$i\frac{e}{2\sin\theta_W\cos\theta_W}\gamma_\mu(v_f - a_f\gamma_5),$$

where γ_μ and γ_5 are Dirac gamma matrices, and v_f, a_f and Q_f respectively denote the vector coupling constant, axial vector coupling constant and the charge of a given fermion species f. The couplings v_f and a_f may be parameterised[2] as,

$$v_f = I_3^f - 2Q_f \sin^2\theta_W, \qquad a_f = I_3^f,$$

where I_3^f is the third component of weak isospin for a given fermion species. In the standard model, each species of lepton should experience the same coupling to the photon or Z^0 as all lepton generations possess the same doublet structure and hence isospin and charge assignments. This lepton universality can be tested by a direct measurement of the couplings for different species at LEP.

4.1.1 Choice of standard model parameters

There are seventeen free parameters in the minimal standard model, the values of which have to be determined by experimental measurements. These are the quark and charged lepton masses, three quark mixing angles, the mass of the Higgs scalar, the vev of the Higgs field and three gauge couplings (one from the strong and two from the electroweak sector). A meaningful test of the standard model requires that as many of these parameters must be measured experimentally as possible. For electroweak tests, the vev of the Higgs field and the SU(2) and U(1) gauge coupling constants have to be independently fixed by experiment although the actual input is via observable quantities such as M_W or M_Z[3]. The masses of the top quark (M_t) and Higgs scalar (M_H) remain as free parameters in calculations as their values have not been determined to date.

For experiments at LEP, a good (*i.e.* well measured) set of input parameters to use is the Fermi constant G_F, the fine structure constant α and the Z^0 boson mass, M_Z. By comparing the lowest order standard model expression for the muon lifetime with the Fermi model expression for the same, one can identify,

$$G_F = \frac{\alpha\pi}{\sqrt{2}} \frac{1}{{M_W}^2 \sin^2\theta_W}. \tag{4.1}$$

---

[2] Various conventions are used in defining these couplings, *e.g.* v_f and a_f are larger by a factor of 2 in [20].

[3] In order for M_Z to be a valid input, it must be independent of the other standard model parameters; this is illustrated in the literature [16, pp 89–128].

Using the on-shell renormalisation scheme [42], the weak mixing angle is defined by

$$\sin^2\theta_W \equiv 1 - \frac{M_W{}^2}{M_Z{}^2}. \tag{4.2}$$

Thus, with essentially negligible experimental errors on G_F and α, an accurate measurement of M_Z effectively fixes the numerical values of $\sin^2\theta_W$ and M_W. Using the relations given in equations 4.1 and 4.2, it follows that,

$$\begin{aligned} M_W{}^2 &= \frac{M_Z^2}{2}\left(1+\sqrt{1-\frac{4A}{M_Z{}^2}}\right), \\ \sin^2\theta_W &= \frac{1}{2}\left(1-\sqrt{1-\frac{4A}{M_Z{}^2}}\right), \end{aligned}$$

where

$$A = \frac{\pi\alpha}{\sqrt{2}\,G_F}. \tag{4.3}$$

4.2 Radiative corrections

In studying $e^+e^- \to \mu^+\mu^-$ near the Z^0 pole it is insufficient to only consider the lowest order processes of figure 4.1, as loop diagrams (contributing to the elastic process) and real photon bremsstrahlung emission (contributing to the inclusive inelastic process) are of numerical significance. At the level of one-loop corrections to the basic process, these diagrams can be divided into 'weak' and 'photonic' (or 'QED') corrections. Beyond the one-loop level, this simple categorisation cannot be made. The two classes, which are expanded upon in the following sections, are defined thus:

- **Photonic corrections** This set consists of all diagrams with a single extra real bremsstrahlung photon or virtual photon loop added to the Born diagrams (see figure 4.2).

- **Weak corrections** This set is composed of all remaining one-loop diagrams (see figure 4.3). These include vertex corrections with virtual gauge bosons, propagator corrections (vacuum polarisation and Z^0 self-energy diagrams) and box diagrams with the exchange of two massive gauge bosons.

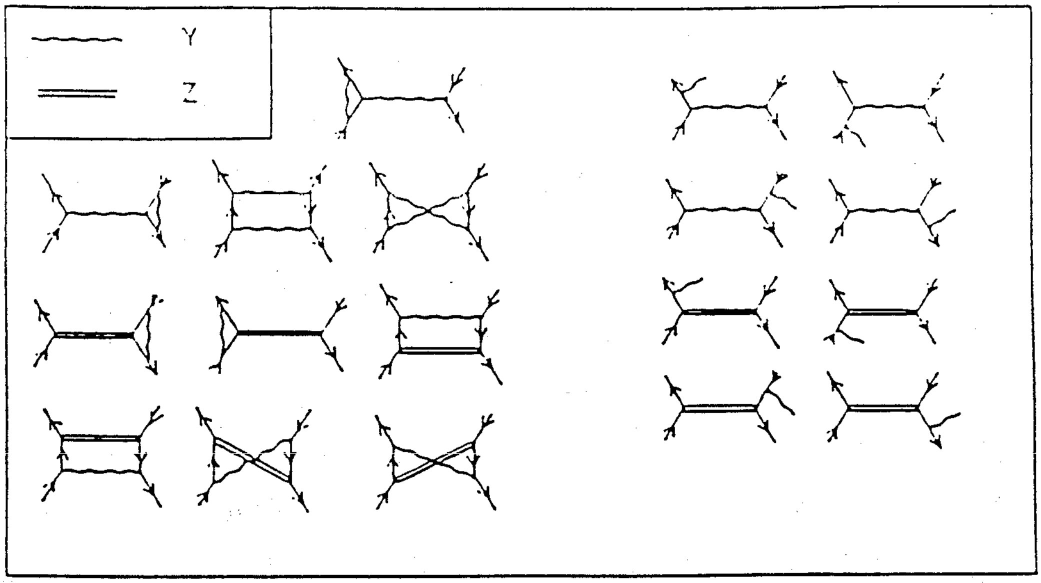

Figure 4.2: One-loop photonic corrections to $e^+e^- \rightarrow \mu^+\mu^-$ (from [16]).

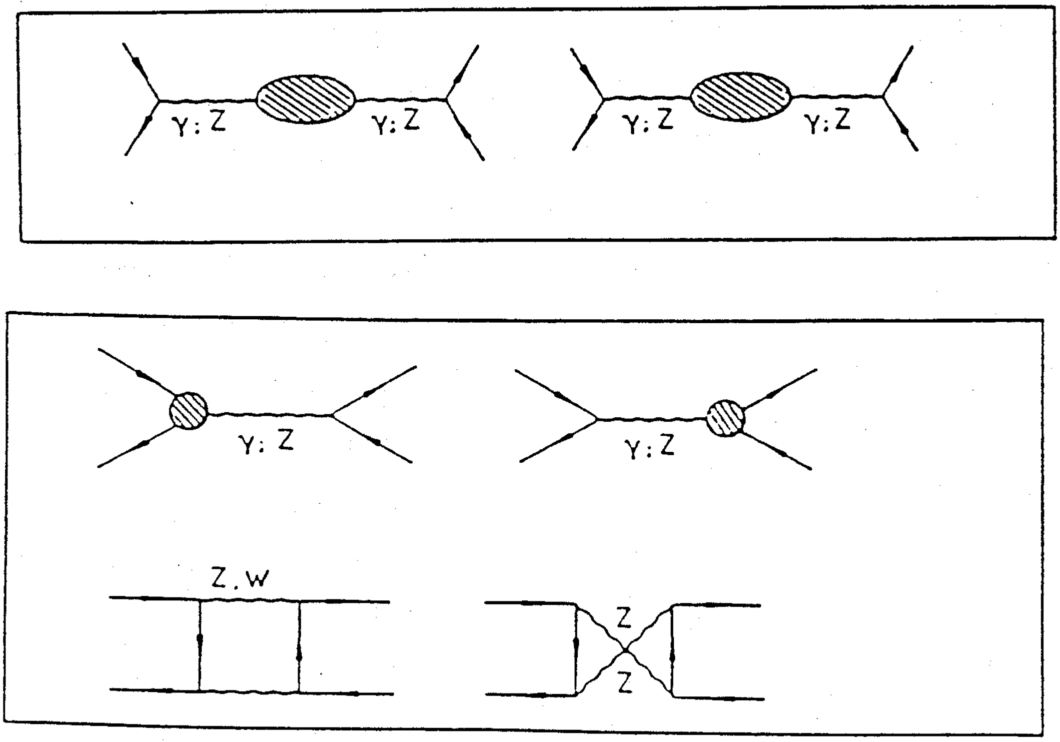

Figure 4.3: One-loop weak corrections to $e^+e^- \rightarrow \mu^+\mu^-$ (from [16]).

Currently, complete two-loop calculations of purely photonic corrections have been performed, whilst weak corrections have been calculated complete in one-loop level with leading terms from two-loops. (A *complete* calculation is defined as one that retains all terms of a given order that are non-vanishing in the limit of m_f^2/s tending to zero.) Cross sections or asymmetries incorporating these corrections are normally evaluated by Monte Carlo methods or by *semi-analytic* calculations. where a semi-analytic procedure is an analytic computation in which some integrals are performed numerically. It should be noted that the former allow exclusive quantities to be calculated in the presence of complex cuts on the phase space of all the particles present in a given process. whereas the latter are restricted to the evaluation of inclusive quantities subject to limited cuts. However, there is always a statistical error associated with any Monte Carlo result which semi-analytic procedures do not suffer from.

4.2.1 Photonic corrections

The most significant subset of diagrams are those including radiation of real photons from the initial state fermions, which reduce the peak cross section by approximately 40%. In an e^+e^- initial state with centre of mass energy $\sqrt{s}$, the radiation of photons reduces the energy available for Z^0 production to $\sqrt{s'}$. The cross section that is actually observed for an initial state characterised by s is the Z^0 production cross section at s'. For s corresponding to the peak cross section, $\sigma(s) > \sigma(s')$ by definition, hence the observed cross section is reduced by photonic corrections. The effect is large due to the very rapid variation in cross section in the vicinity of the the Z^0.

These corrections are independent of the non-electromagnetic details of the theory (such as structure of the Higgs sector), require only the global parameters of the model in order to be evaluated, are gauge invariant and their effect is influenced by the details of the experiment and cuts imposed. Cross sections and asymmetries may be corrected for photonic effects by convolution with a photon distribution function or 'radiator'[4], as described in Appendix C.

---

[4] A radiator, $G(s/s')$, is a function that represents the probability that the centre of mass energy, $\sqrt{s}$ is reduced to $\sqrt{s'}$ by initial state radiation.

There are severe practical problems that have to be overcome in calculating cross sections with photonic radiative corrections. So-called *infrared* divergences are present in the virtual photon and soft[5] real bremsstrahlung cross sections. arising from the presence of photons that. in the limiting case, have zero energy and zero mass. These divergences may be formally regulated by the introduction of an artificial. finite photon mass (M_γ). The subsequent combination of the two cross sections forms a 'soft photon' cross section. which includes all photons that are not detectable. in which the M_γ dependence vanishes—the phenomena of 'infrared cancellation'.

Despite the cancellation of M_γ. an arbitrary distinction between soft and hard bremsstrahlung exists at E_0. This E_0 should be sufficiently small that no three-body behaviour is observable in the soft photonic final state, whilst being sufficiently large to ensure that all the cross sections remain positive. (If E_0 is set to zero, the original divergences are recovered.) This conflict is problematic for Monte Carlo techniques. in which all cross sections must remain positive definite so that they may be interpreted as probabilities: in contrast, it presents no trouble to semi-analytic calculations in which only the final cross section is constrained to be positive. The dilemma occurs in all cross sections that contain an odd number of soft bremsstrahlung or virtual photons and cannot be resolved by incorporating terms up to a finite higher order.

It has been shown [43] that this problem can be solved by considering soft photon contributions up to infinite order. This technique is known as *exponentiation* and is extensively used in the most complete calculations to date (*e.g.* [44,45]).

4.2.2 Weak corrections

These corrections are dependent on the detailed structure of the theory including the masses of the top quark and Higgs scalar and the renormalisation scheme used but are independent of the experimental cuts imposed. Cross sections and asymmetries may be corrected for weak effects by the use of 'effective' parameters such as couplings. This allows one to retain the lowest order form of the amplitude

---

[5] Soft bremsstrahlung photons are those with energies below some arbitrary cutoff, say E_0, that is sufficiently small that such photons are not detectable.

for the process by modifying parameter definitions appropriately. An amplitude modified in this way is referred to as 'Born-like'. The $O(\alpha)$ weak corrections can be divided into the categories of propagator corrections (2-point functions), vertex corrections (3-point functions) and box corrections (4-point functions) as shown in figure 4.3.

Propagator corrections comprise a universal contribution to the amplitude, *i.e.* they are independent of the external fermions in the process, arising from the insertion of self-energy loops in the propagators. For light fermions such as muons where vertex and box diagrams containing the Higgs scalar and top quark are vanishingly small, these corrections are the only place at which the unknown masses M_t and M_H may enter. The effect of including the self-energy insertions to the photon propagator may be incorporated in the definition of a 'running' charge, $e(s)$, or electromagnetic coupling, $\alpha(s)$. Similarly, the self-energy contributions from pure Z^0 exchange may be closely described near the resonance by the introduction of an s dependence to Γ_Z.

There is also γ-Z^0 mixing beyond tree level, in which a neutral gauge boson may leave a fermion line as a Z^0 and arrive at another one as a photon or *vice versa*, the change occurring via self-energy loops. This mixing may be treated as the existence of a new, combined γ-Z^0 propagator or (more commonly) as a change in the NC couplings of the Z^0. The required change in the couplings can be made by the introduction of a new mixing angle, $\sin^2\overline{\theta}_W$. It should be noted that in order to define this angle as a real quantity, imaginary terms from the self-energy diagrams must be omitted. As the imaginary part of $\sin^2\overline{\theta}_W \approx -0.01$ on resonance and the real part ≈ 0.23 for $M_Z = 92$ GeV, this is not a large effect [16, p 25]. Furthermore, the self-energies from bosonic loops do not form a gauge invariant set of diagrams and so cannot be included if $\sin^2\overline{\theta}_W$ is to be an observable quantity. Despite the seeming complexity, propagator corrections in the region of the Z^0 may be accounted for to a good approximation by introducing a simple energy dependence to the width of the Z^0(see section 4.3.2).

Vertex corrections are non-universal in nature as the possible virtual states depend upon the external fermion species. The corrections to the $f\overline{f}Z^0$ vertex may be accommodated in a Born-like amplitude if s-dependent form factors are used in the definition of the NC couplings [16, p 29]. Corrections to the $f\bar{f}\gamma$ vertex may be merged with other vertex and propagator corrections near the Z^0 resonance, despite not being Born-like, as they are non-resonating (*i.e.* do not become large at $s \sim M_Z^2$). If vertex corrections are combined with propagator corrections, the effective weak mixing angle must in general differ for each fermion species in order to account for the non-universal behaviour. Vertex corrections affect quantities such as the resonance cross section at the level of 1%.

Box corrections are neither universal nor Born-like in nature and have a complicated form which includes angular dependent terms through the Mandelstam variable s, t and u [16, p 33]. As these terms are non-resonant, they may be combined with both vertex and propagator corrections to give weakly 'dressed' amplitudes with a Born-like structure near resonance, where the couplings are physical observables. Near resonance, box contributions are negligible *e.g.* the on-resonance differential cross section is affected at the level of 0.02%.

The specific effects of radiative corrections on $A_{\mathrm{FB}}(s)$ and $\sigma(s)$ are illustrated in the following sections after the lowest order expressions have been presented.

4.3 Forward-Backward asymmetry

The Z^0 and γ exchange diagrams contributing to muon pair production have identical initial and final states and so the amplitude for the combined process is the coherent sum of these diagrams. The resulting interference manifests itself as an asymmetric angular distribution which is characterised by θ, defined as the angle between the incident e^+ and the outgoing μ^+. This forward-backward asymmetry is formally defined as

$$A_{\mathrm{FB}} \equiv \frac{\sigma_{\mathrm{F}} - \sigma_{\mathrm{B}}}{\sigma_{\mathrm{F}} + \sigma_{\mathrm{B}}}, \tag{4.4}$$

where,

$$\sigma_{\mathrm{F}} = 2\pi \int_0^{+1} d(\cos\theta)\,\frac{d\sigma}{d\Omega}, \quad \sigma_{\mathrm{B}} = 2\pi \int_{-1}^{0} d(\cos\theta)\,\frac{d\sigma}{d\Omega}. \tag{4.5}$$

Measurements of the asymmetry can be used to extract functions of the vector and axial vector couplings of fermions to the Z^0. These functions appear as coefficients in the differential cross section and are given below.

4.3.1 Lowest order expressions

The Born approximation to the differential cross section for muon pairs (after [16, p 205], [20]), which is symmetric about the initial state e^+e^- axis, may be written in the form:

$$\begin{aligned}\frac{d\sigma^0}{d\Omega} &= \frac{\alpha^2}{2s}\Big\{\Big[(1+\cos^2\theta)C^{(1)}_{\mathrm{ZZ}}+\cos\theta C^{(2)}_{\mathrm{ZZ}}\Big]\,|\chi_0(s)|^2+(1+\cos^2\theta)C_{\gamma\gamma}\\ &\quad + \Big[(1+\cos^2\theta)C^{(1)}_{\gamma\mathrm{Z}}+\cos\theta C^{(2)}_{\gamma\mathrm{Z}}\Big]\,\Re\{\chi_0(s)\}\Big\},\end{aligned} \tag{4.6}$$

where terms in m_μ^2/s, which are $\sim 10^{-6}$, have been neglected. $\Re(\chi)$ is used to denote the real part of χ. The remaining coefficients are given,

$$C^{(1)}_{\gamma\mathrm{Z}} = 2Q_eQ_\mu v_e v_\mu, \qquad C^{(2)}_{\gamma\mathrm{Z}} = 4Q_eQ_\mu a_e a_\mu, \qquad C_{\gamma\gamma} = {Q_e}^2{Q_\mu}^2,$$
$$C^{(1)}_{\mathrm{ZZ}} = ({v_e}^2+{a_e}^2)({v_\mu}^2+{a_\mu}^2), \qquad C^{(2)}_{\mathrm{ZZ}} = 8v_e v_\mu a_e a_\mu,$$

and $\chi_0(s)$ is the resonating function which is defined as

$$\chi_0(s) = \frac{G_{\mathrm{F}}{M_{\mathrm{Z}}}^2}{2\sqrt{2}\,\pi\alpha}\,\frac{s}{s-{M_{\mathrm{Z}}}^2+iM_{\mathrm{Z}}\Gamma_{\mathrm{Z}}}. \tag{4.7}$$

In equation 4.6, the terms in $C^{(1,2)}_{\mathrm{ZZ}}$, $C_{\gamma\gamma}$ and $C^{(1,2)}_{\gamma\mathrm{Z}}$ are associated with pure Z^0 exchange, pure γ exchange and γ-Z^0 interference respectively. All coefficients are simple functions of the charges and the vector and axial vector couplings of the fermions.

Given this form for $\frac{d\sigma^0}{d\Omega}$, it follows from equations 4.4 and 4.5 that the lowest order asymmetry is given:

$$A^0_{\mathrm{FB}}(s) = \frac{3}{8}\,\frac{\Big[\Re\{\chi_0(s)\}C^{(2)}_{\gamma\mathrm{Z}}+|\chi_0(s)|^2C^{(2)}_{\mathrm{ZZ}}\Big]}{\Big[\Re\{\chi_0(s)\}C^{(1)}_{\gamma\mathrm{Z}}+|\chi_0(s)|^2C^{(1)}_{\mathrm{ZZ}}+\frac{1}{2}C_{\gamma\gamma}\Big]}. \tag{4.8}$$

In detail this approximation is inadequate in the region of the Z^0, given the experimental precision attainable. It is necessary to consider not only the large, lineshape distorting photonic corrections but also effects arising from weak corrections to propagators and vertices.

4.3.2 Higher order expressions

The photonic corrections to $A_{FB}(s)$ can be incorporated by convolution with a radiator, analogous to the procedure for cross sections given in Appendix C. The convolution may be performed numerically to facilitate cuts on exclusive quantities such as acolinearity (*e.g.* as in the program `ZFITTER` [46]). The main effects of the $O(\alpha)$ weak corrections, which are numerically small compared to the photonic corrections, originate from propagator corrections and can be incorporated into a differential cross section with a Born-like structure by redefining the following parameters using the substitutions:

$$\begin{array}{rcll}
\Gamma_Z & \rightarrow & \Gamma_Z(s) \;= \frac{s\Gamma_Z}{M_Z^2} & \text{from } Z^0 \text{ propagator corrections} \\
\alpha & \rightarrow & \alpha(M_Z{}^2) \;= \frac{\alpha}{1-\Delta\alpha} & \text{from } \gamma \text{ propagator corrections} \\
\sin^2\theta_W & \rightarrow & \sin^2\overline{\theta}_W & \\
a_f & \rightarrow & \hat{a}_f \;\equiv \sqrt{\rho}a_f & \left\{\begin{array}{l}\text{from } \gamma\text{-}Z^0 \text{ propagator} \\ \text{mixing corrections and} \\ \text{vertex corrections}\end{array}\right. \\
v_f & \rightarrow & \hat{v}_f \;\equiv \sqrt{\rho}v_f &
\end{array} \tag{4.9}$$

where the photon vacuum polarisation contribution at $s = M_Z^2$, (M_Z in GeV) is given [16, p 45]

$$\Delta\alpha \cong 0.0602 + \frac{40}{9}.\frac{\alpha}{\pi}\log\frac{M_Z}{92.} \pm 0.0009$$

and where the Z amplitude is normalised by ρ (appearing in the effective couplings, $\hat{a}_f$ and $\hat{v}_f$) which is given,

$$\rho \cong \frac{1}{1-\Delta\rho}, \qquad \text{with} \quad \Delta\rho = \frac{3G_F M_t^2}{8\sqrt{2}\pi^2}. \tag{4.10}$$

In the standard model, the effective mixing angle is related to ρ by,

$$\sin^2\overline{\theta}_W \cong \frac{1}{2}\left(1 - \sqrt{1 - \frac{4A}{\rho M_Z^2(1-\Delta\alpha)}}\right) \tag{4.11}$$

with A as defined in equation 4.3. Furthermore, the standard model relation between $\Delta\alpha$ and ρ is,

$$\frac{A}{1-\Delta\alpha} = \rho M_Z^2 \sin^2\overline{\theta}_W \cos^2\overline{\theta}_W. \tag{4.12}$$

This is the essence of the so-called improved Born approximation [16,47]. There are many variants on this parameterisation in use and various levels of corrections that may be 'absorbed' into the effective parameters, with corresponding degrees of model dependence. These are discussed in the final chapter of this thesis in connection with fitting the parameters of equation 4.9 to measured asymmetries and cross sections. Although the improved Born approximation does not include the imaginary parts of self-energies, nor a proper treatment of the vertex and box corrections, for muons at resonance these contributions accidentally cancel. (This is not the case for other final states.)

A useful feature of the improved Born approximation is that qualitative features of the lowest order expressions are still applicable. This allows a simple interpretation of the non-photonic behaviour near the resonance, *e.g.* from equation 4.8, the asymmetry on-resonance is determined predominately by the ratio $\frac{C^{(2)}_{\rm ZZ}}{C^{(1)}_{\rm ZZ}}$ and its energy evolution is determined by the ratio $\frac{\Re\{\chi_0(s)\}C^{(2)}_{\gamma \rm Z}}{C^{(1)}_{\rm ZZ}|\chi_0(s)|^2}$.

4.4 Line shape

Measurements of the cross section for different decay channels of the Z^0 allow measurements of the mass and partial and total widths of the Z^0. As with determinations of NC couplings from asymmetry measurements, there are various degrees of model independence with which the lineshape can be parameterised. For example, in the standard model the only significant free parameter is $M_{\rm Z}$ from which values for $\Gamma_{\rm Z}$ and the peak cross section without photonic corrections, $\sigma^{\rm pole}_{\mu\mu}$, can be calculated for a given $M_{\rm t}$ and $M_{\rm H}$. Removing the standard model constraint that $\Gamma_{\rm Z}$ is a function of $M_{\rm Z}$ allows one to test the model by comparing the measured values of $\Gamma_{\rm Z}$ and $\sigma^{\rm pole}_{\mu\mu}$ with the predicted values for the measured $M_{\rm Z}$.

4.4.1 Born cross section

The lowest order total cross section for muons can be obtained from the Born differential cross section of equation 4.6 and is given by,

$$\sigma^0(s) = \frac{8\pi\alpha^2}{3s}\left\{C_{\gamma\gamma} + C^{(1)}_{\gamma \rm Z}\Re\{\chi_0(s)\} + C^{(1)}_{\rm ZZ}|\chi_0(s)|^2\right\}, \qquad (4.13)$$

where the term from s-channel Z^0 exchange, $C^{(1)}_{\rm ZZ}$, dominates near the resonance. As the radiative corrections to this cross section are large a more detailed description of the lineshape must be used.

4.4.2 Higher order expressions

The lineshape may be cast in a more model independent form by the use of electroweak corrected partial widths, Γ_f and Γ_e, (*i.e.* corrections have been absorbed resulting in effective widths), and by replacing Γ_Z and α by their s-dependent counterparts in precisely the same way as for the improved Born approximation substitutions. Neglecting the external fermion masses, the one-loop electroweak corrected total cross section may be approximated by, [16, p 99],

$$\begin{aligned}\sigma_w(s) \quad = \quad & \left\{ \frac{s}{(s-M_Z^2)^2 + s^2{\Gamma_Z}^2/M_Z^2} \left[\frac{12\pi\Gamma_e\Gamma_\mu}{M_Z^2} + \frac{I(s-M_Z^2)}{s} \right] \right. \\ & \left. + \frac{4\pi}{3} \frac{{Q_\mu}^2\alpha^2(M_Z^2)}{s} \right\} (1+\delta_{\rm QCD}), \qquad (4.14)\end{aligned}$$

where I is an interference term (explicit form given in [16, p 94]). It is of order $\frac{\alpha}{M_Z}$ multiplied by the vector and axial vector couplings of both initial and final state fermions and is therefore negligible for muons pairs (and largest for d-type quarks). The term $\delta_{\rm QCD}$ is of order 4% and only applies to hadronic final states.

This expression is a very good approximation to the exact calculation, the discrepancy being of order 0.3% near to the resonance. With the weak corrections adequately parameterised, the photonic corrections must be included to obtain a realistic description of the lineshape. This may be performed numerically by convolution with an appropriate photon distribution function. It is also possible to obtain an approximate analytic expression for the cross section, folded with a first order (exponentiated) photon cross section. This latter approach is used to extract lineshape parameters from muon pair data and is included for completeness in Appendix C.

4.5 Radiative corrections to $A_{\rm FB}(s)$ and $\sigma(s)$

The purpose of this final section is two-fold. The first objective is to present a concise summary of the effect of radiative corrections on the forward-backward asymmetry and cross section that are the foundation of the main analysis presented in this thesis. Where these effects are relatively large, they must be well understood and calculable to allow the extraction of other physical parameters from the measurements of $\sigma(s)$ and $A_{\mathrm{FB}}(s)$. The various levels of initial state photonic corrections are treated separately in the case of the cross section for this reason. The effects are summarised by evaluating cross sections and asymmetries, corrected to various orders, and presenting the resulting distributions. The cross sections and asymmetries are determined using semi-analytic calculations.

The second objective of the section is to compare the results of two semi-analytic calculations and one Monte Carlo event generator that are used in the analysis of real data later in this thesis. The total cross section is used for this comparison as it is the only quantity that all three calculate directly. More detailed studies have been performed along similar lines in the past [17, p 102]. In addition to illustrating the good agreement between different calculations, this study is a useful check for the existence of bugs introduced in tailoring these pieces of software for analysis purposes.

4.5.1 Modification of $A^0_{\mathrm{FB}}(s)$

Following a qualitative argument used earlier to explain the large reduction of the peak cross section as a result of initial state radiation, the effect of such radiation upon the forward-backward asymmetry is expected to be a global shift towards more negative asymmetries at all energies in the vicinity of the Z^0. The shift is anticipated to be greater at centre of mass energies a few GeV above the Z^0 as more energy is radiated from the initial state, leading to a distortion of the asymmetry as a function of $\sqrt{s}$ with respect to the lowest order form.

The integrated muon pair forward-backward asymmetry is calculated by the semi-analytic program ZFITTER, which can be used to perform a full standard model calculation of this quantity. The program is based upon a complete one-loop calculation of weak corrections with photonic effects calculated complete to $O(\alpha)$ with exponentiation in both initial and final states, with leading terms from second order in the initial state. Vertex and box diagrams are also calculated.

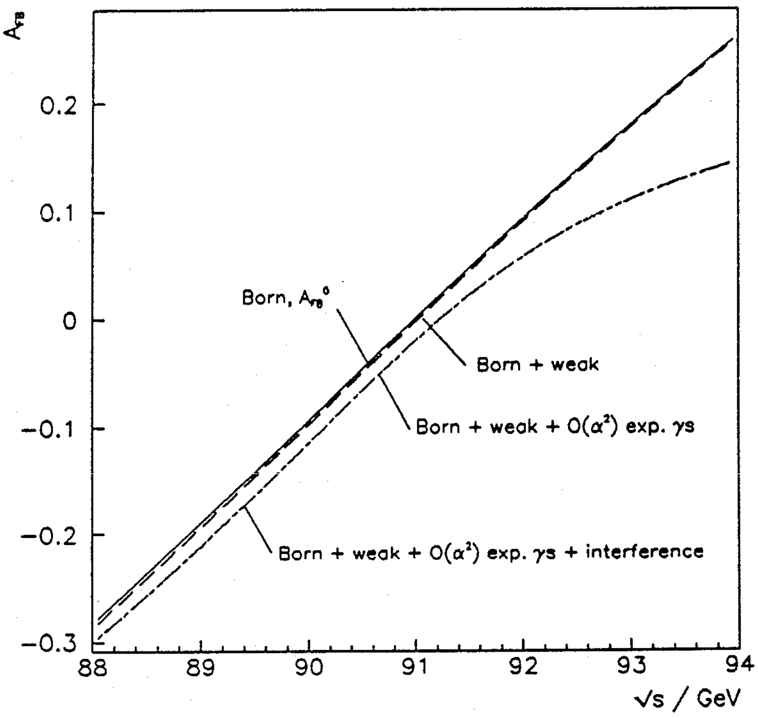

Figure 4.4: $A_{\mathrm{FB}}(s)$ including various classes of correction.

Several illustrative calculations are carried out, the results of which are presented in figure 4.4. The different levels of detail to which $A_{\mathrm{FB}}(s)$ is calculated are:

1. Lowest order asymmetry, no corrections on tree level calculation.
2. Lowest order with weak corrections only.
3. Weakly corrected asymmetry with $O(\alpha)$ initial state radiation, leading terms from $O(\alpha^2)$ and exponentiation.
4. As above with the addition of $O(\alpha)$ exponentiated final state radiation and initial-final state interference.

The standard model input to this calculation was $M_{\mathrm{Z}} = 91.18$ GeV and $M_{\mathrm{H}} = M_{\mathrm{t}} = 100$ GeV. The lower limit on the invariant mass of the final state muon pair was $4M_\mu^2$ for calculations including photonic corrections. It can be seen that the correction to the asymmetry is large well above M_{Z} and relatively small and uniform, close to and below M_{Z}. The most significant modification to the asymmetry of those considered is the result of photonic corrections to the initial state.

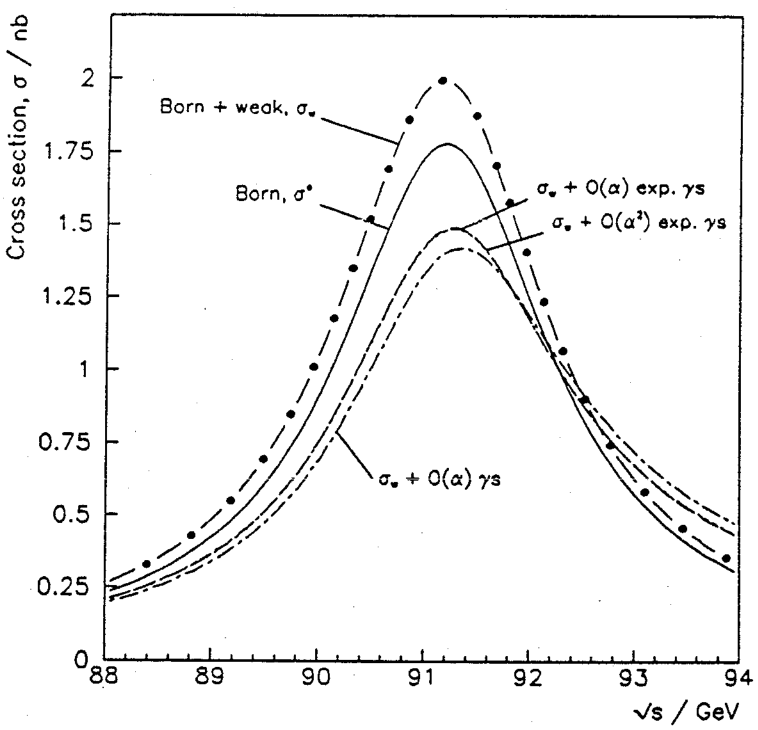

Figure 4.5: $\sigma(s)$ including various classes of correction.

4.5.2 Modification of $\sigma^0(s)$

The total cross section for muon pair production is reduced by approximately 40% at the peak of the resonance as discussed above. Other corrections significantly modify the cross section but to a far lesser extent than the previous correction. The large reduction quoted is from the weakly corrected rather than the lowest order cross section. The total muon pair cross section has been determined using the semi-analytic program ZSHAPE [44], which is considered the most complete calculation of this cross section at the current time [17, p 113]. This program performs a complete one-loop weak calculation, with initial state photonic corrections of $O(\alpha^2)$, final state photonic corrections of $O(\alpha)$ and exponentiation in both cases. All self-energies and vertex corrections are evaluated.

The cross sections that have been evaluated, using the standard model input $M_Z = 91.18$ GeV and $M_H = M_t = 100$ GeV, are the following:

1. Born cross section, no corrections applied.

2. Born cross section with weak corrections.

3. Weakly corrected cross section with $O(\alpha)$ initial state radiation.

4. As above but with exponentiation of the initial state photons.

5. Weakly corrected cross section with $O(\alpha^2)$ initial state radiation and exponentiation.

The various lineshapes are shown in figure 4.5. In all calculations with photonic corrections, the lower limit on the invariant mass of the muon pair was $4M_\mu^2$. The main point of interest is the relative size of the $O(\alpha^2)$ photonic corrections with respect to the $O(\alpha)$ corrections: the difference is very small. (To avoid confusion, only initial state photonic corrections have been evaluated here.) This implies that the effect of successive corrections to the initial state appear to be converging even at $O(\alpha)$ when exponentiation is included. This observation is used later to justify fitting an analytic expression for the lineshape, calculated to $O(\alpha)$ with exponentiation, to experimental data.

4.5.3 Comparison of cross section calculations

In analysing real data it is always necessary to have a cut on the minimum invariant mass of the muon pair, s'. Even if this cut is not explicit, it will exist if muon chambers or calorimeters are used to detect muons as the material in front of these components will prevent muons below a certain threshold from being correctly identified. This *lower* limit on the muon pair invariant mass defines an *upper* limit on the amount of energy that may be radiated in the form of photons and must therefore be known in order to evaluate photonic corrections. The effect of this cut on the observed cross section is small but not negligible. A typical experimental cut is $s' > 100$ GeV^2.

The comparison performed below illustrates the size of the correction to the total cross section that such a cut produces and the extent to which the three programs considered agree when subject to this cut. The programs that are compared are `ZFITTER` and `ZSHAPE`, as used above and the Monte Carlo program `KORALZ` [45]. This latter is considered the most complete muon pair event generator available [16, p 127] and includes initial state radiation to second order with exponentiation,

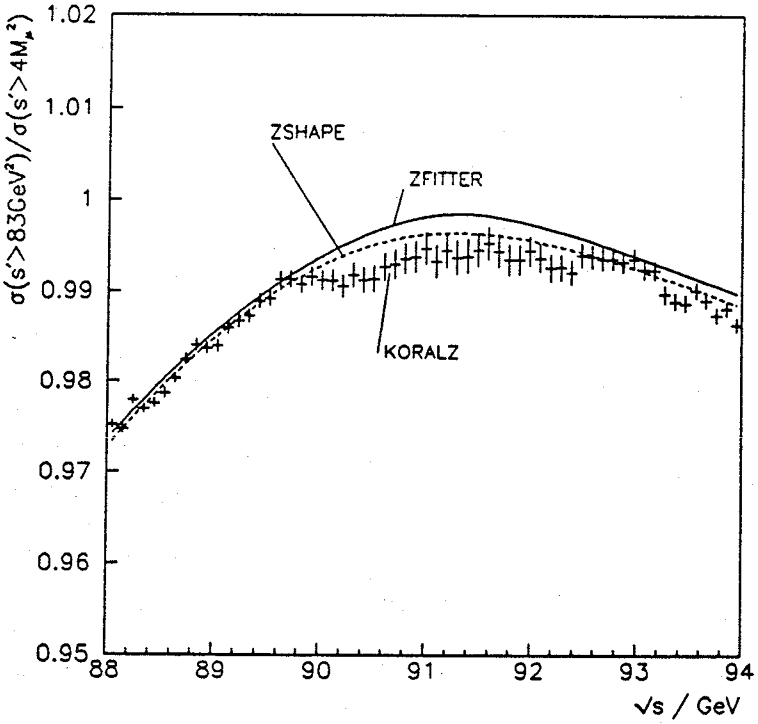

Figure 4.6: $\sigma(s)$ with $s' > 83$ GeV^2 relative to $\sigma(s)$ with $s' > 4M_\mu^2$.

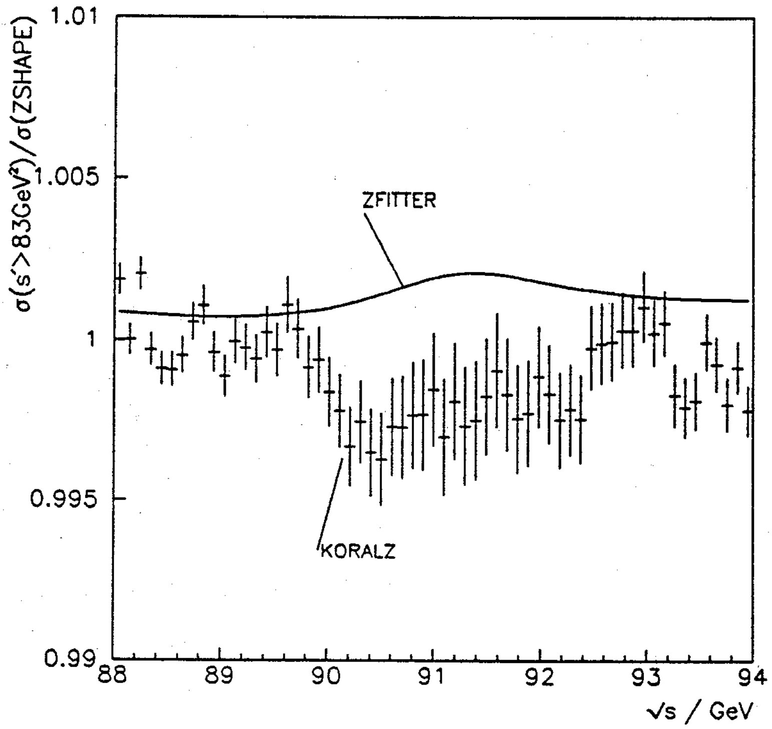

Figure 4.7: $\sigma(s)$ with $s' > 83$ GeV^2 relative to ZSHAPE $\sigma(s)$ with $s' > 83$ GeV^2.

whilst final state radiation is restricted to first order. Initial-final state photonic interference is not included: however, this is predicted to be a small effect, modifying $A_{\rm FB}(s)$ by less than 10^{-3} if only relatively loose cuts are applied to the phase space of photons [48]. In the sense used here, a loose cut is one that only affects photons with energies greater than 10 GeV.

In order to make a comparison of quantities that are nominally the same, all programs are restricted to $o(\alpha^2)$ exponentiated photonic corrections in the initial state, and no final state corrections are included. The standard model input to the calculations is $M_Z = 91.18$ GeV and $M_H = M_t = 100$ GeV, and the invariant mass cut used is given by $s' > 83$ GeV^2. (The s' cut in `KORALZ` is actually specified as a fraction of the centre of mass energy rather than as a fixed value for all energies. The fixed $s' > 83$ GeV^2 cut is obtained by taking the average of $s' = 0.01s$ evaluated at the limits of the energy range considered. The discrepancy between specifying the cut as $s' > 83$ GeV^2 and $s' = 0.01s$ is equivalent to a difference of less than 0.3 GeV in the centre of mass energy.)

The results are summarised in two figures. In figure 4.6, the cross sections evaluated by each of `ZSHAPE`, `KORALZ` and `ZFITTER` subject to the s' cut above are divided by the cross section predicted by `ZSHAPE` with the minimum invariant mass cut of $s' > 4M_\mu^2$. The error bars on the cross sections evaluated by `KORALZ` are statistical. The lineshapes are all in reasonable agreement and the net effect of this cut on the cross section is seen to be an overall reduction in the cross section of approximately 1%, the effect being largest below the peak and smallest on peak. In order to see more clearly the extent to which the programs agree, the cross sections evaluated by `ZFITTER` and `KORALZ` are divided by that evaluated by `ZSHAPE`, where all cross sections are those evaluated with the large s' cut. The results of this procedure are given in figure 4.7.

The level of discrepancy between the semi-analytic programs is less than 0.2% whilst that between the Monte Carlo and `ZSHAPE` is less than 0.3% at all centre of mass energies considered. It is concluded that the predictions of these three programs are in good agreement with one another and they may be used with confidence in analysis of muon pair data.

Chapter 5

Selection and analysis of muon pair events

The main analysis presented in this thesis is a measurement of the electroweak parameters M_Z, Γ_Z, $\sigma_{\mu\mu}^{\text{pole}}$ and combinations of the effective couplings, $\hat{a}_l$ and $\hat{v}_l$. The experimental input to this analysis is a set of muon pair asymmetries and cross sections calculated at various centre of mass energies between 88 GeV and 94.5 GeV. The data set used consisted of all muon pair events recorded in OPAL during the 1990 run, in which LEP delivered an integrated luminosity of approximately 8.7 pb^{-1}.

This chapter describes the calculation of these asymmetries and cross sections, including the main triggers used to detect muon pairs, the cuts imposed to isolate them from other final states, an estimate of background contamination and corrections applied to the data. A measurement of the $\mu^+\mu^-\gamma$ (colinear γ) cross section is also presented.

5.1 The OPAL trigger and filter

In the current 4-bunch operation of LEP, bunch crossings occur at a frequency of 45 kHz. With typical luminosities in 1990 of $4 \times 10^{30}\text{cm}^{-2}\text{s}^{-1}$, the rate of Z^0 production and decay to observable final states is approximately 0.14 Hz on resonance. Although the probability of a genuine e^+e^- interaction in any given bunch crossing is very low, the ambient rate is increased by background processes such as cosmic

θ bin	$\cos\theta$ range
θ_1	-0.980 - -0.596
θ_2	-0.823 - -0.213
θ_3	-0.596 - 0.213
θ_4	-0.213 - 0.596
θ_5	0.213 - 0.823
θ_6	0.596 - 0.980

ϕ bin	ϕ range ($^\circ$)
ϕ_1	0 - 30
ϕ_2	15 - 45
ϕ_3	30 - 60
...	... ...
ϕ_{23}	330 - 360
ϕ_{24}	345 - 15

Table 5.1: θ-ϕ segmentation of the detector at the trigger level

rays, beam-gas interactions, synchrotron radiation and interactions between off-momentum beam particles and the wall of the beam pipe leading to hadronic or electromagnetic showers. The purpose of the triggering system is to select bunch crossings in which an interesting interaction has occurred and to reject background without introducing biases, whilst keeping the deadtime of the detector as small as possible. This is achieved by means of a two level trigger and is summarised below.

5.1.1 First level trigger

The first level trigger [49] makes a decision in the 22 μs between successive bunch crossings as to whether or not a given event should be read out. If an event is to be rejected, reset signals are sent to each sub-detector 6 μs before the next bunch crossing. The average rate of the first level trigger during the run was approximately 2 Hz leading to a deadtime of about 5% as the readout time of OPAL is 25 ms. The first level trigger incorporates signals from most sub-detectors and events may be selected on the basis of a number of independent criteria. This redundancy for event selection leads to a high detection efficiency which may be reliably measured. Triggers may be either 'standalone' or formed by spatial correlations between detectors.

Standalone signals are typically total energy sums or segment multiplicities within sub-detectors; thresholds for standalone trigger signals are high in order to avoid noise problems with summations extending over a large number of electronic channels. Spatial correlations are made by dividing the 4π solid angle into 144 overlapping bins, 6 in θ and 24 in ϕ, and requiring sub-detectors to supply trigger signals from zones corresponding (as closely as possible) to the mapping of this θ-ϕ 'matrix'. The definition of the bins in the θ-ϕ matrix is shown in table 5.1. As the area of each θ-ϕ bin is comparatively small, electronic noise from summing over all channels in a given θ-ϕ zone allows relatively low thresholds to be used in the formation of θ-ϕ signals compared to standalone triggers. For example, a typical standalone trigger is EBTOTLO, the minimum summed energy in the barrel ECAL, which has a threshold of 4 GeV whereas the threshold for an ECAL θ-ϕ input signal is 1 GeV.

The θ-ϕ signals are used to detect spatial coincidences between sub-detector triggers and in the definition of back-to-back hits. The central trigger logic of the trigger system makes a decision to accept or reject each event on the basis of programmable criteria that the θ-ϕ signals and standalone triggers are required to satisfy. In 1990, OPAL recorded approximately 5.2 M first level triggers. The main features of the three most important sub-detector triggers for muon pairs are briefly summarised below; the ECAL trigger is not described as it was unable to trigger on minimum ionising particles during the 1990 run.

Track trigger

The track trigger is a fast pattern recognition processor that identifies tracks originating from the vicinity of the interaction point in the region $|\cos\theta| < 0.95$. It makes use of the fact that charged tracks with moderate momenta transverse to the beam axis ($p_T > 0.25$ GeV), have approximately linear trajectories in the r-z plane due to the axial field of OPAL, *i.e.* a $\frac{z}{r}$ distribution for all hits on a good track would ideally be a narrow cluster centred at a well-defined value of $\frac{z}{r}$ ($\equiv \cot\theta$). In order to avoid looking at $\frac{z}{r}$ for all hits in the central detector, the track trigger only considers four annular groups or 'rings' of 12 (adjacent) wires, one ring consisting of all the axial wires of the vertex chamber, the remaining three rings being at various (and variable) radii within the jet chamber.

Each ring is effectively divided into 24 overlapping azimuthal sectors of 30°, corresponding to the ϕ bins in the θ-ϕ matrix, and up to 32 θ bins (only 18 are used at present). The overlaps in ϕ are introduced to allow for curvature in the r-ϕ plane causing tracks to cross sector boundaries and neighbouring θ bins are combined to define boundaries. Histograms of $\frac{z}{r}$ are filled for hits in each ϕ sector of each ring and the contents of each bin compared with programmable thresholds. Coincidences between $\frac{z}{r}$ bins in different rings are used to categorise the track multiplicity as 0, ≥ 1, ≥ 2 or ≥ 3, over the whole detector or restricted to the barrel region, and form standalone triggers (TM1, TBM1, ...). The track trigger produces further standalone triggers, generated by summing hit counts in each ring (VXH, JH1, ...) and by identifying tracks with very high or low charge, as well providing input to the θ-ϕ matrix.

Muon trigger

Triggering in the muon detectors is performed separately in the endcap and barrel regions. The muon barrel, with no z resolution for triggering purposes and segmented into 24 ϕ sectors, provides 24 θ-ϕ input signals each of which corresponds to a single ϕ bin summed over the bins θ_2–θ_5. In addition, a standalone trigger formed by the logical OR of all ϕ bins (MBH). A ϕ sector is required to have hits in 3 out of 4 layers of drift chambers to form a trigger signal.

The basic muon endcap trigger signals are formed by the summation of induced charge on groups of either 64, 96 or 128 adjacent readout strips. These are arranged to form non-overlapping θ-ϕ bins (providing coverage in bins θ_1, θ_2, θ_5 and θ_6) to increase the information of each signal, although some ambiguity between adjacent bins is unavoidable as the muon endcap geometry is Cartesian. The minimum requirement for a θ-ϕ signal is that there are at least two active trigger zones that are consistent with a track originating from the interaction region in both xz and yz projections, with one zone in an inner endcap and one in an outer endcap. The tolerance on this limited pointing cut is typically equivalent to ±45°. In addition to 96 θ-ϕ signals, the muon endcap supplies three standalone triggers, two corresponding to hits in either endcap individually (MEL and MER) and a third corresponding to a loosely colinear match between hits in either endcap (MELR). 'Loosely colinear' is used to mean that at least one hit in the left endcap is matched with a hit in the right endcap in the equivalent θ bin with the opposite sign of x co-ordinate. A more detailed description of the muon endcap trigger is given in [50].

ToF trigger

The ToF trigger signals are formed by coincidences between phototubes at either end of the long scintillator bars, where all coincidences must occur within ±50 ns of the beam crossing. As with the muon barrel, there is no θ information available. The ToF bars are merged in groups of 6 or 7 to form 15° ϕ sectors which are subsequently combined in pairs to form 24 overlapping sectors of 30°. Standalone triggers from the logical OR of all ToF bars (TOFOR), the multiplicity of ToF bars (TOFMUL) and the multiplicity of overlapping ϕ sectors (TOFMANY) are provided in addition to the θ-ϕ input signals.

5.1.2 Second level trigger

The second level trigger or 'event filter' [23, pp 33–35] works by identifying and rejecting background events rather than by attempting to recognise and accept interesting events. In this sense, it is a rather conservative system, reducing the likelihood of rejecting new physics events with unknown topologies. The filter processor decision is based on a fast analysis of the entire event (performed in a multiprocessor 68020/68030 [52] environment) in which attempts are made to verify all first level trigger signals, having found ECAL clusters and identified muons. The online reconstruction of jet chamber track segments forms a central part of this analysis.

At the start of the 1990 run events flagged as 'junk' by the filter were recorded on magnetic tape with other data passing the first level trigger; events flagged as junk were not reconstructed. This is 'passive' filtering. 'Active' filtering, in which junk events were not even recorded, was introduced early in the run. The filter flagged a total of 1.2 M (23%) of all first level triggers as junk, of which 536 k (10%) were not written to tape. The remaining 4 million events which were accepted by the filter were reconstructed by ROPE.

5.1.3 Triggers for muon pair events

The trigger processors above provide a high degree of redundancy, particularly in the barrel region where ToF, muon and track triggers all overlap. By careful choice of event samples selected on the basis of one trigger, the efficiency of other available triggers may be deduced in given angular regions. This is straightforward for muon pairs as the events have a simple topology. Using a subset (60%) of the events in this analysis, the overall first level trigger efficiency for muon pairs has been estimated to be 99.8 ± 0.2% whilst the filter has been estimated to be more than 99.9% efficient [20].

5.2 Data selection

With a total integrated luminosity delivered to OPAL of 8.7 pb^{-1}, the maximum number of Z^0 decays that would be expected assuming, a standard model resonance cross section to charged final states of 35 nb, is approximately 305 k if all data was accumulated at the peak. This crude estimate suggests that at most 8% of the 4 M events reconstructed within OPAL during the run originate from genuine Z^0 decays. For this reason, as well as purely logistical problems associated with handling such large amounts of data sparsely populated with interesting events, a further loose selection (called 'PHYS1') was performed after each event had been reconstructed. DST records for all events that satisfied the PHYS1 criteria were accumulated on disk throughout the duration of the run to improve access to the data for analysis.

5.2.1 The PHYS1 selection

One of the last stages in the reconstruction process is the assignment of loose (inclusive) event classifications based upon information from the first level trigger, the filter and the reconstructed physics quantities. These classifications are packed into a single event type word in the 'header' of each event to improve efficiency when analysing a large sample of the data or when separating a given type of events from the main DST stream. Each DST record consists of a relatively small header of 40 (32-bit) words and a much larger 'event part', which is typically a few tens of kB. Before detailed analysis can be carried out, the event part of the DST must be read which requires CPU time to relocate the data structure into memory and to carry out format conversions. A large improvement in processing speed is achieved if all decisions to reject events are made on the basis of information stored in the header alone, thus reducing the amount of unnecessary data read.

The standard event classifications that are performed are preselections for many analyses and together they comprise the PHYS1 data stream. The current definition of PHYS1 includes preselections for multihadrons (two slightly different selections are in use), single photon triggers, tagged two-photon events, Higgs searches, heavy lepton searches and charged lepton pairs. In addition, the PHYS1 data includes so-called 'luminosity' events, *i.e.* very small angle scattered Bhabha events that are recorded by the forward detector and used to measure the luminosity in a given period of data taking. The retention of the headers of these events in the PHYS1 data set (or any other subset of the data, such as the lepton pair preselection) enables cross sections to be calculated in straightforward manner [53], the essence of which is to simply count the number of such events.

5.2.2 Lepton pair preselection

The lepton pair preselection, which is divided into a positive lepton pair identification and a high multiplicity (or multihadron) veto, is defined by the following criteria:

Positive selection An event is selected if it includes,

- at least two ECAL clusters both having transverse energy, $E_{\mathrm{T}} > 6.0$ GeV (potential Bhabha candidates), or
- at least two ECAL clusters, one of which has $E_{\mathrm{T}} > 2.0$ GeV, that are back-to-back within 25° in ϕ (potential tau candidates), or
- at least one track with $p_{\mathrm{T}} > 1.0$ GeV, $|d_0| < 1.0$ cm, $|z_0| < 20.0$ cm that has a minimum of 30 hits, summing hits from vertex, jet and Z chambers (potential muon candidates).

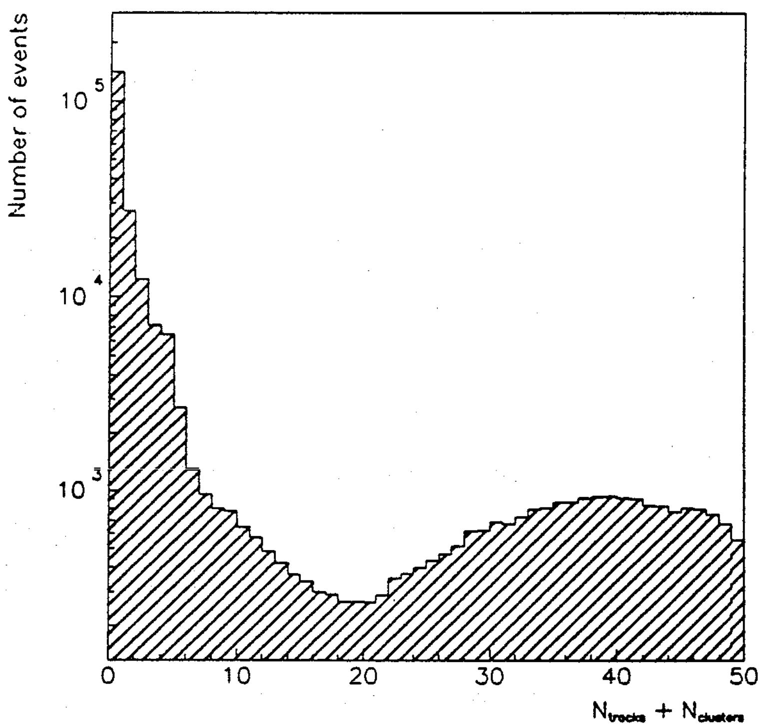

Figure 5.1: Combined ECAL cluster and track multiplicity, showing high multiplicity veto cut.

High multiplicity veto An event is rejected if it satisfies,

- number of ECAL clusters + number of charged tracks > 17

For the purposes of counting in this test (and in all subsequent analysis):

- Endcap ECAL clusters are used if they have energy, $E > 0.2$ GeV and contain a minimum of 2 blocks with no single block containing more than 99% of the total energy of the cluster.
- Barrel ECAL clusters are used if they have energy, $E > 0.1$ GeV.
- Tracks are used if they satisfy the same charged track quality cuts as used in the positive selection with the additional requirement that the first hit on each track must occur within 75.0 cm of the beam axis.

The distribution on which the high multiplicity veto cut is imposed is illustrated in figure 5.1 (with logarithmic scale), showing a clear separation of events in the region of the cut. The purpose of the tighter restrictions imposed on endcap ECAL clusters is to avoid rejecting events in which some endcap lead glass blocks had excessive noise due to hardware and pedestal problems. These were corrected in later processing, but not before the preselection was made during online reconstruction.

Two bits, which are set in the event type header word if an event passes the positive selection and fails the high multiplicity veto, are all that is required thereafter to rapidly identify events comprising the lepton pair preselection. The identification of muon pair events from this combined lepton pair data sample is presented below.

5.3 Muon pair selection

Events are regarded as muon pair candidates if they contain a minimum of two good quality charged tracks, both of which are identified as muons, and they pass a small number of simple cuts to reject residual background from cosmic rays, two-photon events and tau pairs. A 'good quality' track is defined as one that is formed from at least 30 central detector points, the first of which must be no more than 75.0 cm from the beam axis, with momentum $p > 6.0$ GeV, $|d_0| < 1.0$ cm and $|z_0| < 20.0$ cm. Imposing a cut on the minimum momentum allowed for each of two charged tracks in a candidate event reduces the background from tau pair and two photon events, whilst the cut on d_0 eliminates part of the cosmic ray background.

In order to be identified as muons a good charged track is required to either,

1. have $p > 15$ GeV and less than 3 GeV deposited in the ECAL inside a cone of half angle 200 mrad around the track, where the angle is defined in the r-ϕ plane, or

2. have associated activity in the muon chambers or the HCAL or both.

There are small regions of OPAL where there is no coverage by the muon system, either due to gaps in the acceptance (approximately 94% and 97% of the solid angle is instrumented by muon chambers and HCAL respectively) or as a result of infrequent hardware problems with the constituent sub-detectors. It is in these areas that the identification of muons using the ECAL is most important.

The loose cut on the electromagnetic energy associated with a track avoids accepting Bhabha events without undue risk of rejecting muons which, being minimum ionising particles, will only deposit approximately 600 MeV in the lead glass. The association between ECAL and charged track information is not carried out in three dimensions because of imperfections in the z resolution of the jet chamber which result in a slight degradation of θ measurements. This is in contrast to the excellent ϕ (and hence momentum) determination by the jet chamber.

As the HCAL and muon chambers are less homogeneous than the ECAL, the association of charged tracks with activity in the muon system is correspondingly more involved. The slightly different criteria used to define the matching between tracks and the four currently used components of the muon system are given below.

5.3.1 Association of charged tracks with the muon system

The matching of hits in the muon system with charged tracks is carried out during the generation of DST records by comparing the trajectory of the track with the appropriate quantity from the muon system, the objective being to indicate in which layers of the muon system there is activity related to the presence of the track. For every charged track in the DST the result of this association is stored in one word, where each bit set indicates that the track in question matches muon activity in a given layer of the HCAL or muon chambers. (Details of the implementation of this scheme are given in [54].) A more thorough match is also performed during the reconstruction, using both the position and trajectory of the muon and charged track segments—for the simple event topologies of muon pairs this more thorough matching is not necessary.

The association is performed by means of a comparison in the r-ϕ plane for the HCAL and muon barrel sub-detectors having cylindrical geometries, whereas a change of co-ordinates is necessary to incorporate data from the endcap detectors. It is necessary to propagate the charged tracks through the material of the detector, taking into account multiple scattering, energy loss and the magnetic field in the iron return yoke of the coil, in order to obtain a meaningful set of track parameters at the surface on which the matching takes place [34,55]. After muon activity has been associated with a track, further cuts are made to increase the likelihood that it originated from a genuine muon, *e.g.* on the number of layers containing related hits. The association is carried out for each component of the muon detector system as described below.

Muon endcap

All two dimensional xz hits are combined with all yz hits within the same streamer tube plane, forming a set of three-dimensional points. The θ-ϕ co-ordinate of each point is compared in turn with the θ-ϕ trajectory of the extrapolated track and is deemed to have matched if the differences, $\Delta\phi$ and $\Delta\theta$, satisfy

$$\Delta\phi \leq 20 \quad \text{mrad.}$$

$$\Delta\theta \leq 100 \quad \text{mrad.}$$

This match compares position measurements and does not compare directions of the muon segments and the extrapolated track. The advantage of this procedure is that acceptance in the endcap region is marginally increased at the periphery of the chambers, by effectively removing the minimum requirement that there should be at least one hit in both the the inner and outer parts of an endcap. It is implicit that all tracks originate from the interaction point. At least two such hits out of four (up to eight in the small overlap regions) must be matched to classify a charged track as a muon.

Muon barrel

Reconstructed muon barrel hits are compared directly in r-ϕ with the trajectory of the charged track. No θ information was used in the association as calibration problems rendered the z resolution of the muon barrel unreliable. A weak momentum dependence is incorporated in the matching, though the effect is limited as charged tracks below 6 GeV have been excluded. The criterion used is,

$$\Delta\phi \leq 100 + \frac{100}{p} \quad \text{mrad.}$$

where p is in GeV. At least two hits out of four must be matched to classify a charged track as a muon.

Hadron endcap

In the hadron endcap, the matching is carried out using only the yz (vertical) co-ordinate from the strip readout: information from the pads is not used. The central detector track is extrapolated to each layer of the calorimeter in turn and association takes place if the extrapolated position lies within a distance, Δyz, of the calorimeter hits, where

$$\Delta yz \leq 20 + \frac{45}{p} \quad \text{cm}$$

At least four hits out of a maximum of eight, one of which must be in the outer three layers, must be matched to classify a charged track as a muon. In addition, no layer must have more than two associated hits to suppress the association of HCAL activity from hadronic showers.

Hadron barrel

As with the muon barrel, the matching of hits is performed in r-ϕ only, with the road used for matching defined by,

$$\Delta\phi \leq 20 + \frac{100}{p} \quad \text{mrad.}$$

The only cut imposed in θ is that the track should fall within the angle subtended by a given barrel readout strip, each of which is approximately half of the length of the calorimeter. The same restrictions are applied to the number of associated hits as in the hadron endcap.

5.3.2 Rejection of remaining backgrounds.

The dominant backgrounds are from cosmic rays, $\tau^+\tau^-$ and two photon events and the means whereby these different types of event are removed from the data sample are described in detail below. Rejection of cosmic rays is very efficiently carried out by the imposition of simple cuts, based on either timing information of the muons as measured by the ToF or on the quality of the muon tracks measured within the central detector. The ToF covers the angular region $|\cos\theta| < 0.82$ and all candidate events with tracks inside this region are rejected if they do not have

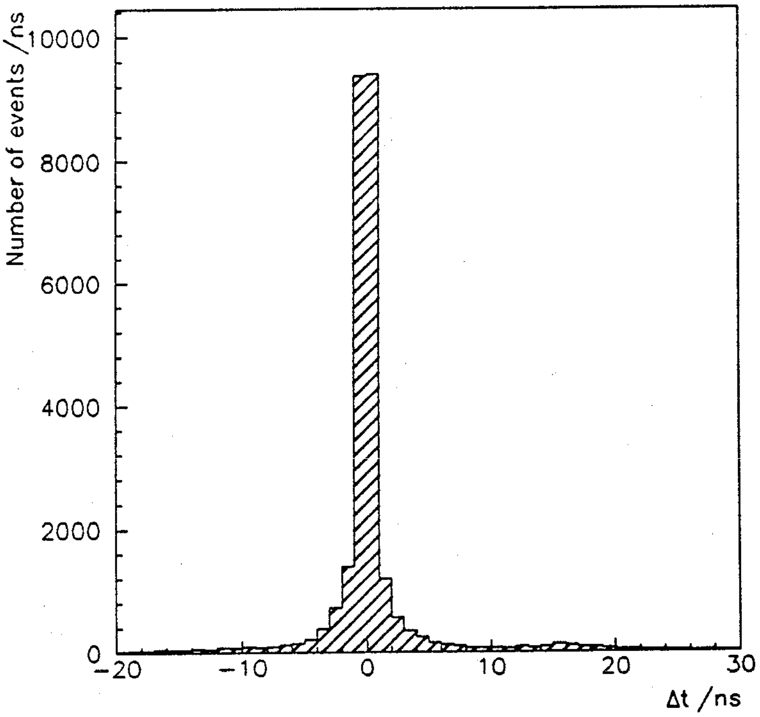

Figure 5.2: Minimum time difference between back-to-back ToF counters.

a minimum of one ToF hit, where a ToF counter is only required to have a signal at one end to be included in the definition of a ToF hit. In most cases two or more hits are present. In events containing two ToF hits that are separated by more than 165^0 in ϕ, the minimum relative time difference, Δt, between hits is required to be less than 10 ns. The distribution of the time differences for such back-to-back ToF hits for a sample of events from the lepton pair preselection is shown in figure 5.2.

The reason for using the relative time difference is that tracks from a particle decaying near to the interaction region will both arrive at the ToF at approximately the same time, whereas back-to-back ToF hits from cosmic rays will be separated by at least 16 ns *i.e.* the time required to travel from a scintillator bar on one side of the ToF to a diametrically opposite bar on the other side of the beam axis, a minimum distance of roughly 4.7 m. Most cosmics will fail to have any ToF hits as the detector is only sensitive for ±50 ns of the bunch crossing signal. The acceptance of the ToF is such that a genuine muon will occasionally (~2–3% probability) pass through the ToF without hitting a scintillator. In events such

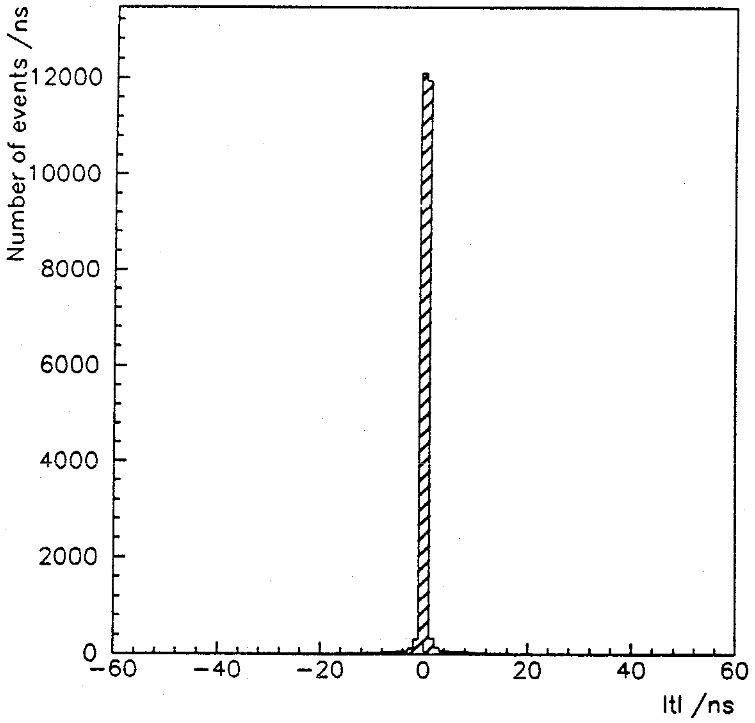

Figure 5.3: Absolute time measured for back-to-back ToF counters having $\Delta t < 10$ ns.

as this which contain only a single hit, the absolute time relative to the bunch crossing is required to be less than 10 ns. The cut is based upon the absolute time measured in events containing back-to-back ToF hits with $\Delta t < 10$ ns, the distribution of which is given in figure 5.3.

In the endcap region, cuts on the track parameters d_0 and z_0 are used to reject cosmic ray background as there is no equivalent of the ToF system. The preferred values to use for these cuts are obtained by inspecting combined distributions of $z_0^{\text{track1}} + z_0^{\text{track2}}$ vs. $|d_0^{\text{track1}}| + |d_0^{\text{track2}}|$ for barrel events which have been classified as cosmic rays or Z^0 decays, as shown in figures 5.4 and 5.5 respectively. The effectiveness of the ToF as a tool for rejecting cosmic background is apparent from the distinction between the distributions of the track quality parameters for these two classes of event.

In the region beyond the ToF, events are rejected as cosmics if they do not have two charged tracks which satisfy, $|d_0^{\text{track1}}| + |d_0^{\text{track2}}| < 0.6$ cm and $|z_0^{\text{track1}} + z_0^{\text{track2}}| < 25.0$ cm. The momentum distribution of muon candidates in the endcap region is compared with that for events which are rejected as cosmics in the same angular

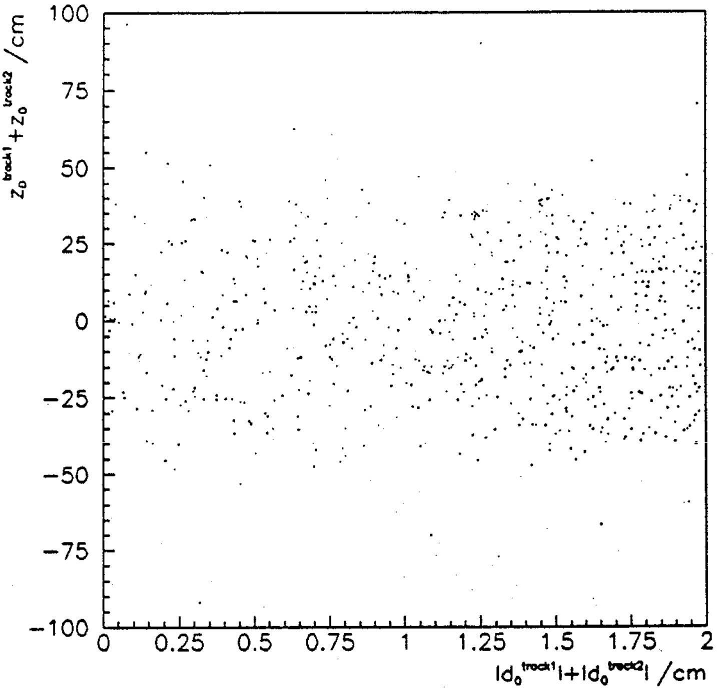

Figure 5.4: $z_0^{\text{track1}}+z_0^{\text{track2}}$ vs. $|d_0^{\text{track1}}|+|d_0^{\text{track2}}|$ distribution for barrel events failing ToF cuts (cosmics).

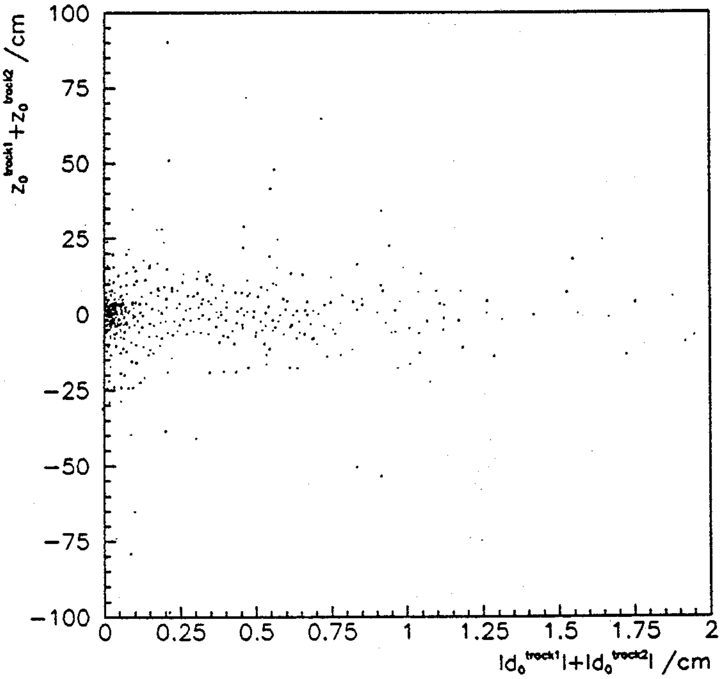

Figure 5.5: $z_0^{\text{track1}}+z_0^{\text{track2}}$ vs. $|d_0^{\text{track1}}|+|d_0^{\text{track2}}|$ distribution for barrel events passing ToF cuts (Z^0 decays).

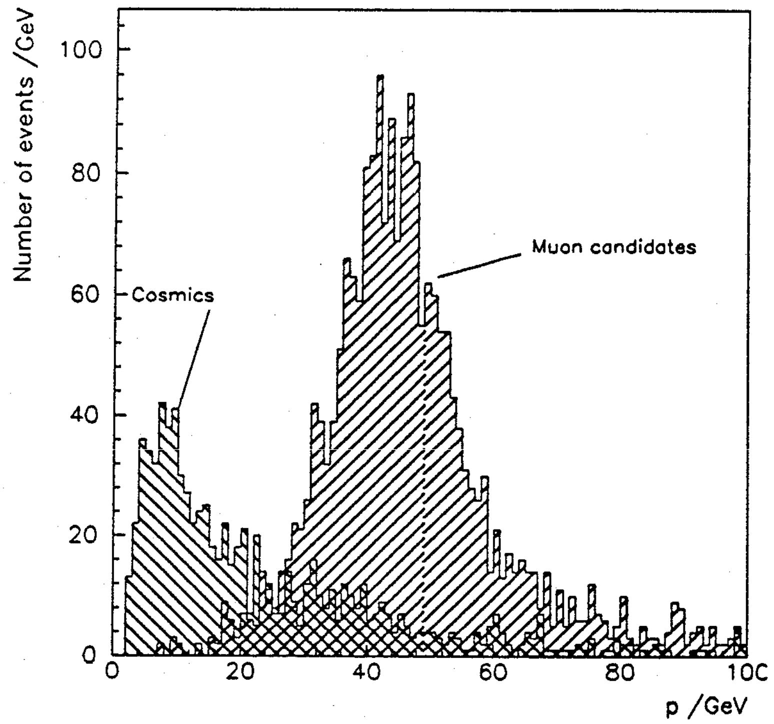

Figure 5.6: Momentum, p, for endcap muons and cosmics, as defined by d_0 and z_0 cuts.

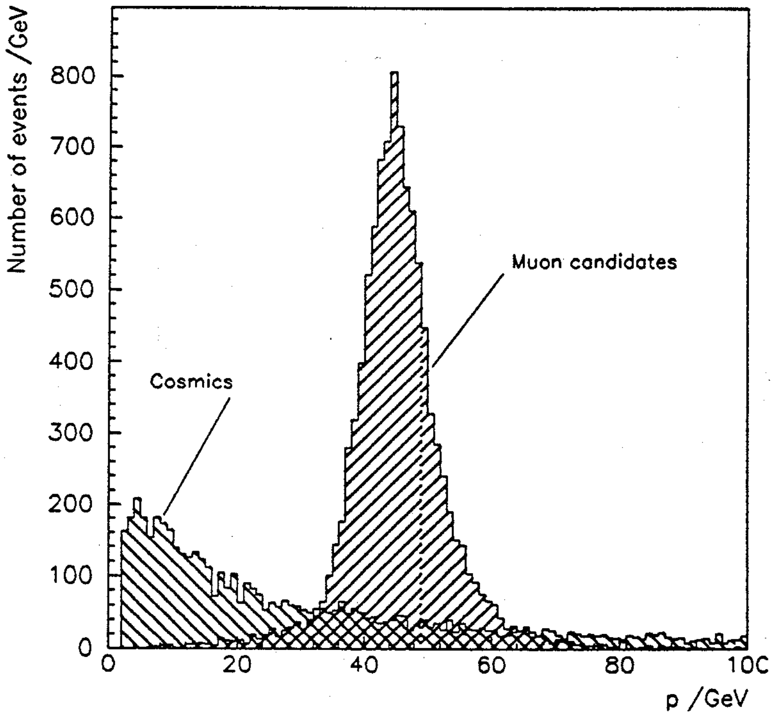

Figure 5.7: Momentum, p, for barrel muons and cosmics, as defined by ToF cuts.

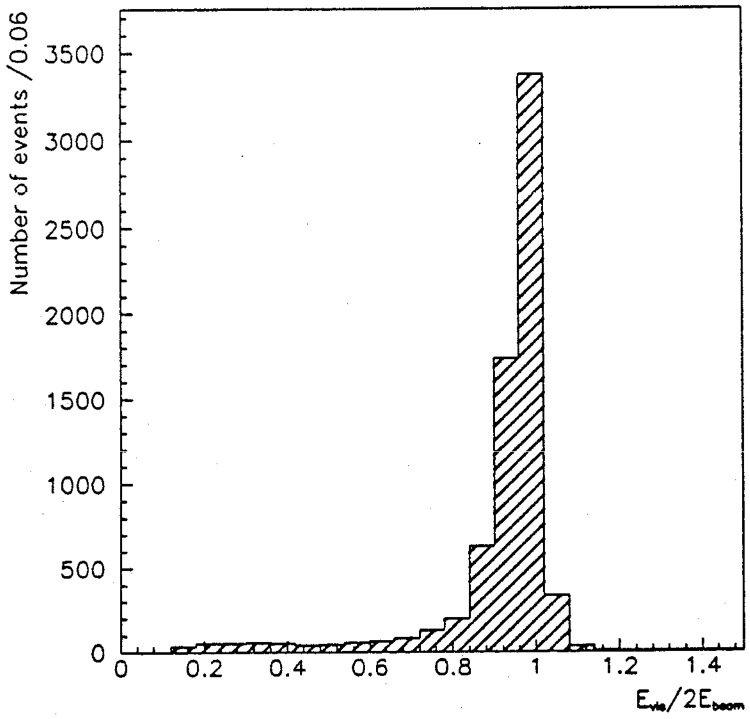

Figure 5.8: Distribution of $\frac{E_{\rm vis}}{2E_{\rm beam}}$ for muon pair candidates.

region in figure 5.6. Analogous distributions are shown in figure 5.7 for barrel events, where the better momentum resolution of the detector at larger polar angles is apparent. These distributions indicate that most of the events that are rejected are cosmics, without discarding a significant fraction of genuine muon pair events.

5.3.3 Rejection of $\tau^+\tau^-$ and two-photon events

The largest fraction of these events may be removed by applying a cut on the total visible energy of the event, $E_{\rm vis}$, defined as the sum of the energy of the two muon track candidates and the highest energy photon (if any photons are present). Charged particles with momenta measured to be greater than the beam energy are assumed to have momenta equal to the beam energy. A photon is defined as an ECAL cluster that is not associated with a charged track and the muon track candidates are taken as the two highest momentum tracks that have an acoplanarity, ξ, such that $\cos\xi > -0.95$, *i.e.* the muons must be separated by more than 18.2° in the r-ϕ plane. The main purpose of the latter cut is to prevent a relatively poor quality track, which may occasionally be reconstructed as more than one track, from being identified as a muon pair. Events are classified as muon pair events if they satisfy,

$$\frac{E_{\mathrm{vis}}}{2E_{\mathrm{beam}}} > 0.6.$$

where E_{beam} is the energy of one beam. The distribution on which this cut is imposed is shown in figure 5.8 for muon candidates after all other cuts have been applied.

Throughout the analysis, no restriction has been made on the acolinearity, ζ, of the muon pairs. A cut that is sufficiently weak that it does not significantly affect the cross section has been observed to have a minimal effect on background rejection when used in conjunction with the cuts described above. For example, rejecting events with $\zeta > 15°$, a cut proposed as being weak in the sense used above [56], rejects 1.4% of muon pair candidates after all other cuts above have been applied without rejecting any additional (Monte Carlo) tau pair events, as used in the study carried out below.

The resultant efficiency of these cuts for selecting muon pairs has been estimated by a Monte Carlo study, details of which are given in section 5.6.1, to be $98.8 \pm 0.1\%$ within the angular region $|\cos\theta| < 0.95$. The level of background present in the final muon pair sample is estimated in a similar manner as described below.

5.4 Estimate of background contamination

The level of background contamination after all analysis cuts have been applied is evaluated by using the full OPAL analysis chain. For each background process considered, Monte Carlo event generators are used to produce simulated 4-vectors which are processed by `GOPAL` to reproduce the combined effect of measurement by the various detectors, including inefficiencies and resolutions. The simulated raw data is subsequently reconstructed by `ROPE` and finally analysed by the same software as used to study real data, thus ensuring that the Monte Carlo data is subjected to precisely the same cuts.

Four principle sources of background are considered, *viz.* tau pairs, Bhabhas, multihadrons and two photon events. All are generated with comparable standard model input parameters and at centre of mass energies within 0.2 GeV of M_Z. Relevant features of each 4-vector sample are presented below.

Tau pairs

A sample of 10000 events, generated by the `KORALZ` program at a centre of mass energy of 91.17 GeV, was used. Initial state radiative corrections of $O(\alpha^2)$ with exponentiation of soft photons, final state radiation of a single final state photon and a leading log approach to incorporate weak effects [57] are included in the simulation. Standard model parameter values used were $M_Z = 91.17$ GeV, $M_t = 150$ GeV and $M_H = 100$ GeV. The photon system was permitted to take no more than 90% of the available centre of mass energy (*i.e.* the minimum invariant mass squared of the muon pair, $s' \geq 0.01s$). This simulated set of events corresponds to an integrated luminosity of 6.8 pb^{-1}.

Bhabhas

The data sample consisted of approximately 14000 Bhabha events, generated by the `BABAMC` program [58] at a centre of mass energy of 91.25 GeV. This generator does not include higher than $O(\alpha)$ radiative corrections nor does it include exponentiation of soft photons; consequently the cross section for the process is obtained from another source [59]. Events were generated within a limited angular range defined by $|\cos\theta| < 0.976$. Standard model parameter values used were $M_Z = 91.135$ GeV and $M_t = M_H = 100$ GeV. This set of events simulates the yield from an integrated luminosity of 4.2 pb^{-1}.

Multihadrons

A sample of approximately 51000 multihadronic events, generated with the `JETSET` program [60] at a centre of mass energy of 91.2 GeV, was used. This generator includes initial state radiation at $O(\alpha)$ without exponentiation and does not incorporate any weak loop effects. The standard model parameters used were

Process	Events accepted/Total	σ(accepted)/σ(muons)
$e^+e^- \rightarrow \tau^+\tau^-$	$\frac{106}{10000}$	0.011±0.001
$e^+e^- \rightarrow e^+e^-$	$\frac{0}{13999}$	< 0.001
$e^+e^- \rightarrow q\bar{q}$	$\frac{0}{51042}$	< 0.001
$e^+e^- \rightarrow e^+e^-\mu^+\mu^-$	$\frac{0}{7999}$	< 0.001

Table 5.2: Estimated background contributions to $e^+e^- \rightarrow \mu^+\mu^-(\gamma)$.

$M_Z = 91.2$ GeV, $M_t = 150$ GeV and $M_H = 100$ GeV. This data set is equivalent to an integrated luminosity of 1.9 pb^{-1}.

Two-photon events

The sample studied was a set of approximately 8000 $e^+e^- \rightarrow \mu^+\mu^-e^+e^-$ events produced by the Vermaseren event generator [61]. As the two photon cross section is relatively large and the full detector simulation is somewhat slow, only events within a restricted region of phase space were processed by `GOPAL`. The phase space limitations imposed were that either one charged particle was generated with $p > 4$ GeV and $|\cos\theta| < 0.95$, or two charged particles were generated in the same angular range having $p > 0.5$ GeV and $\cos\zeta > 0.95$, *i.e.* the two tracks were acolinear by less than 18.2°. The minimum invariant mass of the two-photon system was 0.5 GeV. This sample corresponds to an integrated luminosity of 8.0 pb^{-1}.

The results of the analysis of these large Monte Carlo samples are summarised in table 5.2. This includes the number of simulated events in each channel that were selected by the muon pair analysis cuts, and also the the fraction of background events relative to muon pairs. The only significant background contamination is found to be from $\tau^+\tau^-$ production.

5.5 Forward-backward asymmetry measurement

The forward-backward asymmetry may be measured in several different ways, three of which are used and discussed herein. These methods, which are used to determine the asymmetry at each centre of mass energy in the scan, are:

- simple counting of events in the forward and backward hemispheres,
- performing a χ^2-minimisation fit to the binned differential cross section,
- performing a negative log likelihood fit to the unbinned differential cross section.

It is central to such measurements that the sign of the charge of the muon tracks and the angle, θ, are well determined. In view of this, data taking periods in which essential components of the detector (or trigger) were not fully operational have been excluded.

Detector and trigger status

Each sub-detector supplies two status codes, one for trigger and one for detector, in the range 0–3 where 0 indicates that the status is 'unknown' and 3 that the detector (trigger) is deemed 'fully operational'. As a result of the redundancy present in muon pair detection, it is sufficient to require that each of the vertex chamber, jet chamber and ToF had a detector status of at least 2 and the jet chamber had a trigger status of at least 2.

A measurement of the asymmetry is independent of the absolute normalisation by integrated luminosity and therefore no restrictions are imposed on detector status of the forward detector. These 'status quality' cuts rejected $7.17 \pm 0.08\%$ of non-luminosity events in the 1990 low multiplicity sample.

Charge and θ determination

Only events in which the charge, q, of both muons is well determined can be meaningfully used to measure an asymmetry. All events in which both muon candidates are assigned a charge of the same sign are discarded for the purpose of the asymmetry measurement. The probability of either muon having an incorrect charge assignment can be deduced from a distribution of $\left(\frac{q}{p}\right)_{\mathrm{track1}}$ vs. $\left(\frac{q}{p}\right)_{\mathrm{track2}}$, as shown in figure 5.9. The data is presented as $\left(\frac{q}{p}\right)$ as the curvature measurement in the magnetic field, from which the momentum p is determined, is proportional to $\frac{1}{p}$. This plot therefore illustrates the quantity actually measured by the central

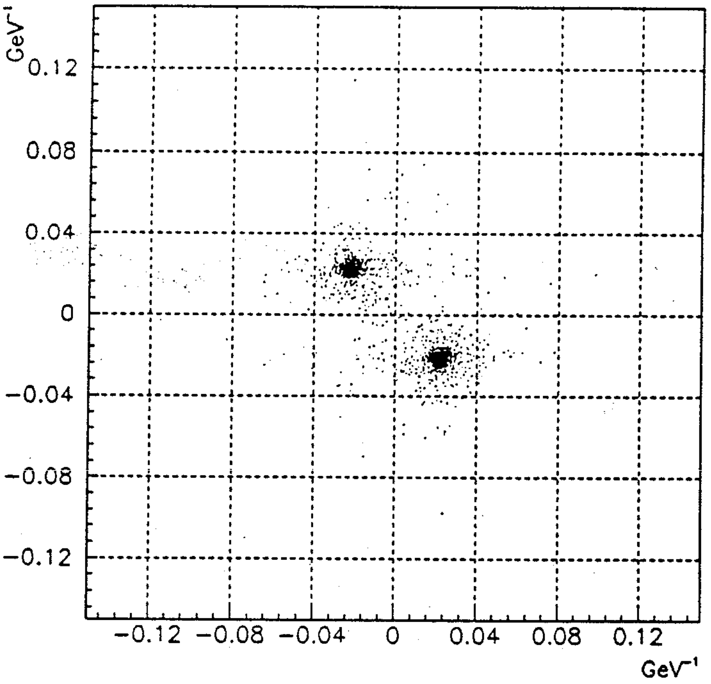

Figure 5.9: Distribution of $\left(\frac{q}{p}\right)_{\text{track1}}$ vs. $\left(\frac{q}{p}\right)_{\text{track2}}$ for muon candidates, showing charge mis-assignments.

detector and that the charge measurement is slightly degraded at higher momenta. This gives an indication of the fraction of events in which the charge on both muons has been wrongly assigned, assuming that the reason for the charge determination problems are not correlated. The probability of the same charge being assigned to both muons in an event is $3.1 \pm 0.2\%$. This gives a double charge mis-assignment probability of $0.1 \pm 0.01\%$ averaged over all $\cos\theta$ considered.

The θ determination of tracks by the central detector is adequate in the barrel region where the z-chambers are present to provide accurate z information of track endpoints. However, in the forward region there is a visible degradation of resolution where all z information is provided by the vertex and jet chambers and an alternative method is employed. The muon endcap information is used wherever it is available and matched to a track and in its absence, the central detector is used.

As muon pair tracks originate from a very small region around the interaction point, an accurate measurement of θ is possible by taking a single point on the muon endcap reference plane and assuming the track has a straight trajectory from the beam crossing point. By using this method, a more reliable measurement of θ can be obtained than from the trajectory of central detector tracks. The high accuracy obtained in this way is a result of the large lever arm for the angular measurement between the interaction point and the muon endcap reference plane, which is approximately 540 cm. The uncertainty on θ determined in this manner is estimated to be less than 2 mrad.

5.5.1 Differential cross section

The use of the improved Born approximation for the differential cross section has been discussed in chapter 4. By solving equations 4.6 and 4.8 to eliminate terms in $C^{(2)}_{\gamma Z}$ and $C^{(2)}_{ZZ}$, the differential cross section can be written in the form

$$\frac{d\sigma}{d\cos\theta} = B(s)\left[(1+\cos^2\theta) + \frac{8}{3}A^0_{\mathrm{FB}}\cos\theta\right], \tag{5.1}$$

where the overall normalisation, $B(s)$, is an s dependent function. Cast in this form, $A^0_{\mathrm{FB}}(s)$ is the coefficient of the only asymmetric part of the differential cross section. This expression is later fitted to the experimentally determined differential cross section at each of seven centre of mass energies to extract observed asymmetries, $A^{\mathrm{obs}}_{\mathrm{FB}}(s)$.

It should be noted that no overall normalisation conditions are imposed upon the data for the asymmetry measurement and all differential cross sections presented herein are expressed in terms of numbers of observed events. Furthermore, from the definition of the asymmetry in equation 4.4, it can be seen that asymmetry measurement by event counting rather than by performing a fit to the shape of the differential cross section will lead to a value for $A^{\mathrm{obs}}_{\mathrm{FB}}(s)$ that must be qualified by the restricted angular range of the acceptance. The results from the fits will be given for both the full solid angle and scaled down by the appropriate factor to simplify comparison with the event counting results.

The measured differential cross section at each centre of mass energy, from which $A_{\mathrm{FB}}(s)$ is determined, is shown in figure 5.10. The error bars are statistical only. A qualitative inspection of these distributions indicates that with increasing centre of mass energy there is a small change in the relative populations of the

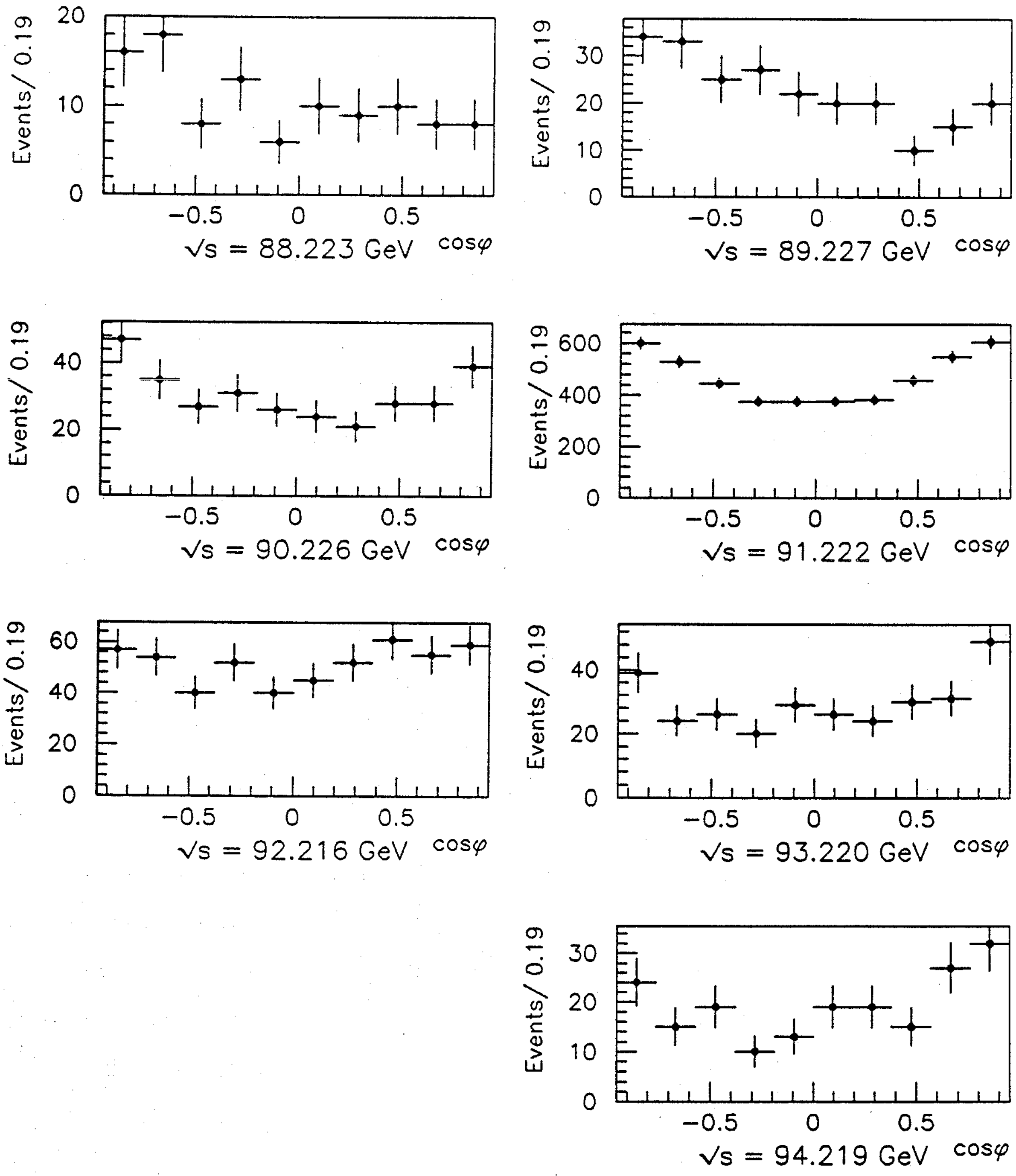

Figure 5.10: Differential cross sections measured at each energy point.

forward and backward hemispheres, with more events in the backward hemisphere at lower energies and more in the forward hemisphere at higher energies. Before measuring the asymmetry, the effect of determining the differential cross section using the OPAL detector is studied.

Bin-by-bin correction

The three methods of measuring the asymmetry can all be considered as using binned data, although the event counting (2 bins) and maximum likelihood fit (infinitessimal bins) are both limiting cases. In order to use experimentally measured data for physics, all effects of the detector should be removed or 'unfolded'. For the total cross section, the main effect to be removed is that of acceptance which may be corrected for by a single numerical factor. In the case of the differential cross section such a correction is effectively required for each individual $\cos\theta$ bin of the distribution. This bin-by-bin correction procedure was performed as below.

A set of 20000 muon pair 4-vectors was generated by the **KORALZ** Monte Carlo with the standard model parameters $M_t = M_H = 100$ GeV and $M_Z = 92.0$ GeV. Initial state radiation ($O(\alpha^2)$ exponentiated) and final state radiation ($O(\alpha)$) were included in the simulation. These 4-vectors were processed by the full detector simulation and reconstruction and analysed in complete analogy with the real data. The differential cross section was evaluated for the original Monte Carlo 4-vectors and for the corresponding events that had been processed by **GOPAL** and **ROPE**, and compared in a 10 bin distribution in the angular range $-0.95 < \cos\theta < 0.95$.

This binning was chosen in order to ensure that the statistical error in the most sparsely populated $\cos\theta$ bin should be less than 3%. By comparison, even close to resonance where most events were detected, the statistical error in each $\cos\theta$ bin for real data is 4–5%: away from the peak the statistical error for real data in each $\cos\theta$ bin is considerably larger, typically 10–20%. Thus with the accumulated Monte Carlo statistics, the uncertainties on any correction factors will be significantly less than the statistical error present in the real data.

Denoting the contents of the i^{th} bin of the 4-vector distribution by $f(\cos\theta_i)$ and that of the fully analysed events by $g(\cos\theta_i)$, the correction factor for this bin is given,

$$C(\cos\theta_i) \equiv \frac{g(\cos\theta_i)}{f(\cos\theta_i)}. \tag{5.2}$$

This set of correction factors, $\{C(\cos\theta_i)\}$, which incorporates detector inefficiencies

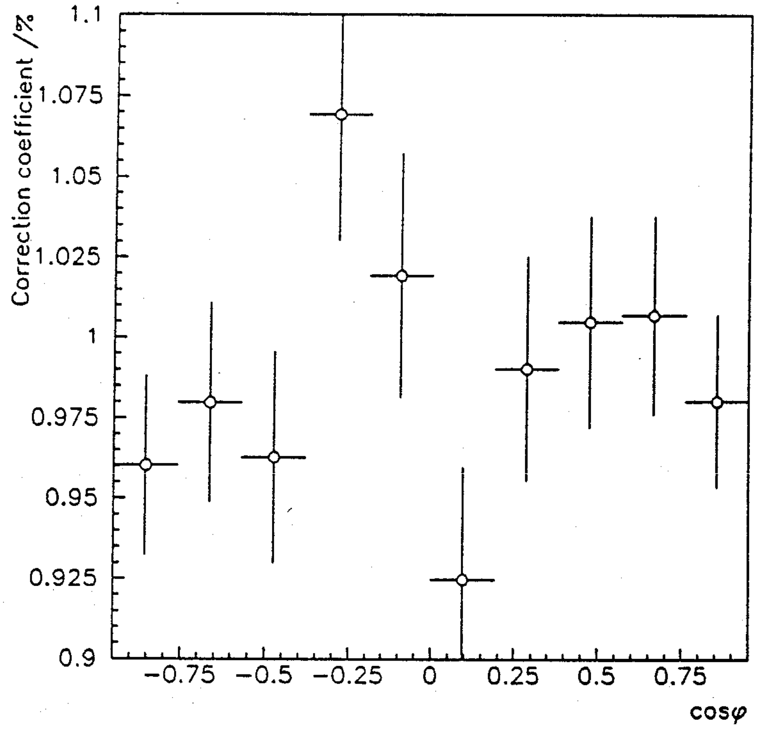

Figure 5.11: Bin-by-bin correction factors to the differential cross section.

and the effects of cuts and acceptance (assuming **GOPAL** is an accurate representation of OPAL), is used to extract the true differential cross section, $\frac{d\sigma}{d\cos\theta}$, from the experimentally observed one, $(\frac{d\sigma}{d\cos\theta})_{\mathrm{obs}}$, by

$$\frac{d\sigma}{d\cos\theta_i} = \left(\frac{d\sigma}{d\cos\theta_i}\right)_{\mathrm{obs}} \times \frac{1}{C(\cos\theta_i)}$$

The correction factors evaluated from this procedure are shown in figure 5.11. A straight line fit to this distribution has a gradient of 0.01 ± 0.02 and an ordinate of 0.99 ± 0.01, with a χ^2 per degree of freedom of 10.2/8. This does not differ significantly from attributing a correction factor of unity in all bins. Thus, no angular dependent correction factor is applied to the differential cross section with the current accumulated data.

Migration effects

The set of correction factors become highly correlated if the bin size used is such that a significant proportion of the events with 4-vectors generated in a given bin migrate into a different bin after the effects of the detector have been simulated. This can be studied on an event-by-event basis as the simulated raw data contains

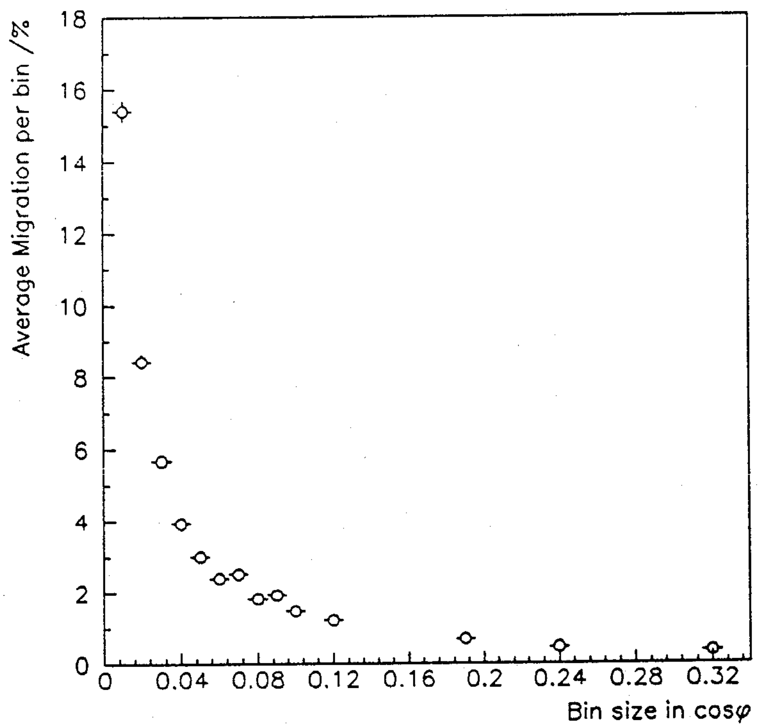

Figure 5.12: Variation in average migration as a function of bin width.

the original 4-vectors in the event record. Migration is larger in the forward region where the θ resolution is worse and smearing from bin to bin is more probable. The percentage of events that migrate, averaged over all bins, as a function of the bin size is presented in figure 5.12.

The bin sizes used for the asymmetry determination by event counting (bin width = 0.95) and to study the effects of the detector on the measured angular distribution (bin width = 0.19) are both sufficiently large that migration effects are negligible. Having shown that migration effects and the angular dependence of the detector are not significant for the measurements in hand, the three methods of asymmetry determination are now described.

5.5.2 $A_{\mathrm{FB}}^{\mathrm{obs}}(s)$ by event counting

This is the most straightforward method of measuring the asymmetry and is independent of the detailed form of the θ dependence of the acceptance, except in the region close to the boundary between the forward and backward hemispheres. The measurement follows directly from the definition of the asymmetry in equation 4.4 and is given

$$A_{\rm FB}^{\rm obs}(s) = \frac{N_F - N_B}{N_F + N_B}, \qquad \sigma_{A_{\rm FB}^{\rm obs}(s)} \simeq \frac{2}{N_F + N_B}\sqrt{\frac{N_F N_B}{N_F + N_B}}$$

where N_F and N_B are the number of events in the forward and backward hemispheres respectively and $\sigma_{A_{\rm FB}^{\rm obs}(s)}$ is the (binomial) error on $A_{\rm FB}^{\rm obs}(s)$. The effect of events migrating between hemispheres due to the finite angular resolution has been shown to be negligible above. The measured asymmetries for each centre of mass energy are presented in table 5.3

5.5.3 $A_{\rm FB}^{\rm obs}(s)$ from χ^2-minimisation fit

The differential cross section is fitted at each centre of mass energy using the CERN minimisation package `MINUIT` [62], to extract the asymmetry. The form of $\frac{d\sigma}{d\cos\theta}$ used in the fit is that given in equation 5.1, where $B(s)$ and $A_{\rm FB}^{\rm obs}(s)$ are treated as free parameters. The procedure is to minimise a χ^2 function which, assuming correlations between different $\cos\theta$ bins is negligible, is given by

$$\chi^2 = \sum_{j=1}^{N_{\rm bins}} \frac{\left(N_j - \frac{d\sigma}{d\cos\theta_i}\right)^2}{N_j},$$

where N_j and $\frac{d\sigma}{d\cos\theta_i}$ are respectively the number of observed muon candidates and the differential cross section (expressed in terms of numbers of events) in the $j^{\rm th}$ $\cos\theta$ bin.

The number of $\cos\theta$ bins into which the data was accumulated, $N_{\rm bins}$, was varied between 5 and 11 and fits were performed at each centre of mass energy with the different binning. In no case did the fitted asymmetry at a given centre of mass energy vary by more than half a standard deviation with this range in binning. The results of the fits should all be equally meaningful and an arbitrary decision to use distributions with 10 bins was made. The differential cross sections and the corresponding fitted curves for each of the seven centre of mass energies used are shown in figure 5.13. The numerical results of these fits are presented in table 5.4.

$\sqrt{s}$ (GeV)	N_F	N_B	$A_{\mathrm{FB}}^{\mathrm{obs}}(s)$
88.223	45	61	-0.151 ± 0.096
89.227	85	141	-0.248 ± 0.064
90.226	140	166	-0.085 ± 0.057
91.222	2372	2326	+0.010 ± 0.015
92.216	272	243	+0.056 ± 0.044
93.220	160	138	+0.074 ± 0.058
94.219	112	81	+0.161 ± 0.071

Table 5.3: Measured asymmetry by counting events within $|\cos\theta| < 0.95$.

$\sqrt{s}$ (GeV)	$A_{\mathrm{FB}}^{\mathrm{obs}}(s)$ $\lvert\cos\theta\rvert < 1.0$	$A_{\mathrm{FB}}^{\mathrm{obs}}(s)$ $\lvert\cos\theta\rvert < 0.95$	χ^2 / DF
88.223	-0.195 ± 0.091	-0.190 ± 0.089	6.3/8
89.227	-0.280 ± 0.059	-0.272 ± 0.058	7.5/8
90.226	-0.076 ± 0.055	-0.074 ± 0.053	2.5/8
91.222	+0.010 ± 0.014	+0.009 ± 0.014	4.6/8
92.216	+0.045 ± 0.041	+0.044 ± 0.040	10.9/8
93.220	+0.091 ± 0.055	+0.088 ± 0.054	5.4/8
94.219	+0.141 ± 0.070	+0.137 ± 0.068	6.7/8

Table 5.4: Measured asymmetry by χ^2-minimisation fit.

$\sqrt{s}$ (GeV)	$A_{\mathrm{FB}}^{\mathrm{obs}}(s)$ $\lvert\cos\theta\rvert < 1.0$	$A_{\mathrm{FB}}^{\mathrm{obs}}(s)$ $\lvert\cos\theta\rvert < 0.95$
88.223	-0.194 ± 0.093	-0.189 ± 0.090
89.227	-0.273 ± 0.062	-0.266 ± 0.060
90.226	-0.073 ± 0.055	-0.071 ± 0.053
91.222	+0.010 ± 0.014	+0.010 ± 0.014
92.216	+0.054 ± 0.043	+0.052 ± 0.042
93.220	+0.086 ± 0.056	+0.084 ± 0.054
94.219	+0.132 ± 0.067	+0.128 ± 0.066

Table 5.5: Measured asymmetry by maximum likelihood fit.

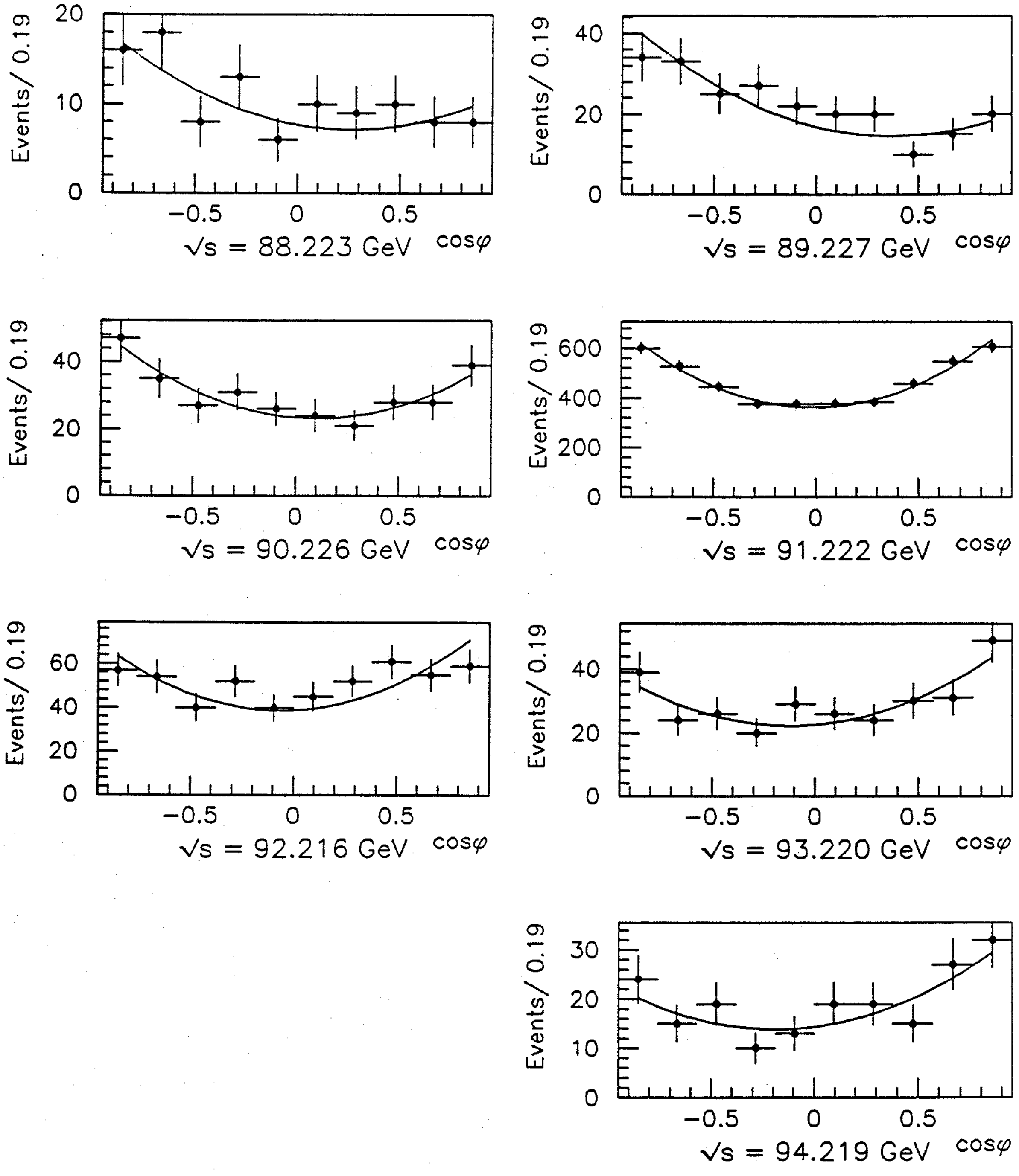

Figure 5.13: χ^2-fit to the measured differential cross section at each energy point.

5.5.4 $A_{\mathrm{FB}}^{\mathrm{obs}}(s)$ from maximum likelihood fit

The same fitting package and strategy are used as for the previous fit, the vital difference being that a negative log likelihood function is minimised instead of a χ^2 function and the data is not binned (after [20]). The function to be minimised is given by

$$W = -\sum_{j=1}^{N_{\mathrm{obs}}} \ln(1 + \cos^2\theta + \frac{8}{3}A_{\mathrm{FB}}^{\mathrm{obs}}(s)\cos\theta),$$

where the summation extends over the N_{obs} observed events. As the measured asymmetry occurs in this function in the form of the logarithm of a product with $\cos\theta$, $A_{\mathrm{FB}}^{\mathrm{obs}}(s)$ has the very desirable property of being independent of any explicit $\cos\theta$ dependence in the acceptance.

The results of the fits at each energy are summarised in table 5.5.

5.5.5 Measured asymmetries

The three different methods of measuring the asymmetry considered above have been found to give results that are entirely consistent with each other in all cases. This further reinforces the observation that to a good approximation any $\cos\theta$ dependence of the acceptance that may exist can be safely neglected at the current level of precision. In subsequent fits to extract more fundamental parameters such as couplings, the asymmetries determined by the maximum likelihood approach will be used in preference to the other methods. As the agreement between the two fitting methods is so good, the only justification for using the maximum likelihood results is the *a priori* lack of explicit θ dependence inherent in this procedure.

5.6 Muon pair cross section measurement

The experimentally measured cross section is defined as,

$$\sigma_{\mu\mu}(s) \equiv \frac{N_{\mu\mu}}{\int \mathcal{L}\, dt}, \tag{5.3}$$

where $\int \mathcal{L}\, dt$ is the integrated luminosity and $N_{\mu\mu}$ is the number of muon pair events produced for a given integrated luminosity. $N_{\mu\mu}$ is calculated from the observed number of muon pair events, $N_{\mu\mu}^{\mathrm{obs}}$, by correcting for events lost due to imperfections in the detector and selection procedure, for the acceptance being less than 4π and for background contamination.

These different sources of inefficiency are combined into an overall correction factor, F_{corr}, such that

$$\begin{aligned} N_{\mu\mu} &= F_{\mathrm{corr}} \times N_{\mu\mu}^{\mathrm{obs}}, \\ F_{\mathrm{corr}} &\equiv \frac{P}{\epsilon_{\mathrm{trigger}}\epsilon_{\mathrm{filter}}\mathrm{A}_{4\pi}\epsilon_{\mathrm{simulation}}}, \end{aligned}$$

where $\epsilon_{\mathrm{trigger}}$ and $\epsilon_{\mathrm{filter}}$ are respectively the efficiencies of the trigger and filter, $\mathrm{A}_{4\pi}$ is the acceptance of the detector (evaluated using `GOPAL`), $\epsilon_{\mathrm{simulation}}$ is a factor to compensate for losses arising from effects present in actual data that are not included in the simulation, such as tracking problems in particular regions of the jet chamber, and P is the overall purity of the selection procedure.

The purity is defined as $\frac{N_{\mu\mu}}{N_{\mu\mu}+N_{\mathrm{bg}}}$, with N_{bg} the number of background events in the sample that have survived the muon pair selection cuts. It has been illustrated in section 5.4 that the only significant background is from $\tau^+\tau^-$ events, *i.e.* $N_{\mathrm{bg}} = N_{\tau\tau}$. By assuming that the production cross sections for $\tau^+\tau^-$ and $\mu^+\mu^-$ are equal, the purity depends entirely upon the ratio $\frac{N_{\mu\mu}}{N_{\tau\tau}}$. Using the results from Monte Carlo studies in table 5.2 to determine $\frac{N_{\tau\tau}}{N_{\mu\mu}}$, the purity is found to be $P = 0.989 \pm 0.001$, where the error is from the statistics of the simulated data samples.

5.6.1 Acceptance correction

The overall acceptance of the detector, $\mathrm{A}_{4\pi}$, is the largest single contribution to F_{corr}. It is evaluated by using the `KORALZ` data set described above and following the same procedure as used to determine background contamination. A total of 18309 events out of a generated sample of 20000 were classified as muon pair candidates. This is leads to an acceptance measurement of $\mathrm{A}_{4\pi} = 0.915 \pm 0.002$, where the quoted error is statistical only. The energy variation of the acceptance was studied using event samples at the 4-vector level and is estimated to be less than 0.5% over the range of the energy scan.

This was evaluated by generating 16 samples of 4-vectors, each consisting of

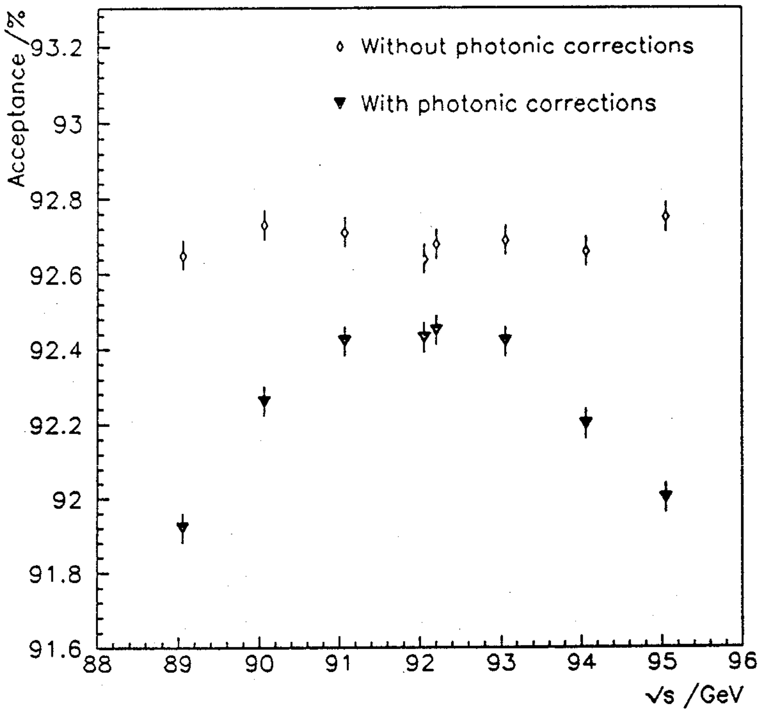

Figure 5.14: Energy dependence for $\mu^+\mu^-(\gamma)$ events.

half a million KORALZ events. Eight of these samples were generated without any photonic corrections in either the initial or final states, whilst the remaining event samples were generated with second order exponentiated initial state radiation and first order final state radiation. The standard model input to the simulation was $M_Z = 92.0$ GeV and $M_H = M_t = 100$ GeV. The centre of mass energies were chosen to have approximately the same $\sqrt{s} - M_Z$ as in the actual data, assuming $M_Z = 91.174$ GeV from [20]

Only a very simplistic definition of acceptance was used, *viz.* two muons were required be within $|\cos\theta| < 0.95$: no cuts on the momentum or acolinearity of the muons were made. The results of this study are shown in figure 5.14. It can be seen from the figure that in the absence of photonic effects, the acceptance has negligible energy dependence and is also equal to the lowest order expectation of approximately 92.7%. (This is obtained by integrating the standard model angular distribution of $(1 + \cos^2\theta)$ within $|\cos\theta| < 0.95$ and comparing it with the same distribution integrated over the full solid angle.) In the presence of photonic radiation, the acceptance does vary with the centre of mass energy, but only by a

Source of inefficiency	numerical value
Trigger efficiency, $\epsilon_{\mathrm{trigger}}$	0.998 ± 0.002
Filter efficiency, $\epsilon_{\mathrm{filter}}$	1.000
Acceptance, $A_{4\pi}$	0.915 ± 0.002
Monte Carlo imperfections, $\epsilon_{\mathrm{simulation}}$	0.991 ± 0.008
Purity of selection procedure, P	0.989 ± 0.001
Overall correction factor, F_{corr}	1.093 ± 0.009

Table 5.6: Contributions to correction factor, F_{corr}, and systematic error.

relatively small amount compared to the statistical error on the measured data.

5.6.2 Sources of systematic error

By its very nature, the overall correction factor to the cross section, F_{corr}, is a source of systematic error. The errors associated with several of the quantities that define F_{corr} are unchanged from previous work [20], whereas the estimates of P and $A_{4\pi}$ and the associated uncertainties have been re-evaluated. Systematic discrepancies between `GOPAL` and the detector itself are incorporated into F_{corr} through the factor $\epsilon_{\mathrm{simulation}}$. Numerical values for all constituents of the global correction factor and errors are given in table 5.6. With the contributory factors considered, the resultant overall correction is estimated to be $F_{\mathrm{corr}} = 1.093 \pm 0.009$ (systematic).

A further source of systematic error for cross section measurements is the measurement of the luminosity. This has been extensively described elsewhere [20,63,64] and it is sufficient to note herein that the total systematic error on luminosity measurements in 1990 has been estimated to be 1.0%. This is larger than the statistical error present in luminosity measurements, arising from the number of small angle scattered Bhabha events recorded in the forward detector, which is typically 0.5% in a given energy bin with the integrated luminosity accumulated per bin. In addition, there is a systematic uncertainty on the overall LEP energy scale of ±24 MeV.

$\sqrt{s}$ (GeV)	$\int \mathcal{L}\,dt$ (nb^{-1})	$N^{obs}_{\mu\mu}$	$\sigma_{\mu\mu}$ (nb)
88.223	479.6 ± 3.2	109	0.248 ± 0.024
89.227	597.1 ± 3.6	231	0.423 ± 0.028
90.226	404.7 ± 3.0	317	0.856 ± 0.048
91.222	3519.6 ± 9.0	4834	1.501 ± 0.022
92.216	524.4 ± 3.5	530	1.105 ± 0.049
93.220	558.7 ± 3.7	307	0.601 ± 0.035
94.219	548.7 ± 3.7	202	0.402 ± 0.028
Total	6633 ± 12	6530	

Table 5.7: Measured muon pair production cross sections, corrected for inefficiency and acceptance.

5.6.3 Measured cross sections

The muon pair cross section is evaluated according to equation 5.3 in each of seven energy bins. Each bin combines data from several energy points with slightly differing centre of mass energies (the typical variation in centre of mass energy is less than 7 MeV), the central energy value for a bin being determined by weighting the different energies according to their respective integrated luminosity. The final cross section in each bin is presented in table 5.7, together with the (uncorrected) number of muon pair events and the integrated luminosity. The errors on the luminosities and the cross section are statistical only.

5.7 $\mu\mu\gamma$ (colinear γ) cross section measurements

This section describes a study of the $\mu^+\mu^-\gamma$ final state for the case where photons and muons are colinear. Three measurements are presented, *viz.*

1. the differential cross section with respect to energy of the colinear photons, $\frac{dN}{dx_\alpha}$,
2. the total cross section for the process, $\sigma_\alpha(\mu^+\mu^-\gamma)$,
3. the cross section for this process relative to the muon pair cross section with inclusive photons, $\frac{\sigma_\alpha(\mu^+\mu^-\gamma)}{\sigma(\mu^+\mu^-(\gamma))}$.

These measurements depend upon two parameters. The first of these, α, is the half angle of a three dimensional cone around each muon and photons within such a cone are defined to be colinear with the muon in question. The second parameter, x_α^{min}, is a lower bound on the colinear photon energy divided by the beam energy, x_α. This is used during the integration of the differential cross section at each centre of mass energy in order to obtain the total cross section as a function of $\sqrt{s}$. By defining the differential cross section in terms of the scaled photon energy, x_α, the same x_α^{min} can be used at all points in the scan.

In the detector, the energy of colinear photons is obtained by summing the energy of all ECAL clusters within a fixed α cone around each muon candidate in an event. The experimental measurement is complicated by the fact that muons themselves deposit a small amount of energy in the ECAL, E_{mip}, which is approximately 600 MeV per muon. A further complication is presented by the production of bremsstrahlung photons as the muons travel through the material of the detector. This latter effect is corrected for using the detector simulation in order to obtain a physical measurement that is independent of the particular hardware configuration of which OPAL is composed.

In order to establish that the behaviour of these clusters is well understood, a comparison is made between the candidate muon pair events and Monte Carlo. It is essential that the Monte Carlo is capable of reproducing distributions observed in the real data before it may be used to correct the data. Having done this, the parameters α and x_α^{min} are fixed, the treatment of the E_{mip} contribution to the ECAL energy is quantified and finally the three physical quantities above are measured.

5.7.1 Comparison with Monte Carlo

The muon pair candidates used herein are as for the inclusive $\mu^+\mu^-(\gamma)$ cross section measurements. These are compared with the same sample of 20000 Monte Carlo muon pair events (including detector simulation) that have been used above to determine the acceptance for $\mu^+\mu^-(\gamma)$ events. It should be noted that although these events have a thorough second order (exponentiated) treatment of initial

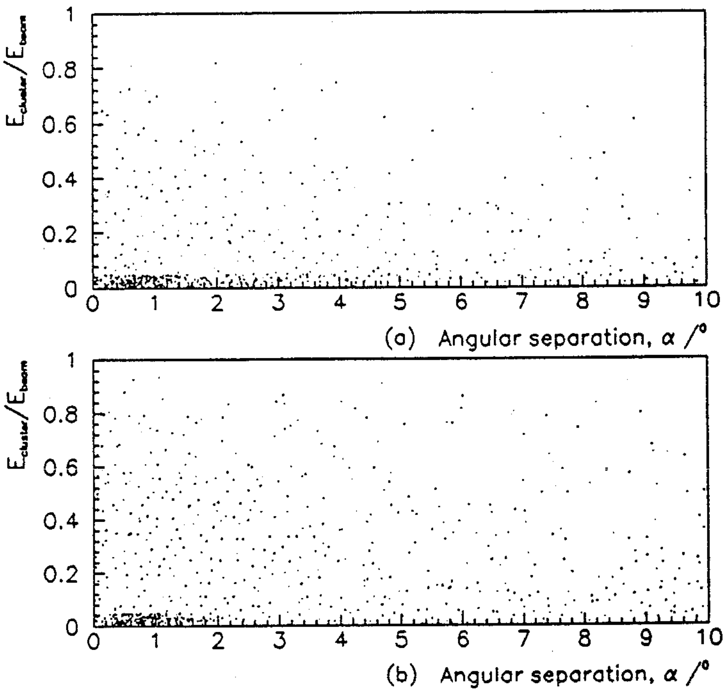

Key
(a) 1990 OPAL muon candidates (b) Monte Carlo

Figure 5.15: Energy flow around muon candidates.

state radiation, they only allow for single (unexponentiated) photon production in the final state. The most relevant quantities to compare are the electromagnetic energy flow around muon candidates, the total electromagnetic energy colinear with muons and the differential cross section.

Energy flow around muons

The energy flow is defined as the distribution of ECAL cluster energies as a function of their angular separation, α, from a muon track, where the cluster energies are expressed in terms of x_α. This is shown in figure 5.15. There are approximately three times as many Monte Carlo events as real muon candidates in this figure. It is apparent that a higher proportion of low energy ECAL clusters are very close to charged tracks (within 2°) in Monte Carlo than in real data. The fact that the θ resolution of the central detector is better in the simulation than the real detector contributes to the discrepancy.

However, there is a relatively good agreement on the fraction of all clusters

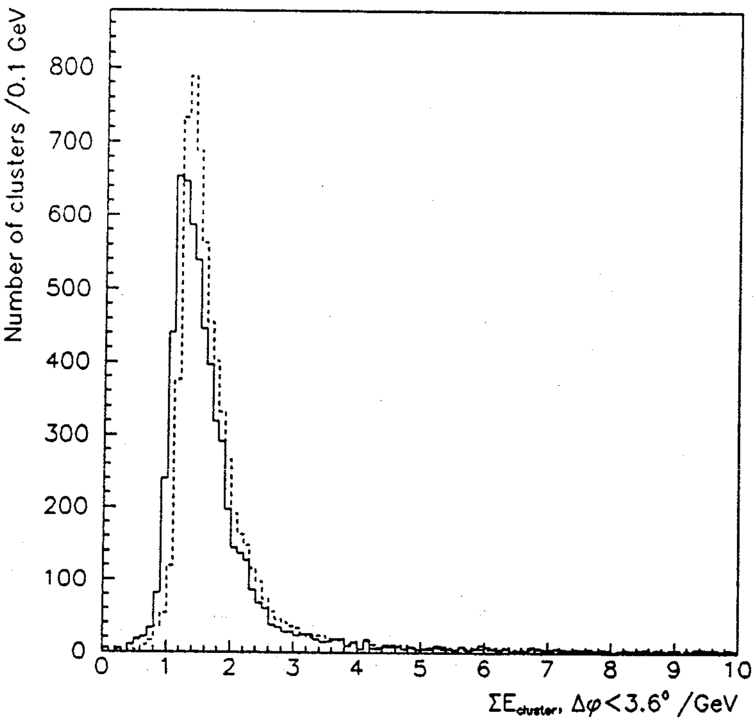

Key
Solid histogram: observed muon candidates
Dashed histogram: Monte Carlo prediction

Figure 5.16: Summed ECAL energy in a cone of half angle 200 mrad in r-ϕ.

within 10° of a muon candidate (92.4 ± 0.2% and 93.4 ± 0.2% for real data and Monte Carlo respectively). given that residual noise clusters in the ECAL which remain after all 'hot' clusters have been removed is estimated to be of order 0.5%.

Total colinear electromagnetic energy

Energy is summed in a cone of half angle 200 mrad in the r-ϕ plane around each muon candidate and the distribution of this quantity for real and Monte Carlo events is presented in figure 5.16. where the simulated data has been normalised to the number of real muon candidates. By using a more inclusive quantity such as the sum of all ECAL cluster energies around a muon, a good overall agreement is obtained between Monte Carlo and real data although the peak positions are shifted by 1 bin (50 MeV) and the sum of real ECAL energies is slightly broader.

The sum of ECAL clusters in r-ϕ is used to illustrate this agreement as this quantity is used in the definition of muon candidates in the absence of muon

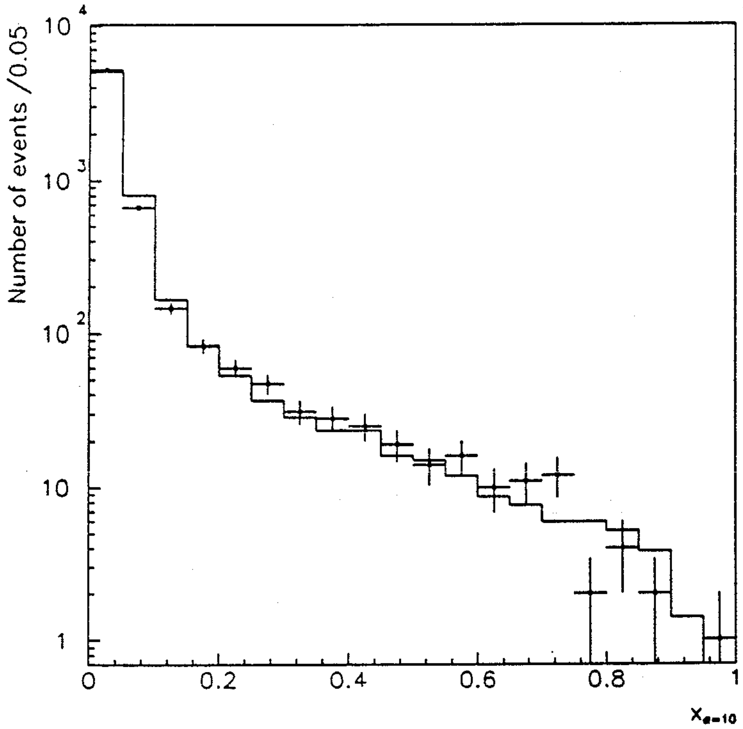

Key

Data points: observed muon candidates
Solid histogram: Monte Carlo prediction

Figure 5.17: Differential cross section, before E_{mip} subtraction.

chamber and HCAL information associated to a charged track. Muons identified in this way are constrained to have less than 3 GeV of associated ECAL energy and so will not make a large contribution to the measured colinear cross sections. However, these events constitute less than 4% of all muon candidates and the losses can be corrected for using the simulation of the detector.

Differential cross section

The differential cross section for real data and Monte Carlo are compared in figure 5.17 (note logarithmic scale). The simulated data has been normalised to the total number of real muon candidates. For clarity, the Monte Carlo data is presented as a solid profile, despite the fact that the statistical error in each bin is approximately 60% of the corresponding error for real data.

In these spectra, colinearity is defined by $\alpha = 10°$. Both $\frac{dN}{dx_{10}}$ distributions contain a contribution to the ECAL energy sum from the minimum ionising energy of the muons, although most events in which the only electromagnetic clusters are of this origin will be contained in the first bin, *i.e.* $x_\alpha < 0.05$, which is equivalent to 2.3 GeV on peak. The agreement between the simulation and the observed data is good, even in the large x_α region.

5.7.2 Choice of parameter values

The differential cross section must always be qualified by the value of α used in carrying out the measurement, whilst the total and relative cross sections must additionally specify the appropriate value of x_α^{min}. Each of the three measurements (differential, total and relative cross sections) requires that the minimum ionising energy be removed from the differential cross section. The simple criteria used to select appropriate values for the two parameters, and the treatment of the minimum ionising signal are summarised below.

Colinearity half angle, α

This is set to 10°. In order to study the effect of the choice of α upon the measured differential cross section, half a million muon pair events including initial and final state radiation were generated at 4-vector level. The value of $\sqrt{s} - M_Z$ in this event generation was +0.2 GeV. The calculated differential cross section for various values of α is shown in figure 5.18. The $\alpha = 10°$ curve is a compromise, being sufficiently large that the measured differential cross section is insensitive to small variations in α, without being so large that it amounts to defining all photons in a given event as being colinear with either muon, *i.e.* $\alpha = 90°$.

It is important that the differential cross section is not critically dependent upon the choice of α due to the finite angular resolution of the detector and to allow for a distortion in the definition of the cone at small polar angles. This affects the cone at the edge of the acceptance.

Minimum colinear photon energy, x_α^{min}

A further half a million events were generated without the simulation of final state radiation. The differential cross section for these events for various values

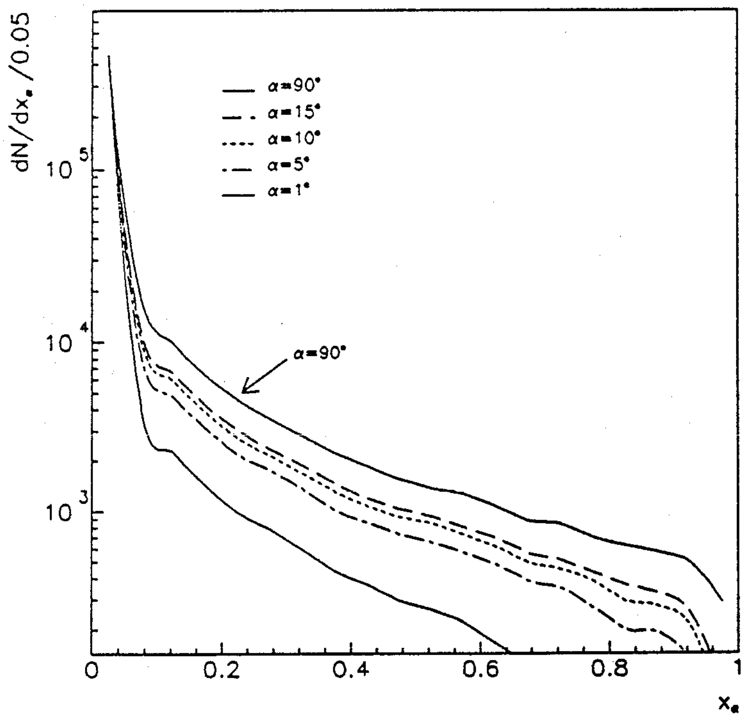

Figure 5.18: Differential cross section with initial and final state radiation, for various values of α.

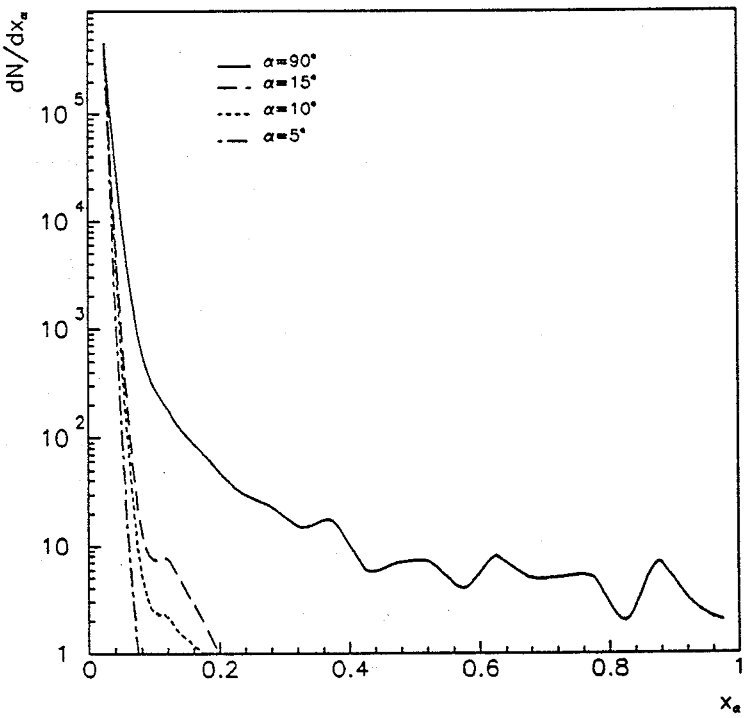

Figure 5.19: Differential cross section with initial state radiation alone, for various values of α.

of α is shown in figure 5.19. This figure is for illustration only, hence curves are used rather than points with error bars, despite very limited statistics in the larger x_α bins. In contrast to the previous figure, most events do not contain significant amounts of colinear photonic energy. Thus, by choosing x_{10}^{min} =0.05 a large fraction (~ 10%) of all of the events generated with final state radiation (shown in figure 5.18) are selected whilst almost all of the events generated without final state radiation (shown in figure 5.19) are rejected. To increase x_{10}^{min} to 0.10 would reject a further 35% of remaining events, which is deemed unacceptable given the limited number of real muon candidate events.

Minimum ionising energy, E_{mip}

The minimum ionising energy for any given muon candidate, E_{mip}, is sampled from a distribution of energies and therefore cannot be strictly subtracted on an event by event basis. However, as this distribution is expected to be narrow compared to the binning used in the differential cross section, a fixed value of E_{mip} is subtracted from each muon with a non-zero colinear electromagnetic energy. (The half width of the distributions in figure 5.16, which contain both colinear photonic energy and the minimum ionising signal, are 170 MeV whereas the differential cross is binned in divisions of approximately 2.3 GeV on peak.) The result is that every event has either E_{mip} or $2E_{\mathrm{mip}}$ subtracted; any events with a colinear energy numerically less than zero after this subtraction are rejected.

In order to assess the effect of this procedure, the value of E_{mip} used was varied in the range from 400 MeV to 800 MeV in steps of 50 MeV for real and simulated data. The relative proportion of events rejected in the real data and the simulated data by the E_{mip} subtraction procedure varied with changes in E_{mip}, as expected from the summed energy distributions shown in figure 5.16. The value chosen was $E_{\mathrm{mip}} = 600$ MeV. The total and relative colinear photon cross section measurements, in which only events containing more than x_{10}^{min} photonic energy are used, are found to be relatively insensitive to the precise value chosen for E_{mip}. Variations in E_{mip} by ±50 MeV around a central value of 600 MeV change the total colinear cross section by ±2.8% whilst even very large changes in E_{mip} of

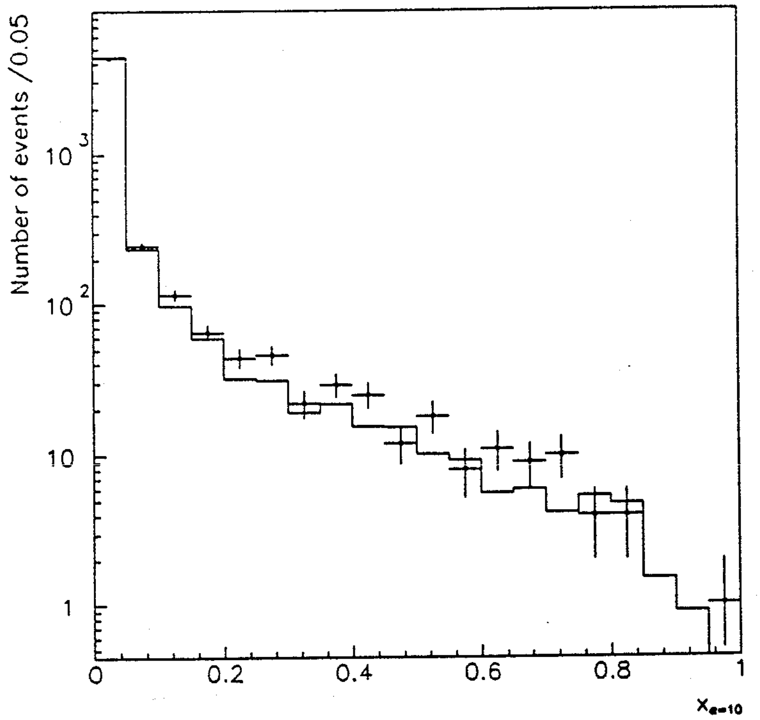

Key
Data points: observed muon candidates
Solid histogram: Monte Carlo prediction

Figure 5.20: Differential (colinear γs) cross section $\frac{dN}{dx_{10}}$.

±200 MeV only modify the total colinear cross section by ±11%.

5.7.3 Measured colinear photon cross sections

With $\alpha = 10^\circ$, $x_{10}^{\text{min}} = 0.05$ and a straightforward method defined with which to treat the minimum ionising energy deposit, the proposed measurements are performed. To a good approximation, the acceptance for colinear $\mu^+\mu^-\gamma$ events is the same as that for $\mu^+\mu^-(\gamma)$, the most probable origin for a discrepancy being the imposition of a harsh cut in acolinearity or acoplanarity of the muon pair, or a cut in the maximum ECAL energy in a muon pair event. No acolinearity cut has been used throughout the analysis and the only restriction on acoplanarity made is that the two muon track candidates have an acoplanarity such that $\cos\xi > -0.95$. The application of a cut on the ECAL energy is discussed below.

In the absence of muon chamber or HCAL information, some charged tracks are identified as muon candidates on the basis of the total associated ECAL energy

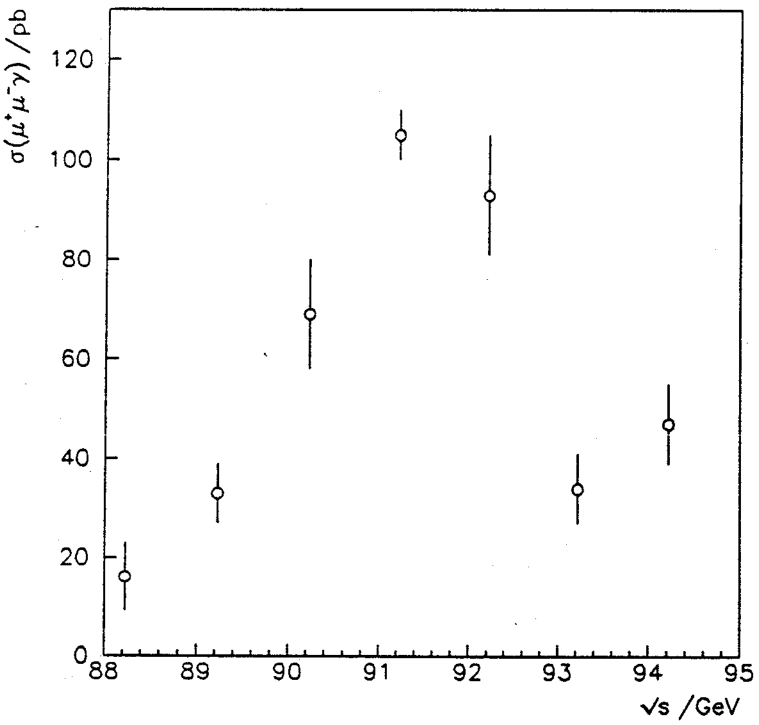

Figure 5.21: Total observed cross section, $\sigma_{10}(\mu^+\mu^-\gamma)$.

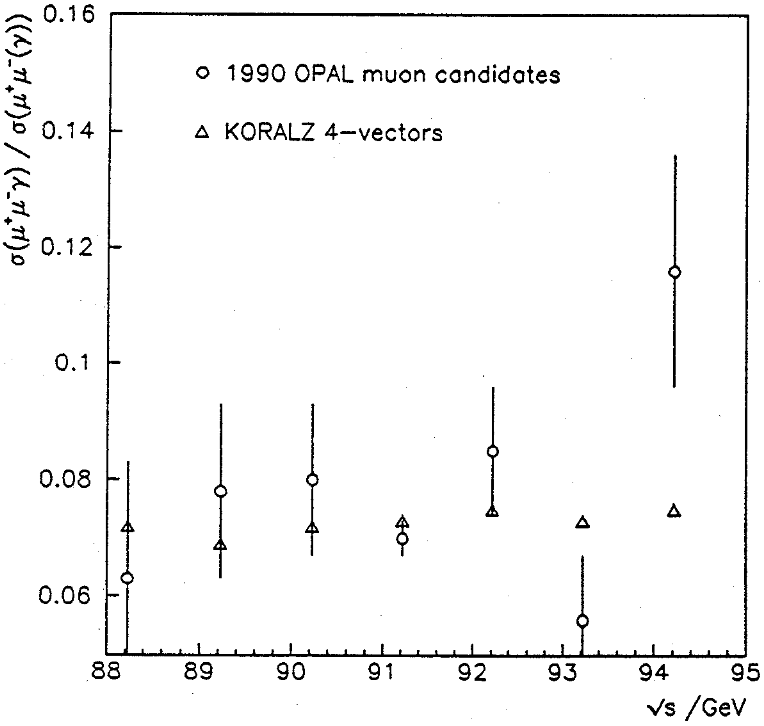

Figure 5.22: Relative cross section, $\frac{\sigma_{10}(\mu^+\mu^-\gamma)}{\sigma(\mu^+\mu^-(\gamma))}$.

(as defined in figure 5.16) being less than 3.0 GeV. Muon candidates identified by this method alone represent 3.8 ± 0.1% of the total number of recorded $\mu^+\mu^-(\gamma)$ events. By studying muons identified using the HCAL and muon chambers, 10.3 ± 0.2% of $\mu^+\mu^-(\gamma)$ events would be expected to fail this ECAL cut. The total loss of $\mu^+\mu^-\gamma$ events from this source is therefore estimated to be 0.4 ± 0.01%. There is very good agreement between Monte Carlo and real data on the value of this inefficiency. It is part of the overall correction to the cross sections which is described below.

Differential cross section

The differential cross section with respect to the colinear γ energy, $\frac{dN}{dx_{10}}$, is shown in figure 5.20 for the observed muon candidates and Monte Carlo data including detector simulation. The simulated data has been normalised to the real data. A good agreement is seen between the distributions. It has been illustrated above that with the chosen values of α and $x_\alpha^{\min}$ most of the initial state radiation has been excluded from this (and subsequent) distributions. However, bremsstrahlung radiation produced during the passage of the muons through the detector will also contribute to the colinear cross section.

In principle it is possible to correct for bremsstrahlung contributing to the measured colinear γ cross section by comparing a Monte Carlo sample of 4-vectors with the results of the detector simulation. In the case of the differential cross section this is not performed due to the relatively limited Monte Carlo statistics of the event sample with the full detector simulation. However, the correction is applied to the total and relative cross section measurements and is described below.

Correction factors for total and relative cross sections

The correction factor for the total colinear γ cross section C_{Tot}, is defined in analogy with equation 5.2 as,

$$C_{\mathrm{Tot}} \equiv \frac{\sigma_{\mu^+\mu^-\gamma}(\mathrm{GOPAL})}{\sigma_{\mu^+\mu^-\gamma}(\text{4-vector})} \tag{5.4}$$

Data sample	`GOPAL`	4-vectors
Events generated	20000	50000
$N_{\mu^+\mu^-\gamma}$, $\lvert\cos\theta\rvert < 0.95$	1931	3369
$N_{\mu^+\mu^-(\gamma)}$, $\lvert\cos\theta\rvert < 0.95$	18309	46260
C_{Tot}	1.33 ± 0.04	
C_{Rel}	1.45 ± 0.04	

Table 5.8: Correction factors for $\mu^+\mu^-\gamma$ cross sections (errors are statistical)

where $\sigma_{\mu^+\mu^-\gamma}$(GOPAL) and $\sigma_{\mu^+\mu^-\gamma}$(4-vector) are the total cross sections determined using `GOPAL` and the 4-vector simulation respectively. This C_{Tot} appears in the expression for the total measured cross section as

$$\sigma_{10}(\mu^+\mu^-\gamma) \equiv \frac{N^{\mathrm{obs}}_{\mu^+\mu^-\gamma}}{C_{\mathrm{Tot}} \int \mathcal{L}\, dt}.$$

In the same way, the correction factor for the relative cross section is given by,

$$C_{\mathrm{Rel}} \equiv \frac{\sigma_{\mu^+\mu^-\gamma}(\mathrm{GOPAL})/\sigma_{\mu^+\mu^-(\gamma)}(\mathrm{GOPAL})}{\sigma_{\mu^+\mu^-\gamma}(\text{4-vector})/\sigma_{\mu^+\mu^-(\gamma)}(\text{4-vector})} \tag{5.5}$$

and is incorporated into the relative cross section by

$$\frac{\sigma_{10}(\mu^+\mu^-\gamma)}{\sigma(\mu^+\mu^-(\gamma))} \equiv \frac{N^{\mathrm{obs}}_{\mu^+\mu^-\gamma}}{C_{\mathrm{Rel}} N^{\mathrm{obs}}_{\mu^+\mu^-(\gamma)}}. \tag{5.6}$$

As the same generator and standard model input was used for the events processed by the detector simulation as for the pure 4-vector events, relative normalisations are used in equations 5.4 and 5.5, *i.e.* C_{Tot} and C_{Rel} are calculated in terms of numbers of events rather than in nb.

In the case of the total cross section, the correction factor must be multiplied by an additional factor to allow for the loss of events between $0.95 < |\cos\theta| < 1.0$, trigger efficiency, imperfections in the detector simulation and the selection purity. The correction from the events lost at small $\cos\theta$ is given by the fraction of all 4-vector events generated that are within $|\cos\theta| < 0.95$, *i.e.* 0.925 ± 0.001. The remaining three corrections are taken from table 5.6 and give a combined factor of 1.000 ± 0.008 (systematic). The final correction factors and the numbers of events generated to calculate them are given in table 5.8. No energy dependence is attributed to these correction factors.

$\sqrt{s}$ (GeV)	$\int \mathcal{L}\,dt$ (nb^{-1})	$N^{obs}_{\mu^+\mu^-\gamma}$	$\sigma_{10}(\mu^+\mu^-\gamma)$ (pb)	$\frac{\sigma_{10}(\mu^+\mu^-\gamma)}{\sigma(\mu^+\mu^-(\gamma))}$
88.223	479.6 ± 3.2	10	16 ± 5	0.063 ± 0.020
89.227	597.1 ± 3.6	26	33 ± 6	0.078 ± 0.015
90.226	404.7 ± 3.0	37	69 ± 11	0.080 ± 0.013
91.222	3519.6 ± 9.0	492	105 ± 5	0.070 ± 0.003
92.216	524.4 ± 3.5	65	93 ± 12	0.085 ± 0.011
93.220	558.7 ± 3.7	25	34 ± 7	0.056 ± 0.011
94.219	548.7 ± 3.7	34	47 ± 8	0.116 ± 0.020
Total	6633 ± 12	689		

Table 5.9: Measured absolute and relative $\mu^+\mu^-\gamma$ (colinear γs) cross sections.

Total cross section

The total cross section for the process, $\sigma_{10}(\mu^+\mu^-\gamma)$, after this correction for acceptance and efficiency has been made is presented in figure 5.21. The numerical values at each centre of mass energy are given in table 5.9. The measured cross sections have a 3% systematic error from the correction factor, C_{Tot} and 1% systematic error from the luminosity determination. The data exhibits resonant behaviour with a peak value in the region of 91.5 GeV (by inspection). To simplify the comparison with Monte Carlo, the cross section for this process relative to the inclusive $\mu^+\mu^-(\gamma)$ cross is used, as described below.

Relative cross section

By considering the ratio of two similar cross sections and studying $\frac{\sigma_{10}(\mu^+\mu^-\gamma)}{\sigma(\mu^+\mu^-(\gamma))}$, systematic errors arising from the measurement of luminosity and acceptance cancel. This is illustrated by the definition of relative cross section given in equation 5.6 in which the only measured quantities are numbers of events. The only remaining errors are therefore statistical errors from the number of recorded events, assuming that any difference in the acceptances for the two cross sections is negligible. The numerical values of $\frac{\sigma_{10}(\mu^+\mu^-\gamma)}{\sigma(\mu^+\mu^-(\gamma))}$, shown in figure 5.22, are included in table 5.9. Also in the figure is a prediction for the relative cross section from a Monte Carlo at 4-vector level. None of the 4-vector predicted points plotted was used in the evaluation of the correction factor, C_{Rel}.

There is a good agreement between the measured data and the Monte Carlo prediction: the χ^2 per degree of freedom of the measured data compared to the prediction is 9.3/7. The non-resonant behaviour in this distribution indicates that the colinear photons are not strongly dependent upon $\sqrt{s} - M_Z$. As discussed above, the values used for α and $x_\alpha^{\min}$ eliminate most initial state radiation from these measurements. The actual contribution from final state radiation has been estimated by studying 4-vectors events simulated without final state radiation; it is found to be less than 0.01%. The measurements are therefore taken to be a measurement of the colinear final state radiative cross section.

Chapter 6

Measurement of electroweak parameters

The calculated muon pair cross sections and asymmetries described above may be used to measure the electroweak parameters $M_{\rm Z}$, $\Gamma_{\rm Z}$, $\sigma_{\mu\mu}^{\rm pole}$, $\hat{a}_l{}^2$ and $\hat{a}_l{}^2\hat{v}_l{}^2$. In the minimal standard model, the latter four of these may be expressed in terms of $M_{\rm Z}$. Comparing the experimentally determined values of these four parameters with theoretical predictions for the measured $M_{\rm Z}$ constitutes a test of the standard model. This chapter describes a measurement of the five electroweak parameters above and the results of a such a test of the standard model.

The measurements are performed by fitting theoretical expressions for either the lineshape alone, or both the lineshape and integrated asymmetry simultaneously, to the corresponding observed quantities corrected to the full solid angle at each energy point in the scan. The fits are divided into two categories, *viz.* standard model and model independent. In this context, a 'standard model' fit is used to mean that the only parameter fitted is $M_{\rm Z}$ and all couplings and widths (and hence the overall normalisation) depend upon $M_{\rm Z}$. Conversely, a 'model independent' fit is one in which the couplings and widths are fitted as free parameters in addition to $M_{\rm Z}$, although the functional form of the standard model is used throughout for the cross section and asymmetry. Both standard model and model independent fits are presented below.

6.1 Standard model fits

In order to fully describe the lineshape and asymmetry, it is necessary to include various higher order corrections to the tree level cross section as discussed in chapter 4. In a pure standard model fit, the electroweak corrections to the partial widths from self energies and vertex corrections must be evaluated, whereas in the model independent case the partial widths are made free parameters of the fit and so automatically include all such corrections. To avoid making unnecessary approximations, the standard model fits are based upon two semi-analytic programs which incorporate a full one-loop calculation of weak corrections; the contribution from box diagrams, which is negligible at the current level of precision, is not included in the fits.

Both programs also include initial and final state photonic corrections of at least $O(\alpha)$ with exponentiation and interference between initial and final states of $O(\alpha)$. The total cross section calculated by the two programs agree to better than 0.2%, as shown in section 4.5.3. On a technical note, as the evaluation of self energies to determine Γ_Z, M_W and $\sin^2\theta_W$ is very slow, this calculation is only performed once for a given value of M_Z during the fitting process. The lower limit on the invariant mass of the final state muon pair, which is needed in order to evaluate the effect of photonic corrections, is taken to be 12 GeV in all fits as muon candidates are required to have a momentum greater than 6 GeV.

6.1.1 Cross section fit

The cross section is described by the lineshape programs ZSHAPE and ZFITTER. The former program contains a full $O(\alpha^2)$ treatment of initial state photonic corrections, whereas the latter calculation is complete to $O(\alpha)$ with leading terms from $O(\alpha^2)$. Fits are performed by minimising a χ^2 function given by

$$\chi^2 = \sum_{j=1}^{7} \frac{\left(\sigma_{\mu\mu}(s_j) - \sigma^{\text{fit}}(s_j)\right)^2}{\sigma^2_{\sigma_{\mu\mu}(s_j)}}, \tag{6.1}$$

where $\sigma_{\mu\mu}(s_j)$ is the measured cross section, $\sigma^{\text{fit}}(s_j)$ is the fitted value of the cross section and $\sigma^2_{\sigma_{\mu\mu}(s_j)}$ is the variance on the measured cross section. The summa-

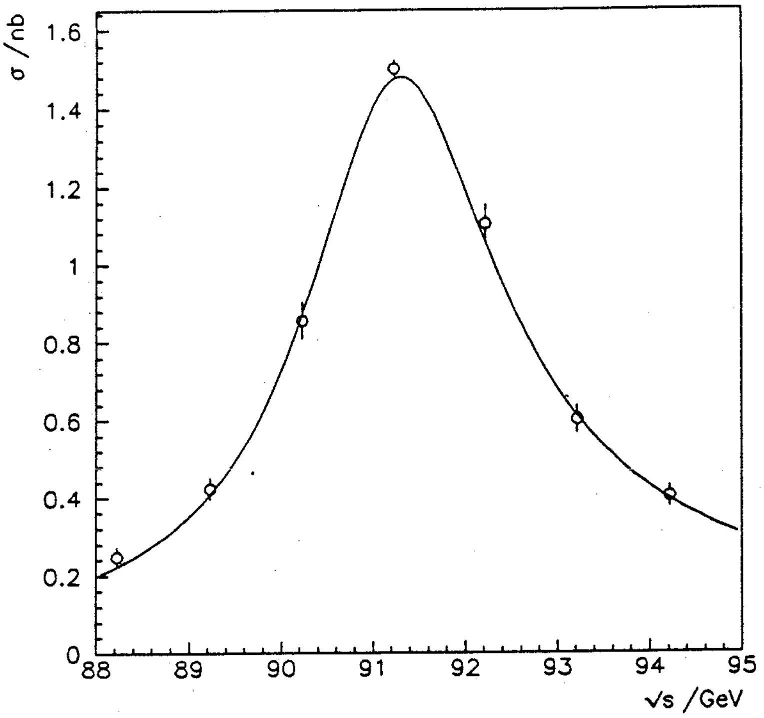

Figure 6.1: Cross section for muon pair production, with standard model fit.

tion extends over the seven centre of mass energies at which cross sections were evaluated. The same fitting package was used as in previous fits of section 5.5.

There is a correlated systematic error on each measured cross section arising from the 1.0% uncertainty in the luminosity measurement. This overall normalisation should strictly be taken into consideration by defining the χ^2 function in terms of a covariance matrix, as described in [65]. However, as the most precise cross section measured has a statistical error of 1.4%, and all other cross sections have statistical uncertainties $\gtrsim$ 5%, this more refined treatment is not necessary with the muon pair data so far accumulated.

Fits based upon both ZFITTER and ZSHAPE were performed and the results were indistinguishable to four significant figures. The fitted lineshape is presented with the measured cross sections in figure 6.1. The fitted value for the mass of the Z^0 obtained is given,

$$M_Z = 91.20 \pm 0.04 \text{ GeV, with } \chi^2/DF = 3.2/6.$$

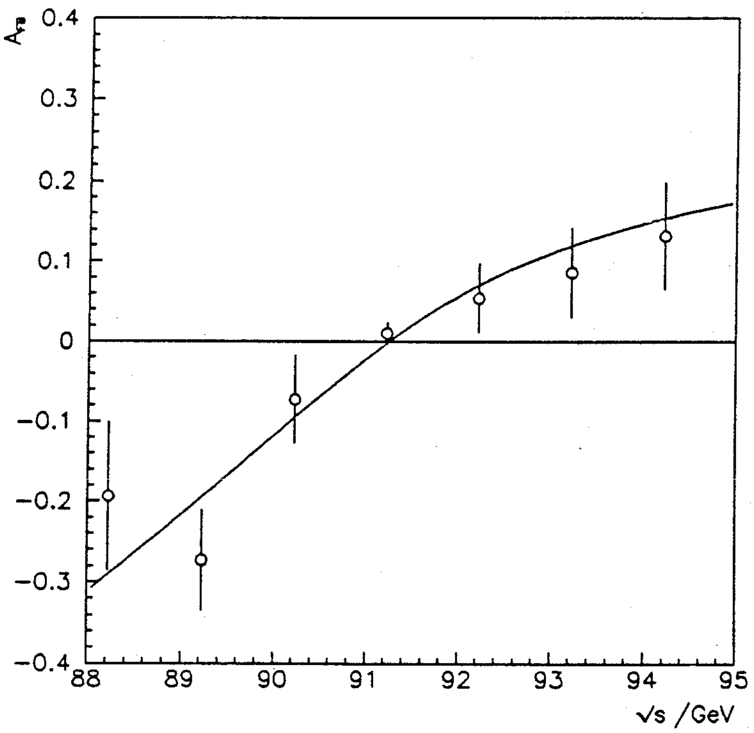

Figure 6.2: Forward-backward asymmetries for muon pairs, with standard model fit.

6.1.2 Cross section and asymmetry fit

The forward-backward asymmetry may also be reduced to a function in which the only significant free parameter is M_Z and therefore may be fitted together with the measured cross section data. A fit is carried out based upon the program `ZFITTER`, in which the cross section and the integrated asymmetry are calculated and compared with the measured data. It is necessary to modify the definition of the function to be minimised for this fit such that,

$$\chi^2 = \sum_{j=1}^{7} \left\{ \frac{\left(\sigma_{\mu\mu}(s_j) - \sigma^{\rm fit}(s_j)\right)^2}{\sigma^2_{\sigma_{\mu\mu}(s_j)}} + \frac{\left(A^{\rm obs}_{\rm FB}(s_j) - A^{\rm fit}_{\rm FB}(s_j)\right)^2}{\sigma^2_{A^{\rm obs}_{\rm FB}(s_j)}} \right\}, \tag{6.2}$$

where $A^{\rm obs}_{\rm FB}(s_j)$ is the measured asymmetry, $A^{\rm fit}_{\rm FB}(s_j)$ is the fitted value of the asymmetry and $\sigma^2_{A^{\rm obs}_{\rm FB}(s_j)}$ is the variance on the measured asymmetry. The result of this fit, which is dominated by the relatively precise cross section data, is

$$M_Z = 91.20 \pm 0.04 \text{ GeV, with } \chi^2/DF = 6.9/13.$$

The fitted and measured asymmetries are illustrated in figure 6.2, showing that the fit to the data is very good as indicated by the χ^2/DF. The conclusion is that at the current precision, the minimal standard model provides an adequate description of the measured muon pair data.

6.2 Model independent fits

Model independent fits are made to the data in an analogous manner to the standard model fits, *i.e.* first the lineshape is fitted and then the lineshape and integrated asymmetry are fitted simultaneously. The fitted results are discussed and compared with the standard model after all fits have been described. In the three model independent fits described below, the cross section is characterised by three parameters, *q.v.* M_Z, Γ_Z and $\sigma_{\mu\mu}^{\mathrm{pole}}$. The reason for introducing $\sigma_{\mu\mu}^{\mathrm{pole}}$, the weakly corrected, resonant component of the cross section at $s = M_Z^2$ without photonic corrections, is to reduce correlations between the parameters in the fit. By definition, it can be seen from equation 4.14 that the pole cross section is given by,

$$\sigma_{\mu\mu}^{\mathrm{pole}} \equiv \frac{12\pi\Gamma_e\Gamma_\mu}{M_Z^2{\Gamma_Z}^2}, \qquad (6.3)$$

where all widths are weakly corrected quantities.

This particular combination of parameters represents an overall normalisation of the cross section on resonance where the γ-Z^0 interference and pure QED terms are relatively small. If universality is assumed between initial and final state charged leptons ($\Gamma_l = \Gamma_e = \Gamma_\mu$), it is possible to fit ${\Gamma_l}^2$ in place of $\sigma_{\mu\mu}^{\mathrm{pole}}$. However, doing so makes the overall normalisation near to resonance a function of three free parameters which introduces large correlations between them. By fitting the pole cross section these strong correlations are circumvented and the results of the fit may be used to determine Γ_l.

6.2.1 Cross section fits

Two fits are made to the cross section data. These are based upon the program `ZFITTER` and an analytic approximation to muon pair cross section. Both fits were carried out by minimising a χ^2 function, as defined in equation 6.1, and have M_Z, Γ_Z and $\sigma_{\mu\mu}^{\mathrm{pole}}$ as parameters to be determined by the fit.

Analytic calculation

The analytic expression for the cross section is based upon the weakly corrected cross section for massless fermions given in equation 4.14. In order to account for the effect of initial state radiation on the lineshape, this cross section has been convoluted with a first order (exponentiated) photon distribution function [16, p 114]. The final form of the cross section, in which interference effects have been neglected, is given in Appendix C.

The fit carried out using this expression describes the data well, with a χ^2/DF value of 2.4/4. The parameter values derived from the fit are presented in table 6.1.

Semi-analytic calculation

The second model independent fit to the cross section is based upon ZFITTER and includes the same photonic corrections as in the standard model fit based upon this program. The cross section to which these photonic corrections are applied includes γ-Z^0 interference and is based upon the improved Born approximation. By inspection of the lowest order form for the total cross section given in equation 4.13, and the resonating function ($\chi_0(s)$) of equation 4.7, it can be seen that the interference term ($C^{(1)}_{\gamma Z}$) makes no contribution to the total cross section at $s = M_Z^2$ in the absence of photonic corrections.

Furthermore, this term is numerically small, contributing less than 0.2% to the cross section at all centre of mass energies considered. In the fit, $C^{(1)}_{\gamma Z}$ is taken from the standard model prediction for $M_H = M_t = 100$ GeV to avoid the introduction of an additional free parameter. Similarly the pure QED term ($C_{\gamma\gamma}$), which is both small and accurately known, is taken from the standard model prediction. These approximations do not significantly influence or bias the measurements made.

In contrast, the term in $C^{(1)}_{ZZ}$ is large on resonance and may be written as

$$C^{(1)}_{ZZ} = \left(\frac{6\sqrt{2}\pi}{G_F {M_Z}^3}\Gamma_l\right)^2 ,$$

which in turn may be rewritten in terms of the pole cross section. As muon pair data alone is analysed, the only partial width that may be extracted from the data is one for which universality between electrons and muons is assumed, *i.e.*

Parameter	$\sigma_{\mu\mu}(s)$ fit		$\sigma_{\mu\mu}(s)$ and $A_{\rm FB}(s)$ fit
	Analytic	ZFITTER	ZFITTER
$M_{\rm Z}$ (GeV)	91.21 ± 0.04	91.21 ± 0.04	91.21 ± 0.04
$\Gamma_{\rm Z}$ (GeV)	2.52 ± 0.07	2.46 ± 0.07	2.46 ± 0.07
$\sigma_{\mu\mu}^{\rm pole}$ (nb)	2.03 ± 0.03	2.03 ± 0.03	2.03 ± 0.03
$\hat{a}_l{}^2\hat{v}_l{}^2(\times 10^{-5})$			73 ± 54
$\hat{a}_l{}^2$			0.23 ± 0.04
χ^2/DF	2.5/4	1.9/4	5.7/9

Table 6.1: Parameters measured by model independent fits.

Γ_l above. Using the above procedure to formulate a cross section in terms of the model independent parameters $M_{\rm Z}$, $\Gamma_{\rm Z}$ and $\sigma_{\mu\mu}^{\rm pole}$, a good fit is made to the data. The χ^2/DF value for the fit, which is 1.9/4, indicates that this formulation of the cross section accommodates the data well. The parameter values derived from the fit are summarised in table 6.1.

6.2.2 Cross section and asymmetry fit

This is the most refined fit of this analysis and is performed by minimising a χ^2 function, as defined in equation 6.2. By fitting the asymmetry as well as the cross section it is possible to measure the effective vector and axial vector couplings (defined by equation 4.9) in the combinations $\hat{a}_l{}^2\hat{v}_l{}^2$ and $\hat{a}_l{}^2$. The improved Born approximation of the differential cross section is used as the basis for the cross section and asymmetry calculations. The same cross section calculation is used as in the previous fit. Implicit in this form for the differential cross section is that only axial vector and vector couplings exist between the Z^0 and charged leptons. The form of the integrated asymmetry that is fitted to the data (before photonic corrections have been applied) is given in equation 4.8. This expression simplifies at $s = M_{\rm Z}^2$ as the resonating function has no real component and the resonant asymmetry is determined by the value of $\frac{C^{(2)}_{\rm ZZ}}{C^{(1)}_{\rm ZZ}}$. Off resonance, the energy dependence of the asymmetry is governed by the ratio $\frac{\Re\{\chi_0(s)\}C^{(2)}_{\gamma{\rm Z}}}{C^{(1)}_{\rm ZZ}|\chi_0(s)|^2}$. Thus the parameters $C^{(2)}_{\rm ZZ}$ and $C^{(2)}_{\gamma{\rm Z}}$ directly influence the asymmetry, as intuitively expected of terms in the differential cross section that are linear in $\cos\theta$.

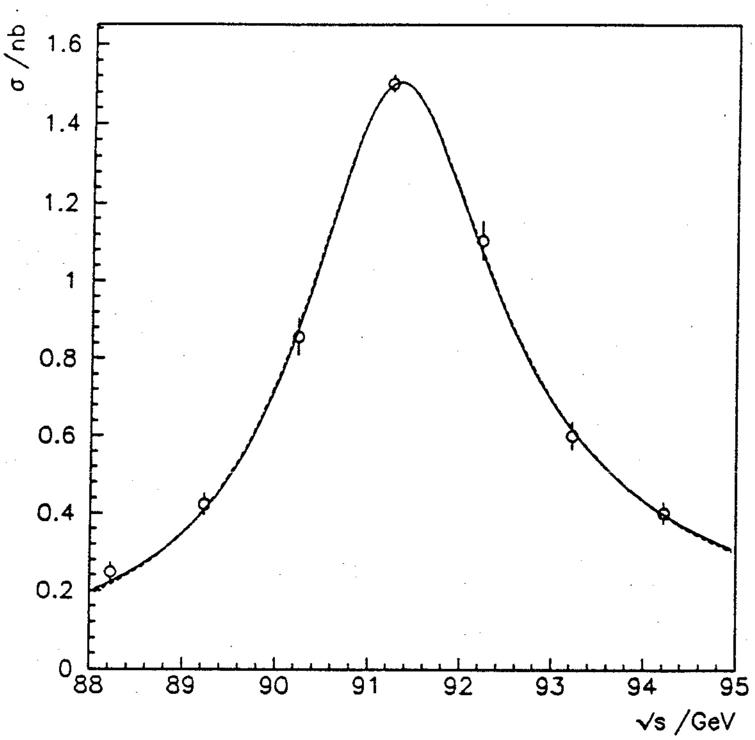

Key
Solid curve: Semi-analytic fit Dotted curve: Analytic fit

Figure 6.3: Cross section for muon pair production, with model independent fits.

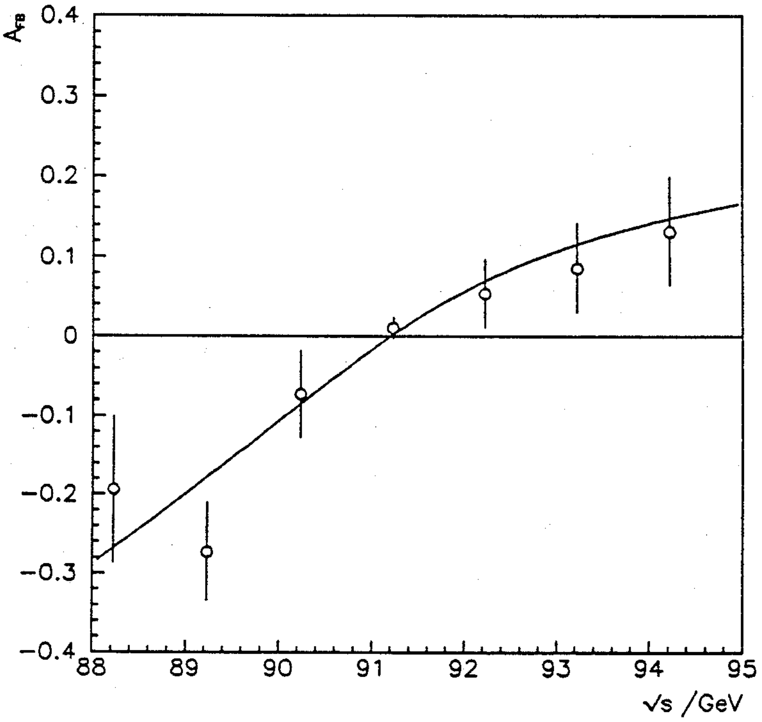

Figure 6.4: Forward-backward asymmetries for muon pairs, with model independent fit.

In the improved Born approximation, these two parameters are assigned the values,

$$C_{ZZ}^{(2)} \equiv 8\hat{a}_l{}^2\hat{v}_l{}^2, \quad C_{\gamma Z}^{(2)} \equiv \frac{4Q_e Q_l \hat{a}_l{}^2}{1-\Delta\alpha},$$

where the couplings are effective leptonic couplings as universality has been invoked between the initial and final state fermions. The denominator in $C_{\gamma Z}^{(2)}$ differs from unity as a consequence of the interference terms in the differential cross section being linear in the effective electromagnetic coupling constant, $\alpha(M_Z^2)$. The value of the QED vacuum polarisation itself, $\Delta\alpha$, depends upon M_Z and M_t as shown in equations 4.10–4.12. As the variation with M_t is weak, a single value of $M_t =$ 100 GeV is used in evaluating $\Delta\alpha$.

This combined fit is carried out and the five parameters so measured are summarised in table 6.1. The χ^2/DF for this fit is 5.7/9. The lineshape resulting from this and the analytic fit are compared with the observed data in figure 6.3. Both fits to the measured cross sections are excellent. A good agreement is also found between the fitted and measured asymmetries, as shown in figure 6.4.

6.3 Comparison of results with standard model

The experimental observables to be compared with the standard model predictions have been determined by three slightly different fits. The results of the various fits are discussed briefly in the next section in order to obtain the 'best' measurement of each parameter before the comparisons are performed.

6.3.1 Summary of experimental results

The electroweak parameters extracted from the model independent fits are summarised in table 6.1. The measured cross section and asymmetry data are accurately described by each of the fits detailed above. A consistent value of the mass of the Z^0 is found among the different fits. All model independent fits yield the same M_Z, which is within one quarter of a standard deviation of that resulting from the from the standard model fits. This implies that the standard model is not likely to be excluded on the basis of this analysis. The value of M_Z to be used as input for subsequent standard model calculations is that from the model independent fits. In addition to the 40 MeV uncertainty on M_Z arising from the fitting procedure, there is a systematic error of approximately 21 MeV on M_Z due to the uncertainty in the absolute beam energy of LEP. (The absolute LEP energy scale was determined by injecting protons into the LEP ring at 20 GeV as originally proposed in [66].)

In the measurement of the total width Γ_Z, the central value of Γ_Z determined by the analytic fit is within one standard deviation of that obtained in the other model independent fits. The value of Γ_Z from the semi-analytic based fit is used in comparisons with the standard model as is derived from a more complete calculation. Although the fit based upon the analytic expression for the cross section contains a greater number of approximations than the corresponding semi-analytic based fits, it is invaluable as a cross check of the more complicated fits. It also illustrates that at the current level of precision in the data, the sensitivity to purely photonic effects beyond $O(\alpha)$ is limited. There is a systematic error on Γ_Z arisising from the point-to-point uncertainty in the LEP machine energy and radiative corrections; it has been estimated to be approximately 10 MeV [2].

The value of the pole cross section is indistinguishable to four significant figures between the various model independent fits. As with all cross sections calculated in this analysis, this is qualified by a systematic error due to the uncertainties in the overall correction factor, F_{corr} (0.8%) and the luminosity measurement (1.0%). These dominant contributions to the systematic error on the pole cross section are added in quadrature and included as a second error term in the table. A measurement of Γ_l, derived from the fitted values of $\sigma_{\mu\mu}^{\mathrm{pole}}$, Γ_Z and M_Z by using the definition of $\sigma_{\mu\mu}^{\mathrm{pole}}$ from equation 6.3, is also included in the table. The systematic error on $\sigma_{\mu\mu}^{\mathrm{pole}}$ is propagated through to Γ_l and quoted for completeness.

The effective couplings, measured as $\hat{a}_l{}^2\hat{v}_l{}^2$ and $\hat{a}_l{}^2$, are only determined by the combined cross section and asymmetry fit. As the values of $\sigma_{\mu\mu}^{\mathrm{pole}}$ and Γ_Z found by this fit are in good agreement with those from the other model independent fits, all parameter values are taken from the combined asymmetry and cross section fit. Doing so allows the correlation of the different parameters to be studied. The

Parameter	Experiment	Standard model
M_Z (GeV)	$91.21 \pm 0.04 \pm 0.02$	input parameter
Γ_Z (GeV)	$2.46 \pm 0.07 \pm 0.01$	$2.489^{+0.037}_{-0.014}$
$\sigma^{\mathrm{pole}}_{\mu\mu}$ (nb)	$2.03 \pm 0.03 \pm 0.03$	$1.988^{+0.006}_{-0.009}$
Γ_l (GeV)	$0.0834 \pm 0.0025 \pm 0.0005$	$0.0836^{+0.0010}_{-0.0006}$
${\hat{a}_l}^2{\hat{v}_l}^2(\times 10^{-5})$	73 ± 54	28^{+25}_{-7}
${\hat{a}_l}^2$	0.23 ± 0.04	$0.2508^{+0.0031}_{-0.0004}$
χ^2/DF	5.7/9	

Table 6.2: Comparison of measured values with standard model predictions.

'best' set of parameters is therefore deemed to be that shown in the rightmost column of table 6.1.

6.3.2 Standard model tests

The standard model predictions for $\sigma^{\mathrm{pole}}_{\mu\mu}$, Γ_Z, ${\hat{a}_l}^2{\hat{v}_l}^2$ and ${\hat{a}_l}^2$, which are functions of M_Z, depend upon the values chosen for the mass of the Higgs boson M_H and the top quark mass M_t. The M_Z dependence of the observables measured herein is far stronger than that predicted for even relatively large changes in either M_t or M_H. The standard model expectation for a given parameter is determined by setting $M_t = M_H = 100$ GeV and using the value,

$$M_Z = 91.21 \pm 0.04\ (\mathrm{exp}) \pm 0.02\ (\mathrm{LEP})\ \mathrm{GeV}$$

obtained in the model independent fits as input to the calculation. An estimate of the error is derived by allowing M_H to vary from 44 to 1000 GeV and M_t from 70 to 230 GeV. The lower limits on these masses are based on [10] and [67] respectively.

The measured parameters and the corresponding theoretical predictions are presented in table 6.2.

There is a good agreement between all measured parameters and the standard model expectation. The prediction for the pole cross section is found to be approximately 1.5 standard deviations away from the observed quantity on the basis of the fitted error alone and less than one standard deviation away from the measurement when the systematic error is added in quadrature with the fitted error. The measurement is entirely consistent with the standard model. It is important

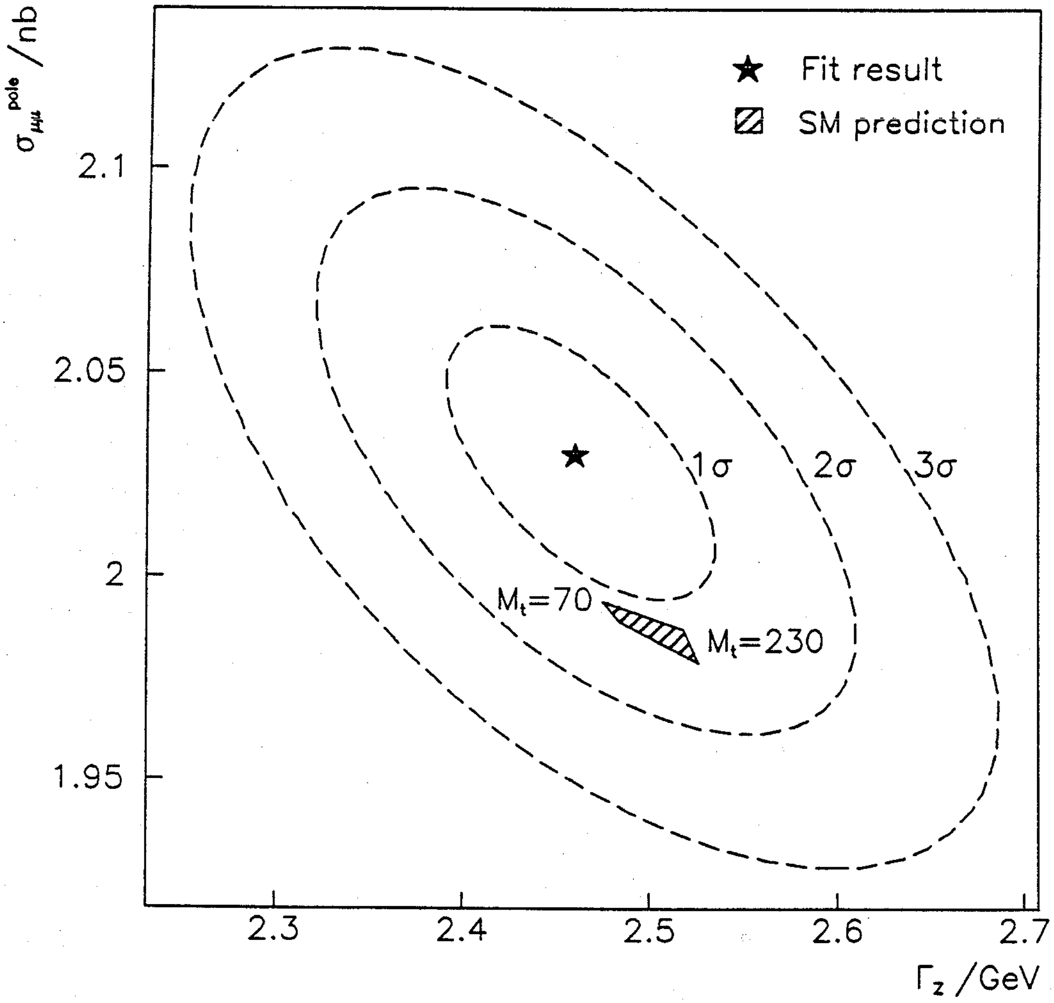

Figure 6.5: Confidence level contours for the measurement of $\sigma_{\mu\mu}^{\text{pole}}$ and Γ_Z.

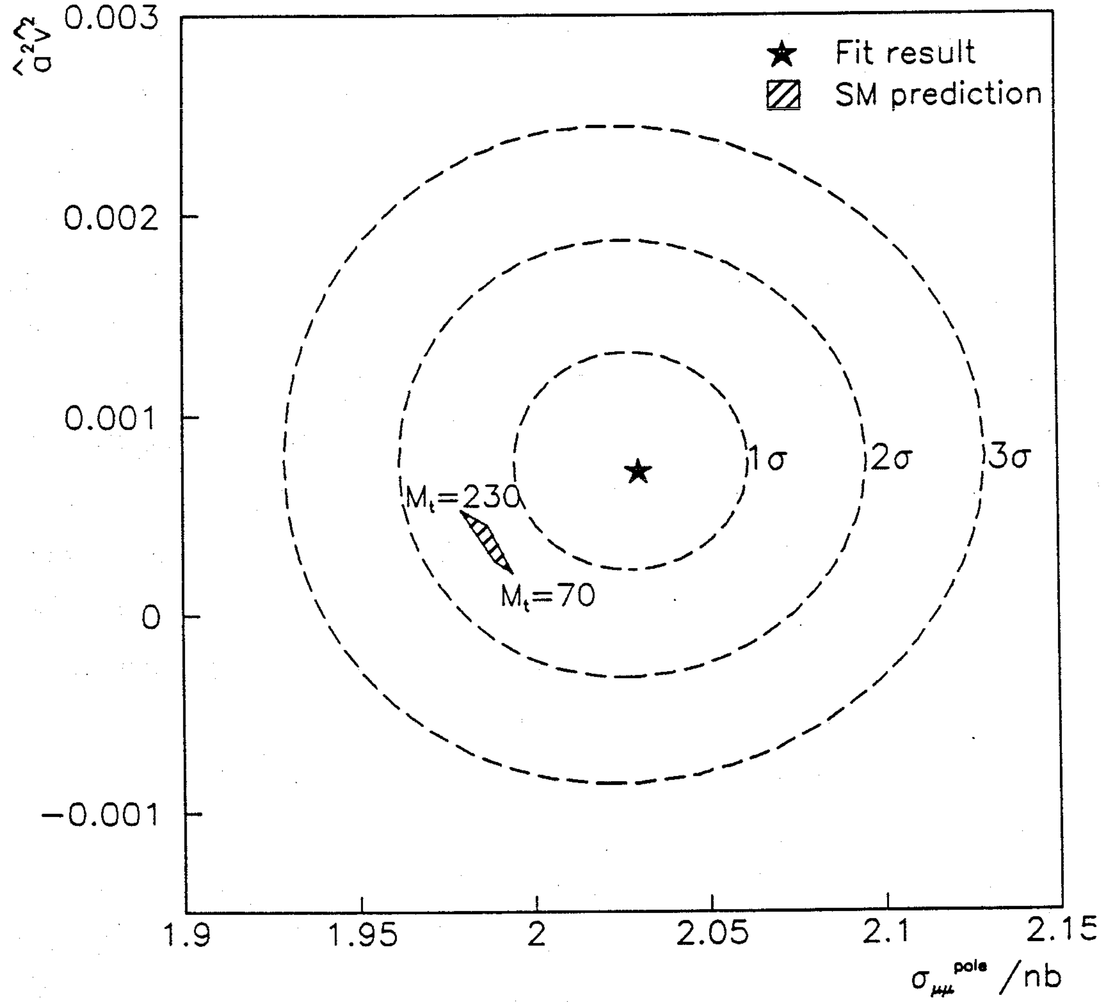

Figure 6.6: Confidence level contours for the measurement of $\hat{a}_l{}^2\hat{v}_l{}^2$ and $\sigma_{\mu\mu}^{\text{pole}}$.

to be aware of the particular convention that is used to define the lowest order couplings from which these effective quantities are derived in order to compare these measurements with other measurements.

A different convention that is commonly encountered is one in which $a_l = 2I_3$ rather than $a_l = I_3$, and similarly for v_l; quantities subsequently derived from these couplings must be rescaled by the appropriate power of 2 before a comparison may be made. For example, the quantities $\hat{a}_l{}^2\hat{v}_l{}^2$ and $\hat{a}_l{}^2$ in the above table must be multiplied by the factors 16 and 4 respectively. Expressed in this convention, the effective couplings measured are $\hat{a}_l{}^2\hat{v}_l{}^2$=0.0117 ± 0.0086 and $\hat{a}_l{}^2$=0.92 ± 0.16, which are consistent with the measurements $\hat{a}_l{}^2\hat{v}_l{}^2$=0.0036 ± 0.0034 and $\hat{a}_l{}^2$=0.99 ± 0.13 of [20] in which a similar analysis was performed using data from three species of leptons and multihadrons.

In order to illustrate the correlation between the measured parameters, the confidence level contours in the $\sigma_{\mu\mu}^{\text{pole}}$-$\Gamma_Z$ plane from the fit are plotted in figure 6.5. The values assumed by the parameters not appearing in the figure are allowed to vary such that the contour may represent a locus of constant χ^2. In this plot, the star indicates the central value of the fit and the shaded area represents the theoretically preferred region of this plane for the allowed variation of M_t and M_H described above. The data is seen to agree with the standard model prediction. The two parameters in the plot are clearly correlated. However, the correlation between $\sigma_{\mu\mu}^{\text{pole}}$ and Γ_Z is far less than that existing between all parameters in a fit which used Γ_l rather than $\sigma_{\mu\mu}^{\text{pole}}$ as a free parameter.

A similar plot of the confidence level contours in the $\hat{a}_l{}^2\hat{v}_l{}^2$-$\sigma_{\mu\mu}^{\text{pole}}$ plane is shown in figure 6.6. The absence of strong correlation between these parameters is expected as the former governs the asymmetry on resonance, which is independent of the absolute normalisation, whilst the latter is proportional to the absolute normalisation on resonance. The region of this plane preferred by the standard model is consistent with the measurements made. The validity of definition of the theoretically preferred region has been verified by mapping the region in question from the $\hat{a}_l{}^2\hat{v}_l{}^2$-$\sigma_{\mu\mu}^{\text{pole}}$ plane to the $\hat{a}_l{}^2\hat{v}_l{}^2$-$\Gamma_l$ plane and comparing with a previous prediction given in [20].

6.4 Conclusions

Using the entire data set recorded by the OPAL detector in 1990 the electroweak parameters of the Z^0 vector boson have been measured to a high precision by studying the process $e^+e^- \rightarrow \mu^+\mu^-(\gamma)$. The $\mu^+\mu^-\gamma$ final state has been studied and the colinear hard photon cross section and differential (energy) cross section have been measured. The photons measured in this process are attributed to final state radiation. The cross sections measured are consistent with the predictions of the standard model. The $\mu^+\mu^-(\gamma)$ final state has been studied and forward-backward asymmetries and cross sections have been measured at seven centre of mass energies in the vicinity of the Z^0 resonance.

The asymmetries have been determined by three different methods which give consistent results that are in agreement with previous measurements [20]. The cross section data has been used to measure the mass and width of the Z^0 and the muon pair pole cross section in a model independent way. The results are,

$$\begin{aligned} M_Z &= 91.21 \pm 0.04 \pm 0.02 \text{ (LEP) GeV}, \\ \Gamma_Z &= 2.46 \pm 0.07 \pm 0.01 \text{ (LEP) GeV}, \\ \sigma_{\mu\mu}^{\text{pole}} &= 2.03 \pm 0.03 \pm 0.03 \text{ nb}, \end{aligned}$$

These results are used to deduce a value for the partial decay width of the Z^0 to charged leptons,

$$\Gamma_l = 0.0834 \pm 0.0025 \pm 0.0005 \text{ GeV}.$$

The cross section and asymmetry data have been used to obtain a measurement of the leptonic couplings to the Z^0. These couplings are measured in the combinations,

$$\begin{aligned} \hat{a}_l{}^2 \hat{v}_l{}^2 &= (73 \pm 54) \times 10^{-5}, \\ \hat{a}_l{}^2 &= 0.23 \pm 0.04, \end{aligned}$$

adopting the convention that $a_l = I_3$. For a given value of the mass of the Z^0 and an allowed range of masses for the Higgs scalar and top quark, the standard model makes unambiguous predictions for each of the parameters which has been measured. The predicted values are shown in table 6.2. The predictions are in good agreement with the measured values for these parameters, which at the present are limited by statistics of the muon pair event sample. On the basis of the studies performed herein, the standard model provides a good description of the process $e^+e^- \rightarrow \mu^+\mu^-(\gamma)$.

Appendix A

OPAL co-ordinate system and track parameters

The OPAL co-ordinate system is a right-handed Cartesian system. The origin of this system is defined by the centre of the jet chamber. The beam axis and the axis of the OPAL solenoid are inclined at an angle of 13.9 mrad to the horizontal plane. The z axis is defined by the e^- direction, the x axis points approximately towards the centre of the LEP ring and the y axis is approximately vertical. Two angles are defined in the OPAL co-ordinate system. These are the azimuthal angle, ϕ, which is measured about the z axis with $\phi = 0$ defined along the $+x$ axis and the polar angle, θ, which is measured from the $+z$ axis. This is best illustrated in figure 2.2 which also shows a perspective view of the OPAL detector.

The vertex quality parameters, d_0 and z_0 are defined in various ways by different experiments. Here, d_0 is defined to be the distance of closest approach of the track to the origin in the r-ϕ plane. It is a signed parameter with $d_0 \geq 0$ for tracks that enclose the origin and $d_0 < 0$ for all other tracks. The parameter z_0 is defined to be the z coordinate of the track at the point of closest approach in the r-ϕ plane, *i.e.* where d_0 is defined.

Other quantities which are required are the physics variables, p_{T}, E_{T}, ζ and ξ. The transverse momentum, p_{T}, is defined as the momentum transverse to the beam direction, *i.e.* in the r-ϕ. The transverse energy, E_{T}, is defined as the electromagnetic energy at a given (θ, ϕ) that has been corrected for the amount of material through which the particle has passed (the 'corrected' as opposed to 'raw' ECAL energy) multiplied by $\sin\theta$.

Two important angles may be formed between any two tracks with momentum vectors $\vec{p}_1$ and $\vec{p}_2$. These are the acolinearity, ζ, and the acoplanarity, ξ. It is important to note that the acolinearity is a three-dimensional quantity, whereas the acoplanarity is only a two-dimensional one. The acolinearity is defined by,

$$\cos\zeta \equiv \frac{\vec{p}_1 \cdot \vec{p}_1}{|\vec{p}_1||\vec{p}_1|},$$

and the acoplanarity by,

$$\xi \equiv ||\phi_1 - \phi_2| - \pi|,$$

where ϕ_1 and ϕ_2 are the azimuthal angles of the two tracks.

From these definitions, it can be seen that two tracks that have an acolinearity of zero are back-to-back in three dimensions, and similarly tracks having a zero acoplanarity are back-to-back in the r-ϕ plane.

Appendix B

PASS 2 processing in the ME processor

The ME processor is capable of recognising certain conditions in which it cannot reconstruct an event. On detecting such a circumstance, an attempt is made to recover the event by restarting the processing using a modified set of segment finding rules. The conditions under which this second pass takes place, the modifications to the segment finding and the changes to the program control within the processor are described below.

Second pass processing is normally associated with localised areas of high activity in the chambers caused by showers of low energy particles emerging from the outer surface of the HCAL or iron absorber. As the muon endcap readout is projective and small correlations that exist in pulse heights between the signals recorded in either projection are not used, the number of possible three-dimensional track segments tends to increase as the square of the number of 2d-segments in either projection. It is clear that in events with an exceptionally high number of hits in a small area, the number of possible combinations of track segments will become unphysically large.

A series of checks are made before loop variables or certain array indices are incremented in order to trap possible 'overflow' events. The internal checks made correspond to readily identified objects in the detector. Details are given by the processor of the particular point in the code for which PASS 2 processing was necessary. The ME processor invokes second pass processing if any of the following conditions are satisfied during the initial processing of the event with default processing parameters:

```
|
|---MEBAT           Convert raw data to track segments.
|       |---MEDICN  Find hits present in (packed) raw data.
|       |       |---MESTCO  Convert strip number to OPAL system.
|       |---MEPATR  Find and fit track segments.
|       |---MEUPCO  Save normal parameters if processing incomplete.
|       |---MEWIPE  Clear debris if event processing incomplete.
|       |---MEUPCO  Use "PASS 2" parameters if appropriate.
|       |---MEPATR  Try to find track segments in "PASS 2"?
|       |---MEUPCO  Restore normal parameters after re-processing?
|       |---MEWIPE  Clear debris if event processing still incomplete.
|---MEDROP          Tidy up intermediate processing results.
```

Figure B.1: Decomposition of the ME PASS 2 processing into subroutines.

1. There are more than 500 clusters in the whole detector.
2. There are more than 1500 2d-segments in any projection at either end.
3. There are more than 200 2d-segments that satisfy CJ pointing and survive ambiguity resolution in any projection at either end.
4. There are more than 150 unused coordinates.
5. There are more than 1500 3d track segments in either endcap.

For second pass processing the segment finding rules are significantly modified from those used in normal processing, which are described in chapter 3. The second pass processing parameters result in the following changes of behaviour of the segment finder:

- The road width is increased from 0.9 cm to 1.0 cm
- Each track segment is required to have minimum of four xz hits matched to four yz hits from the same streamer tube planes; thus no 2-hit or 3-hit 2d-segments will be formed during a second pass processing.
- 2d-segments are considered 'identical' if their slope and intercept differ by less than 10 standard deviations. (Normally this comparison is performed at the 3 standard deviation level.)

If any of the original limits that initiate the second pass processing are exceeded during a second pass phase then all segments are cleared and the event is considered lost. This occurs in less than 0.05% of all events with a comparable frequency in both Monte Carlo and real data. The control of the ME processor under these circumstances is illustrated in figure B.1. Failure of the normal processing is indicated by a non-zero return code from the routine MEPATR. This causes the current set of processing parameters, which may have been altered by `FFREAD` data cards from the default values, to be stored temporarily (MEUPCO); the data structure is cleaned up to remove incomplete processing results (MEWIPE); the PASS 2 parameters are loaded from either the main calibration database or from data cards if they are present (MEUPCO) and then the segment finding is restarted (MEPATR).

The initial segment finding parameters are subsequently restored to reinstate normal segment finding rules (MEUPCO). If the event processing is still incomplete, the event data is cleared (MEWIPE) and the event is deemed unusable.

Appendix C

Approximate analytic cross section for $e^+e^- \longrightarrow \mu^+\mu^-$

Any expression for the $e^+e^- \rightarrow \mu^+\mu^-$ cross section that is to be of practical use in the vicinity of the Z^0 must include at least the first order photonic corrections and preferably exponentiation of the soft photon terms as well. Such an expression can be derived, albeit with approximations, following the structure function formalism (outlined in [16, p 104]) in which a cross section without photonic corrections, $\sigma_{\mathrm{no}\gamma}$ is convoluted with a 'radiator' or photon distribution function, $G(y)$, to yield a cross section that includes photonic corrections.

The general form of the cross section in this approach is given by

$$\sigma(s) = \int_{y_0}^{1} dy\, \sigma_{\mathrm{no}\gamma}(sy) G(y), \tag{C.1}$$

in which the function $G(y)$ represents the probability of radiating a fraction $(1-y)$ of the centre of mass energy from the initial state with,

$$y = \frac{s'}{s} \qquad \text{and} \quad 4\frac{M_\mu^2}{s} \le y_0 \le y \le 1.$$

The specific form of $G(y)$ used here includes only first order terms and is given by,

$$G(y) = \beta(1-y)^{\beta-1}(1+\delta_1^{v+s}) + \delta_1^h$$

where,

$$\delta_1^{v+s} = \frac{\alpha}{\pi}\left(\frac{3}{2}L + \frac{\pi^2}{3} - 2\right),$$

$$\delta_1^h = -\frac{\alpha}{\pi}(1+y)(L-1),$$

$$L = \ln\frac{s}{m_e^2}, \qquad \beta = \frac{2\alpha}{\pi}(L-1).$$

A further approximation that simplifies the convolution is the use of the weakly corrected cross section for massless fermions $\sigma_w(s)$, as given in equation 4.14, in the integral above. For the precision required with the current integrated luminosity, the interference term of $\sigma_w(s)$ has been excluded as its retention requires an additional free parameter if this expression is fitted to real data. The integral of equation C.1 has been evaluated ([16, p 114]) and leads to the final approximate expression for the total muon pair cross section given below.

$$\begin{aligned}
\sigma(s) = & \left\{ \frac{C_R}{s}\left(\eta^{\beta-2}\phi(\cos\zeta,\beta)(1+\delta_1^{v+s}) - \frac{\beta}{2}J_1\right)\right. \\
& -\frac{C_R}{s}\left(\frac{\beta}{\beta+1}\eta^{\beta-1}\phi(\cos\zeta,\beta+1)(1+\delta_1^{v+s}) - \frac{\beta}{2}J_2\right) \\
& +\frac{C_Q}{s}\left[1+\frac{\alpha}{\pi}L\left(2\ln(1-\frac{s_0'}{s}) - \ln\frac{s_0'}{s} + \frac{1}{2} + \frac{s_0'}{s}\right)\right. \\
& \left.\left. + \frac{\alpha}{\pi}\left(\frac{\pi^2}{3} - 1 - 2\ln(1-\frac{s_0'}{s}) + \ln\frac{s_0'}{s} - \frac{s_0'}{s}\right)\right]\right\}
\end{aligned}$$

where,

$$\begin{aligned}
C_R &= \frac{12\pi\Gamma_e\Gamma_\mu}{M_Z^2(1+\gamma^2)}, \\
C_Q &= \frac{4\pi}{3}{Q_\mu}^2\alpha^2(M_Z^2), \\
\phi(\cos\zeta,\beta+1) &= \frac{\pi\beta\sin[(1-\beta)\zeta]}{\sin\pi\beta\ \sin\zeta}, \\
J_1 &= \frac{2+a}{b}A - \frac{B}{2}, \\
J_2 &= -\frac{a^2+2a-b^2}{b}A + (a+1)B - 1,
\end{aligned}$$

with the substitutions,

$$\tilde{M}_Z = \frac{M_Z}{\sqrt{1+(\Gamma_Z/M_Z)^2}}, \qquad \tilde{\Gamma}_Z = \frac{\Gamma_Z}{\sqrt{1+(\Gamma_Z/M_Z)^2}},$$

$$a = {\tilde{M}_Z}^2/s - 1, \qquad b = \tilde{M}_Z\tilde{\Gamma}_Z/s,$$

$$\eta = \sqrt{a^2+b^2}, \qquad \cos\zeta = a/\eta,$$

$$A = \arctan\frac{a+1}{b} - \arctan\frac{a}{b}, \qquad B = \ln\frac{a^2+2a+1+b^2}{a^2+b^2}.$$

The parameter s_0' is the minimum invariant mass squared of the final state muon pair, *i.e.* $s_0' \equiv s y_0 \geq 4M_\mu^2$.

References

[1] S.L.Glashow, Nucl. Phys. **22** (1961) 579,
S.Weinberg, Phys. Rev. Lett. **19** (1967) 1264,
A.Salam, 'Elementary Particle Theory', (Ed.) N.Svartholm,
(Almqvist and Wikell, Stockholm, 1968) pg. 367.

[2] F.Dydak, 'Results From LEP and the SLC',
report presented at the 25th International Conference on High Energy Physics, Singapore, August 1990.

[3] T.Cheng and L.Li,
'Gauge Theory of Elementary Particle Physics',
(1984), Oxford University Press.

[4] M.Kobyashi and T.Maskawa, Prog. Theor. Phys. **49** (1973) 652.

[5] T.Kinoshita and J. Sapirstein,
'Atomic Physics Nine'
(Eds.) R.S.Van Dyck Jr. and E.N.Fortson (1984)
(Singapore: World Scientific).

[6] G.'t Hooft,
Nucl. Phys. **B33** (1971) 173,
Nucl. Phys. **B35** (1971) 167.

[7] I.J.R.Aitchison and A.J.G.Hey,
'Gauge theories in particle physics', 2nd edition, (1989),
Adam Hilger.

[8] P.W.Higgs,
Phys. Rev. Lett. **13** (1964) 508
Phys. Rev. **145** (1964) 1156.

[9] S.Weinberg, Phys. Rev. **D13** (1976) 974.

[10] OPAL collaboration, M.Z.Akrawy *et al.*, CERN-PPE/90-150,
October 1990, submitted to Phys. Lett. **B**.

[11] F.J.Hasert *et al.*, Phys. Lett. **B46** (1973) 138.

[12] G.T.J.Arnison *et al.*, Phys. Lett. **B122** (1983) 103.
G.T.J.Arnison *et al.*, Phys. Lett. **B126** (1983) 398.
M.Banner *et al.*, Phys. Lett. **B122** (1983) 322.
P.Bagnaia *et al.*, Phys. Lett. **B129** (1983) 130.

[13] J.Nash, 'First results from MARK II',
CERN-EP seminar. Genève, 15th September, 1989.

[14] (Eds.) J.Ellis and R.Peccei,
'Physics at LEP, Vols. 1 and 2', CERN 86-02.

[15] (Eds.) A.Böhm and W.Hoogland ,
'EFCA Workshop on LEP 200', Vols. 1 and 2,
CERN 87-02, ECFA 87/08.

[16] (Eds.) G.Altarelli, R.Kleiss and C.Verzegnassi,
'Z Physics at LEP 1', Vol. 1, CERN 89-08.

[17] (Eds.) G.Altarelli, R.Kleiss and C.Verzegnassi,
'Z Physics at LEP 1', Vol. 3, CERN 89-08.

[18] J.K.Sedgebeer, 'Z^0 lineshape parameters from e^+e^- colliders', presented at the 10th International Conference on Physics in Collision, Duke University, Durham, North Carolina, USA 1990.

[19] OPAL collaboration, M.Z.Akrawy *et al.*,
CERN-PPE/90-143, October 1990, submitted to Z. Physik. **C**.

[20] OPAL collaboration, M.Z.Akrawy *et al.*,
Phys. Lett. **B247** (1990) 458,
OPAL Physics Note 90-16 (unpublished), presented at 25th International Conference on High Energy Physics, Singapore, August 1990.

[21] 'CERN 1988', Annual Report 1988, Vol. 1, pp 24–31,
CERN (1988).

[22] (Ed.) S. Turner,
'Proceedings of the CERN Accelerator School', CERN 90-03.

[23] K.Ahmet *et al.*,
'The OPAL detector at LEP', CERN-PPE/90-114, August 1990,
to be published in Nucl. Instr. and Meth. (1990).

[24] T.J.Smith, Ph.D. Thesis, University of Birmingham (1990)

[25] H.Drumm *et al.*, Nucl. Instr. and Meth., **176** (1980) 333.

[26] G.Battistoni *et al.*, Nucl. Instr. and Meth. **176** (1980) 297.

[27] M.D.Rosseau *et al.*, IEEE Trans. Nucl. Sci., NS-30, (1983) 479.

[28] J.Allison *et al.*, Nucl. Instr. and Meth. **A238** (1985) 220.

[29] J.Allison *et al.*, Nucl. Instr. and Meth. **A236** (1985) 284.

[30] G.T.J.Arnison *et al.*, Nucl. Instr. and Meth. **A294** (1990) 431.

[31] M.J.Couch, Ph.D. Thesis, University of Birmingham, submitted December 1990.

[32] S.Weisz,
'ROPE Primer. Latest revision for ROPE312/11',
November 1990 (unpublished).

[33] J.Dumont, S.W.O'Neale and D.R.Ward,
'The GOPAL Users' Manual', February 1987 (unpublished),
D.R.Ward, 'A GOPAL Primer. (Latest revisions for GOPAL124)',
October 1990 (unpublished).

[34] R.Brun *et al.*,
GEANT312, Report DD/EE/84-1, CERN (1989).

[35] R.Brun *et al.*,
FFREAD (Free Format Input Processing),
CERN library entry I302, CERN (1987).

[36] R.Brun *et al.*,
ZEBRA, CERN library entry Q100, CERN (1988).

[37] 'Programming Language FORTRAN ANSI X3.9-1978',
ANSI, (1978).

[38] G.N.Patrick and D.R.Ward,
'OPAL Coding and Documentation Conventions',
September 1987, (unpublished).

[39] J.Zoll, PATCHY 4.13, CERN library entry L400 (1988).

[40] N.K.Watson,
'Calibrations and constants in MExxx',
BHAM/OPAL/90/001 (unpublished).

[41] D.L.Rees and P.M.Watkins,
'ME comparison with GOPAL', OPAL Technical Note TN025,
July 1990 (unpublished).

[42] D.A.Ross, J.C.Taylor, Nucl. Phys. **B** 51 (1973) 25,
A. Sirlin, Phys. Rev. **D** 22 (1981) 971.

[43] D.R.Yennie *et al.*, Ann. Phys. **13** 379.

[44] W.J.P. Beenaker, F.A. Berends and S.C. van der Marck
'Line shape program `ZSHAPE`'
(Institut-Lorentz, University of Leiden, POB 9506, 2300 RA Leiden,
The Netherlands).

[45] S.Jadach, B.F.L. Ward, Z.Was, R.G.S. Stuart, and W.Hollik, 'KORALZ the Monte Carlo Program for τ and μ pair Production Processes at LEP/SLC', (1989) (unpublished).

[46] D.Bardin *et al.*, Lineshape program `ZFITTER`, Dubna-Zeuthen radiative correction group (based upon the `ZBIZON` package),
D.Yu.Bardin *et al.*, Berlin-Zeuthen preprint PHE 89-19, (1989).

[47] G.Burgers,
'The shape and size of the Z resonance', Polarisation at LEP, Vol. 1, CERN 88-06 (1988) 121.

[48] S.Jadach and Z.Was,
'Suppression of QED interference contributions to the charge asymmetry at the Z^0 resonance', CERN-TH.5127/88, July 1988.

[49] OPAL collaboration, M.Z.Akrawy *et al.*,
'The OPAL trigger system', to be submitted to Nucl. Instr. and Meth.

[50] S.J.Hillier,
'Initial experience with the readout and trigger of the endcap muon detectors of OPAL', Birmingham University midterm report, January 1990.

[51] OPAL collaboration, M.Z.Akrawy *et al.*,
'The OPAL filter system', to be submitted to Nucl. Instr. and Meth.

[52] MC68020, MC68030 32-bit microprocessors; Motorolla Inc.

[53] C.M.Hawkes,
'Luminosity counting in ROPE', OPAL Technical Note TN003, July, 1990 (unpublished).

[54] A.Buijs,
'The OPAL DST (OD) processor in ROPE',
16/OFFL-0318, April 1990 (unpublished).

[55] G.D.Lafferty and S.W.O'Neale,
'The CE and CA processes in ROPE (version 309)',
ROPE-0121, October 1990 (unpublished).

[56] R.H.P.Kleiss,
'Hard Bremsstrahlung in $e^+e^- \to \mu^+\mu^-$: Matching theory and experiment', Physics at LEP, Vol. 1, CERN 86-02 (1986) 153.

[57] F.Boillet and Z.Was, Z. Physik. **C 43** (1989) 109.

[58] M.Böhm and W.Hollik, Nucl. Phys. **B** 304 (1988) 687,
F.A.Berends, R.Kleiss and W.Hollik, Nucl. Phys. **B** 304 (1988) 712.

[59] W.J.P.Beenaker, F.A.Berends and S.C.van der Marck (Institut-Lorentz, University of Leiden, POB 9506, 2300 RA Leiden, The Netherlands), Bhabha line shape program ALIBABA. A description of the theoretical framework. 'Large angle bhabha scattering at LEP', can be obtained from the authors.

[60] T.Sjöstrand, Comp. Phys. Comm. **39** (1986) 347,
T.Sjöstrand and M.Bengston Comp. Phys. Comm. **39** (1986) 347,
M.Bengston and T.Sjöstrand, Phys. Lett. **B185** (1987) 435,
M.Bengston and T.Sjöstrand, Nucl. Phys. **289** (1987) 810.

[61] R.Battacherya, J.Smith and G.Grammer, Phys. Rev. **D** 15 (1977) 3267,
J.Smith, J.A.M.Vermaseren, G.Grammer Phys. Rev. **D** 15 (1977) 3280.

[62] F.James and M.Roos,
'Function minimisation and error analysis', MINUIT release 89.12, CERN program library entry D506.

[63] J.E.Conboy, G.M.Dallavalle, C.M.Hawkes *et al.*,
'Luminosity calculation technical note',
February 1990 (unpublished).

[64] OPAL collaboration, M. Z. Akrawy *et al.*, Phys. Lett. **B240** (1990) 497.

[65] Wim de Boer, DESY 89-111, September 1989, presented at the Brighton Conference on Electroweak Radiative Corrections,
July 9th–14th, 1989.

[66] A.Hofmann and T.Risselada,
'Injection of protons into LEP for diagnostics experiments and absolute energy calibration', LEP Note 383, June 1982.

[67] Particle Data Group, M.Aguilar-Benitez *et al.*, Phys. Lett. **B239** (1990) 1–516.